

The Beagle 2 X-ray Spectrometer for Mars

Thesis submitted for the degree of
Doctor of Philosophy
at the University of Leicester

By

Dean Lee Talboys
Space Projects and Instrumentation Group
Department of Physics and Astronomy
University of Leicester

28th June 2006

UMI Number: U601137

All rights reserved

INFORMATION TO ALL USERS

The quality of this reproduction is dependent upon the quality of the copy submitted.

In the unlikely event that the author did not send a complete manuscript and there are missing pages, these will be noted. Also, if material had to be removed, a note will indicate the deletion.



UMI U601137

Published by ProQuest LLC 2013. Copyright in the Dissertation held by the Author.
Microform Edition © ProQuest LLC.

All rights reserved. This work is protected against
unauthorized copying under Title 17, United States Code.



ProQuest LLC
789 East Eisenhower Parkway
P.O. Box 1346
Ann Arbor, MI 48106-1346

The Beagle 2 X-ray Spectrometer for Mars

Dean Lee Talboys

Abstract

This thesis is concerned with the Beagle 2 X-ray spectrometer (XRS) for Mars. The scientific goals of the XRS were to perform (i) geochemical analyses of Martian rocks and soils and (ii) *in situ* $^{40}\text{K} \rightarrow ^{40}\text{Ar}$ dating of rocks. The major aims of this study were the development of the XRS to achieve its scientific goals and to inform the design of future versions of the instrument. The XRS is described and compared with the previous X-ray Spectrometers that have been successfully deployed on Mars. A characterisation of the XRS investigated the fundamental behaviour of the instrument in terms of its spectral features (gain, resolution and artefacts), gain variation with temperature of its components, deadtime and quantum efficiency. The XRS was calibrated to convert elemental intensities from its analyses into concentrations. The concentrations of several major and trace elements of interest in reference materials were linearly correlated with the certified concentration. The analytical performance of the XRS was evaluated in comparison with a terrestrial portable X-ray spectrometer (PXRF) and a wavelength dispersive X-ray spectrometer (WD XRF). The performance was characterised in terms of accuracy, detection limit and fitting precision. This study showed the importance of energy resolution to the analytical performance of the XRS. The operational performance of the XRS was evaluated. The geochemical composition of several basalts analysed by the XRS agreed with complementary analyses by the PXRF and WD XRF. The $^{40}\text{K} \rightarrow ^{40}\text{Ar}$ radiometric ages for two basalts were determined using the K content in the basalts in conjunction with their ^{40}Ar isotope content (analysed by a laboratory version of the Beagle 2 Gas Analysis Package). The $^{40}\text{K} \rightarrow ^{40}\text{Ar}$ ages were found to differ to the Ar-Ar ages because of various effects associated with inhomogeneity of the K content in the rock and radiogenic ^{40}Ar loss.

Declaration

I hereby declare that no part of this thesis has been previously submitted to this or any other university as part of the requirement for a higher degree. The work described herein was conducted solely by the undersigned except for those colleagues and other workers acknowledged in the text.

Dean Lee Talboys

28th June 2006

Dedication

For Mum

Acknowledgements

Firstly, I would like to thank all staff and PhD students in the Space Research Centre for making such a great environment in which to work over the course of my PhD. I would also like to thank all the people involved in the Beagle 2 Mars project for a totally unique experience.

Special thanks to my supervisor George Fraser for his guidance during my PhD and with this thesis. I would also like to thank those involved with the Beagle 2 X-ray Spectrometer, most particularly Nick Nelms and Gillian Butcher. I would also like to thank Phil Potts, of the Open University, and Dariuz Wegrzynek, of the International Atomic Energy Authority, for their valuable advice.

And of course, thanks to Sophia for all her support.

Finally, I would like to gratefully acknowledge the financial support received from the Particle Physics and Astronomy Research Council during my research studentship.

Publications

Some of the results presented in this thesis have been incorporated into the following papers:

1. **D. L. Talboys**, N. P. Bannister, G. W. Fraser, R. Ambrosi, M. R. Sims, N. Nelms, D. Pullan, J. Holt,
‘Instrumentation for Geological Field Work on the Moon’,
Earth, Moon and Planets, vol. 94, (2005), pp. 267-277.
2. **D. L. Talboys**, G. W. Fraser, M. R. Sims, D. Pullan, H.-F. Chen, J.-S. Wang, Z.-Y. Pu, W.-X. Jiao,
‘A Sino-European Collaboration to Develop a Potential Payload Element for the Chinese Lunar Exploration Programme’,
Geophysical Research Abstracts, vol. 7, (2005), no. 01158.
3. **D. L. Talboys**, P. J. Potts, G. W. Fraser, G. Butcher,
‘The Comparative Analytical Performance of the Beagle 2 X-ray Spectrometer’,
Analytical Chemistry, in preparation, 2006.
4. **D. L. Talboys**, D. Pullan, A. Verchovsky, I. P. Wright, S. P. Kelley, G. W. Fraser, M. R. Sims, C. T. Pillinger,
“Demonstration of Radiometric Dating of Martian Analogue Rocks using the Beagle 2 X-ray Spectrometer and Gas Analysis Package”,
Planetary and Space Science, in preparation, 2006.

Contents

Abstract	ii
Declaration	iii
Dedication	iv
Acknowledgements	v
Publications	vi
Contents	vii
Chapter 1 Introduction	1
1.1 X-ray Spectrometric Studies of the Geochemistry of Mars	1
1.2 The Beagle 2 X-ray Spectrometer.....	2
1.3 Thesis Organisation.....	2
Chapter 2 <i>In situ</i> X-ray Fluorescence Spectroscopy for Mars	4
2.1 X-ray Fluorescence Spectroscopy for Geochemical Analyses on Planetary Surfaces....	4
2.2 The Viking X-Ray Fluorescence Spectrometer.....	5
2.3 The Mars Pathfinder Alpha Proton X-ray Spectrometer.....	13
2.4 The Mars Exploration Rovers Alpha Particle X-ray Spectrometers	19
2.5 Summary	26
Chapter 3 The X-ray Spectrometer for Beagle 2	27
3.1 Introduction.....	27
3.2 The Beagle 2 Lander for Mars	27
3.3 The Beagle 2 X-ray spectrometer.....	31

3.4 Calibration Facility.....	37
3.5 Summary	40
Chapter 4 Characterisation of the X-ray Spectrometer	41
4.1 Spectrum Gain and Energy Resolution	41
4.2 Spectrum Artefacts and Background.....	47
4.3 Detection Efficiency.....	53
4.4 Dead time	58
4.5 Gain Variation with Temperature	62
4.6 Summary	67
Chapter 5 Calibration of the X-ray Spectrometer	68
5.1 Introduction.....	68
5.2 Analysis of Reference Materials	68
5.3 Qualitative Analysis and Spectral Fitting.....	71
5.4 The Backscatter Fundamental Parameter Method.....	76
5.5 Calculation of the Geometric Constant and Average Incidence and Exit Angles.....	81
5.6 Quantitative Calibration	85
5.7 Discussion	89
5.8 Summary	92
Chapter 6 The Comparative Analytical Performance of the X-ray Spectrometer.....	93
6.1 Introduction.....	93
6.2 Experimental	93

6.3 Results	96
6.3.1 Fitting Precision	96
6.3.2 Accuracy	102
6.3.3 Detection Limit	106
6.4 Conclusion.....	110
6.5 Summary	111
Chapter 7 The Operational Performance of the X-ray Spectrometer.....	112
7.1 Introduction.....	112
7.2 Experimental Arrangement	112
7.3 Geochemical Composition of the Basalts	113
7.3.1 Scientific Contribution of the XRS to Martian Geochemistry	117
7.4 Radiometric ages of the Basalts	119
7.4.1 <i>In situ</i> $^{40}\text{K} \rightarrow ^{40}\text{Ar}$ Radiometric Dating on Mars Using Beagle 2.....	119
7.4.2 Argon isotope content.....	122
7.4.3 Radiometric ages.....	123
7.4.4 Discussion.....	126
7.5 Conclusion.....	128
7.6 Summary	129
Chapter 8 Conclusions	130
Bibliography.....	134

Chapter 1

Introduction

1.1 X-ray Spectrometric Studies of the Geochemistry of Mars

The exploration of Mars has several notable scientific justifications, perhaps most significantly to investigate if life ever arose on the Red Planet (McKay, 1986). The existence of water on Mars is an essential prerequisite for extinct or extant life (Harland, 2005). There is compelling evidence that water played a significant role in shaping the evolution of the planet (Kargel, 2004; Carr, 1995). Mars also has an important place in comparative planetology (Harland, 2001) and is worthy of study to enhance our understanding of other terrestrial planets in the Solar System.

There is a 40 year history of robotic exploration of Mars, with orbiters and landers (Surkov, 1996), beginning with NASA's Mariner 4 orbiter which performed the first successful flyby of Mars in 1965. Several landers have been sent to the Martian surface by the USA and Russia to provide complementary ground investigations to orbital measurements.

An important measurement on the Martian surface is the geochemical composition of rocks and soils. The geochemistry of the Martian regolith has implications for the bulk composition and internal structure of Mars which places constraints on the origin and evolution of the planet (Longhi et al., 1992). X-ray fluorescence is a valuable technique for the geochemical analysis of rocks (Potts, 1987). There is a significant heritage for the deployment of X-ray Spectrometers in the Solar System including Mars, Venus and the Moon (Surkov, 1996). For Mars, the X-ray fluorescence technique has been implemented in instruments on the two Viking landers (landed 1976), Mars Pathfinder's Sojourner Rover (landed 1997) and the two Mars Exploration Rovers (landed 2004). The technique will again be used by an instrument on the Mars Science Laboratory (due to be launched in 2009). For each mission, the geochemical analyses have been crucial for interpreting the nature, origin and evolution of the geological environment. The Viking landers made the first analyses of the Martian regolith (Clark et al., 1982). The Pathfinder Sojourner rover was first to analyse rocks on Mars (Rieder et al., 1997b) while the two Mars Exploration Rovers were the first to detect chemical signatures in rocks that indicate alteration by water (Rieder et al., 2004; Gellert et al., 2004).

1.2 The Beagle 2 X-ray Spectrometer

Beagle 2 was the exobiology lander for ESA's Mars Express orbiter (Schmidt, 2003). The primary objective of Beagle 2 was to establish whether life is present or ever had existed on Mars. The X-ray Spectrometer, designed and built by the Space Research Centre, University of Leicester, was an important supporting instrument in the payload. Its science aims were to (i) measure the geochemical composition of Martian rocks and soils and (ii) perform an *in situ* radiometric dating of rocks.

The flight model X-ray Spectrometer (FM XRS) was delivered for integration to the Beagle 2 lander in late 2002. Beagle 2 entered the Martian atmosphere on 25th December 2003 but the lander failed to communicate during its first expected radio contact on Christmas Day. The lander did not respond to subsequent attempts to communicate with it and on the 6th February it was declared lost (Sims, 2004). The bulk of the work in this thesis constitutes the work with the flight spare X-ray Spectrometer (FS XRS) in the laboratory.

1.3 Thesis Organisation

Chapter 2 describes the principles of X-ray fluorescence and the X-ray spectrometers that have been successfully deployed on Mars to date. Chapter 3 introduces the Beagle 2 mission and the XRS. This chapter also describes the operation of the flight spare XRS and the facility used for its calibration and testing.

Chapter 4 describes the characterisation of various important aspects of the XRS. The basic parameters associated with XRS spectra such as gain, resolution and spectral artefacts are detailed. The measurements and modelling of the system deadtime and detection efficiency are presented. Finally, the variation of the XRS gain (eV/channel) with temperature of its components is investigated.

Chapter 5 describes the calibration of the XRS to convert raw X-ray pulse height data from the analysis of a geological sample of unknown composition into elemental concentrations. The fitting of peaks and background in spectra to derive X-ray fluorescence intensities of characteristic elemental lines is described. The theoretical basis of the quantitative analysis and the experimental steps taken to calibrate the XRS are outlined.

The next two chapters investigate two aspects of the performance of the XRS. Chapter 6

evaluates the analytical performance of the XRS using three criteria: accuracy, detection limit and fitting precision. The XRS analytical performance is compared with two conventional X-ray spectrometers. Chapter 7 describes the operational performance of the XRS with respect to its science goals. The results of the geochemical composition as analysed by the XRS of a suite of basalts is presented. The analyses of Potassium content in these basalts are used in conjunction with Argon isotope analyses by a laboratory version of the Beagle 2 Gas Analysis Package (GAP) to demonstrate radiometric dating via the $^{40}\text{K}\rightarrow^{40}\text{Ar}$ technique. Conclusions are given in Chapter 9 along with a discussion of future research.

Chapter 2

***In situ* X-ray Fluorescence Spectroscopy for Mars**

This chapter describes the technique of X-ray fluorescence spectroscopy for the geochemical analysis of Martian rocks and soils. The X-ray spectrometers that have been successfully deployed on Mars are described. For each instrument, this chapter provides an overview of its science objectives in relation to those of its mission, a technical description, a summary of its calibration and a brief description of the key results from its analyses of the Martian surface.

2.1 X-ray Fluorescence Spectroscopy for Geochemical Analyses on Planetary Surfaces

The technique of X-ray fluorescence is well established (Van Grieken and Markowicz, 2002; Jenkins et al., 1995) particularly for the geochemical analysis of silicate rocks (Potts, 1987) and there is a considerable heritage for the deployment of X-ray Fluorescence Spectrometers on planetary surfaces (for a review see Surkov, 1996).

An X-ray or charged particle incident on an atom can interact by photoelectric absorption to ionise the atom and cause the ejection of a K-, L- or M- orbital electron. The vacancy in the shell is filled by an electron from a higher shell; this transition causes the emission of either a fluorescent X-ray or an Auger electron. Qualitative identification of the elements in the spectrum is governed by Moseley's Law (Moseley, 1913, 1914) which relates the wavelength of the X-ray emission (λ) to the atomic number of the element (Z) by:

$$\frac{1}{\lambda} = k(Z - \sigma)^2, \quad (2-1)$$

where k is a constant for a particular series of lines (K, L, M, etc) and σ is the shielding constant for a particular shell ($\sigma = 1$ for the K shell).

Quantitative analysis of the composition of a sample uses the measured intensity of fluorescent X-rays from each element to calculate its concentration in the sample under analysis (Potts, 1987). The quantitative calibration is based on the analysis of geochemical reference materials (Chapter 5, Section 5.2) that consist of geological materials that have a composition known to a

high degree of accuracy. The Fundamental Parameter method (Chapter 5, Section 5.4) is implemented for quantitative analysis and models the basic equation of excitation relating intensity to the concentration. In X-ray fluorescence analysis of complex samples, such as silicate rocks, the intensity of the observed fluorescence line is not solely dependent upon the concentration of the analysed element but is affected by the concentration of all the other elements in the sample (called the 'matrix'). These are called 'matrix effects' and arise predominantly from (i) attenuation of the incident primary X-rays, (ii) attenuation of the fluorescence radiation, (iii) secondary fluorescence. The latter matrix effect arises from the absorption of fluorescent X-rays from one element by the atoms of another element to induce X-ray fluorescence. For example, Si K_{α} X-rays at 1.74 keV can be absorbed by Al atoms, which have an absorption edge at 1.56 keV, instead of escaping from the sample. This results in an enhanced Al K_{α} line intensity relative to Si K_{α} .

The X-ray fluorescence spectroscopy technique has been used by several instruments *in situ* on Mars; these are the Viking X-ray fluorescence Spectrometer (XRFS), the Mars Pathfinder Alpha Proton X-ray Spectrometer (APXS) and the Mars Exploration Rovers Alpha Particle X-ray Spectrometer (also with the acronym APXS). These instruments are described in Sections 2.2, 2.3 and 2.4.

2.2 The Viking X-Ray Fluorescence Spectrometer

The primary objective of the Viking 1 and 2 missions was to find evidence of active or extinct biology on Mars. The lander (Figure 2.1) carried instruments to achieve the scientific objectives of the lander mission: to study the biology, chemical composition (organic and inorganic), meteorology, seismology, magnetic properties, appearance and physical properties of the Martian surface and atmosphere (Soffen and Young, 1972). The Viking 1 lander arrived at Mars on 20th July 1976 at Chryse Planitia and Viking 2 landed on 3rd September 1976 at Utopia Planitia.

The original science payload selected for the Viking mission did not include the XRFS but focussed instead on instruments for the detection of biological substances on Mars. However, the demonstration of a prototype XRFS (Clark and Baird, 1973) and the strong scientific case for its inclusion to complement the rest of the payload meant that this instrument was eventually added two years after the other instruments were selected.

The XRFS, described in Toulmin et al. (1973), was an energy dispersive instrument with primary excitation provided by ^{55}Fe and ^{109}Cd radioisotope sources and the fluorescence X-rays detected

by four Gas Proportional Counters (GPCs). The Full Width Half Maximum (FWHM) resolution of the GPCs was 1.2 keV at 5.9 keV. The radioisotope sources had a high specific activity (at ≥ 500 Ci/g) and were collimated to prevent the direct detection of X-rays by the GPCs. The detected fluorescence X-rays were converted into voltage pulses via the supporting electronics and were digitised by a single channel analyzer circuit that binned the output consecutively into one of 128 energy levels for 7 – 200 s per channel.

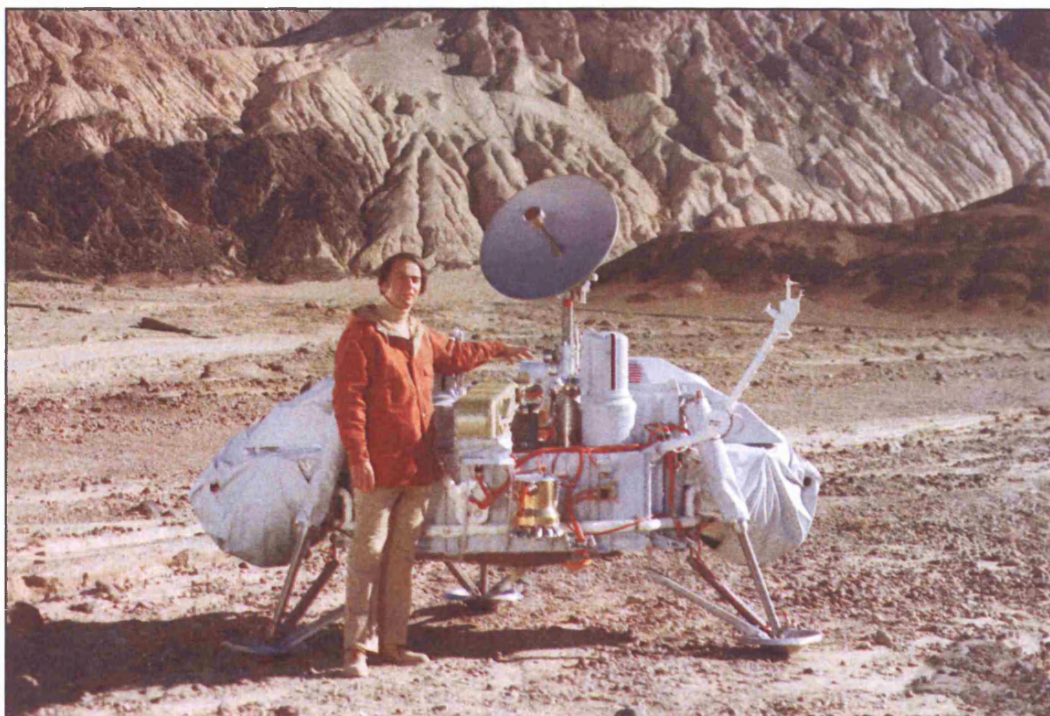


Figure 2.1 A model of the Viking lander in the Nevada Desert with Carl Sagan (image courtesy of NASA).

The XRFS physical arrangement inside the lander is shown in Figure 2.2. The sample was delivered via a funnel which had a screen with 1.2 cm openings to remove any larger pieces from entering and jamming the 2.5 cm diameter delivery chute. The sample was delivered into a sample cavity which was a vertical square prism of dimensions $2.5 \times 2.5 \times 3.8$ cm and capable of retaining a maximum capacity of ~ 25 cm³ of regolith material. After a measurement was completed, the sample was deposited into a dump below the sample cavity which was 600 cm³ in volume. A vibrating trapdoor was located at the bottom of the sample cavity to shake off any adhering fines to the walls and bottom of the chamber.

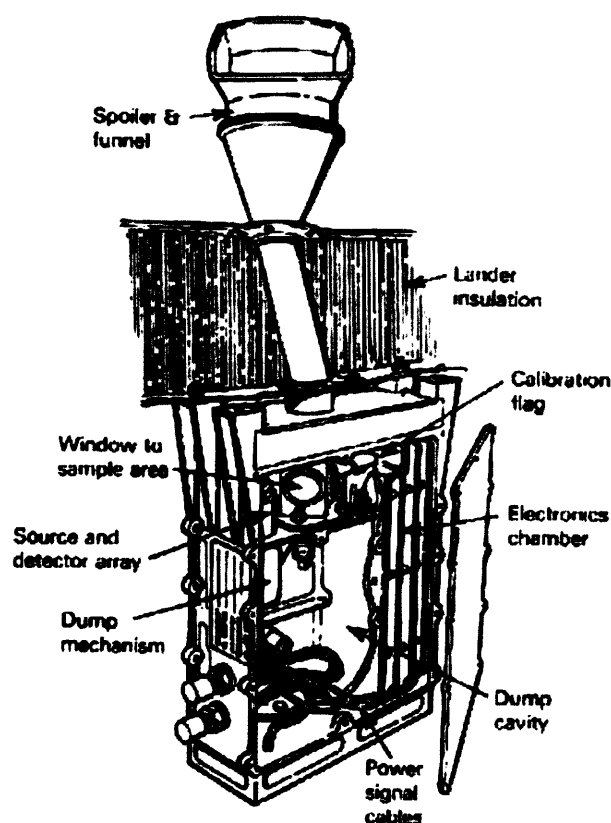


Figure 2.2 Schematic of the XRFs in the Viking lander (after Toulmin et al., 1973).

The physical arrangement of the sources, detector and sample is shown in Figure 2.3. Each source had two gas proportional counters either side of it. The sample cavity had windows on two of its walls composed of synthetic polymers (polycarbonate and polyimide) supported by a metal mesh (Ni for the ^{55}Fe window and Al for the ^{109}Cd window) which allowed efficient transmission of primary and fluorescent X-rays while being robust enough to keep the sample contained within the cavity.

The ^{55}Fe radioisotope emits Mn K X-rays at 5.9 and 6.5 keV and Mn L X-rays at 0.637 and 0.649 keV. The decay of each ^{55}Fe atom occurs solely by electron capture where an electron, from the K or L shell, is captured by the nucleus and combines with a proton to form a neutron. This produces a ^{55}Mn atom with a vacancy in its K or L shell which an electron from a higher shell fills and this process results in the emission of a Mn K X-ray. The ^{109}Cd radioisotope atoms also decay by electron capture and emit Ag K X-rays at 22.2 and 24.9 keV, Ag L X-rays at 2.98 keV and 3.15 keV and an 88 keV gamma-ray.

Flanking the ^{55}Fe source were detectors PC-1 and PC-2. PC-1 was optimised for Mg and Al; PC-2 for Si, S and Cl; and both had a good response for K, Ca and Ti. PC-3 and PC-4, situated either side of the ^{109}Cd source, were intended for the analysis of higher Z elements, namely Fe and certain trace elements (Rb, Sr, Y and Zr). Each pair of GPCs contained gases of various compositions (Table 2.1) to optimise their quantum efficiency to fluorescent X-rays resulting from the primary radiation of their associated source. After review of the operational performance of the detectors on Mars, PC-1 was primarily used to derive the concentrations of K, Ca and Ti, PC-2 to derive the values for Si, S and Cl and PC-4 was used to derive Fe and trace element data.

PC	Gas Composition	Window Material
1	20% Ne, 75% He, 5% CO ₂	5 μm Al
2	10% Xe, 73% Ne, 10% He, 7% CO ₂	25 μm Be
3	40% Xe, 47% Ne, 10 % He, 3% CO ₂	50 μm Be
4	40% Xe, 47% Ne, 10% He, 3% CO ₂	25 μm Be

Table 2.1 XRFS Proportional Counter Detectors with gas composition and window material (after Clark et al., 1977). The gas composition and window material for each proportional counter were selected to optimise the quantum detection efficiency for various spectral ranges.

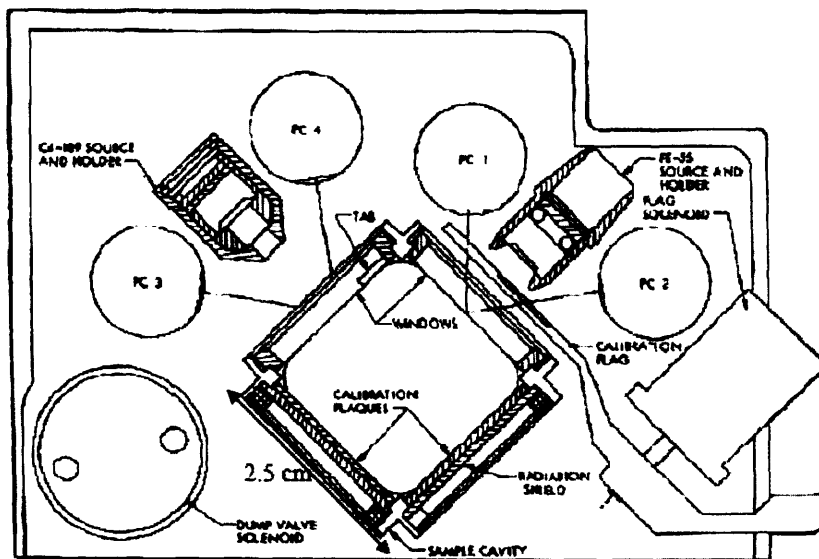


Figure 2.3 Schematic of the sample cavity with GPCs and sources showing the source – sample – detector geometry (after Clark et al., 1977).

Since there was a major overlap between Al and Si, owing to the poor resolution of the GPCs, PC-1 had an Al window to filter out the Si K X-rays and transmit Mg K and Al K X-rays. PC-2 had a Be window which transmitted all low energy X-rays. By comparing the results from the two GPCs, the concentration of Al and Si was determined to a greater accuracy than by using PC-2 alone. However, the Al window itself fluoresced which introduced a higher uncertainty for the concentration of Al.

The XRFS employed a variety of calibration targets (Figure 2.4). There were two calibration targets (called calibration plaques) consisting of circular metal plates (2.5 cm in diameter) opposite each source. Primary X-rays from the sources were incident on these plates when the sample cavity was empty. The plaque opposite the ^{55}Fe source was composed of Al; the plaque opposite the ^{109}Cd was composed of Ag with a central triangular strip of ZnO. This strip was used to determine the level of fill in the sample cavity based on the intensity of the Ag:Zn line ratio in spectra. The fluorescence X-rays from these materials, including the Mn K and Ag K Rayleigh backscatter peaks from the sources, meant it was possible for an energy calibration to be performed using X-rays with energies at regular intervals in the GPCs' spectral range.

In addition to the calibration plaques, a calibration flag was employed that could be inserted between the ^{55}Fe source and detectors PC-1 and PC-2 (Figure 2.3). The flag consisted of an Al plate on which a pellet of CaCO_3 was mounted. This calibration target was employed to compare the profile of a pure Ca peak in the spectrum of the pellet to one mixed with Potassium in spectra of Martian fines. The Potassium and Calcium peaks greatly overlapped in XRFS spectra and appeared as a single peak whose profile was influenced by the relative K:Ca concentration.

The flight instruments were calibrated (Clark et al., 1977) before final instrument installation with 25 calibration samples consisting of solid rock and minerals. These samples were analysed after the instrument had undergone engineering qualification (sterilisation, vibration, thermal vacuum, etc.). Four 'performance standards' were also employed to judge the performance of the instrument before and after engineering qualification. All were in the form of rock slabs because powdered samples could have contaminated various parts of the lander and compromised its reliable operation.

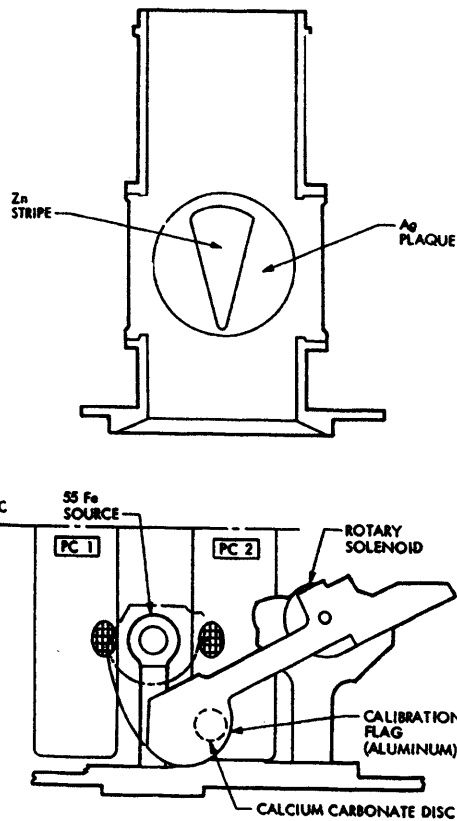


Figure 2.4 The calibration plaque for the ^{109}Cd source and the calibration flag for the ^{55}Fe source (after Clark et al., 1977).

The quantitative analysis of the spectra was based upon a model of the instrument response combined with a correction for matrix absorption and enhancement effects (Clark et al., 1977). The instrument response model included the spectral response for each characteristic emission line (from measurements of pure elemental samples and the quantum efficiency). Each spectrum was normalised to the backscatter peak (either the Mn K or Ag K peak) from the radioisotope sources. The spectrum was compared with a library of spectra to provide an initial estimation of the elemental composition. The elemental concentrations were adjusted iteratively such that the modelled spectrum agreed with the measured spectrum. Finally, each elemental concentration was multiplied by a factor to correct for inaccuracies in the model and established by analysing a suite of geochemical reference materials.

For operations on Mars, the Viking landers had a retractable boom that was capable of sampling a semicircular area approximately 3 m wide and 170° in azimuth for delivery to the XRFS (Figure 2.5). On the end of the boom was a sampling device that consisted two jaws, one of which was moveable, to make an opening of dimensions 4×2 cm in cross section. The sampling

device also had a 'backhoe' trenching device that could be employed to make trenches. This sampler offered some flexibility in the sampling strategies employed for the XRFS (Baird et al., 1977). For example, the lower jaw of the sampler contained a mesh with 2 mm holes through which material could be sieved by vibration of the arm. Generally, sampling was performed to the full capacity of the cavity of the instrument.

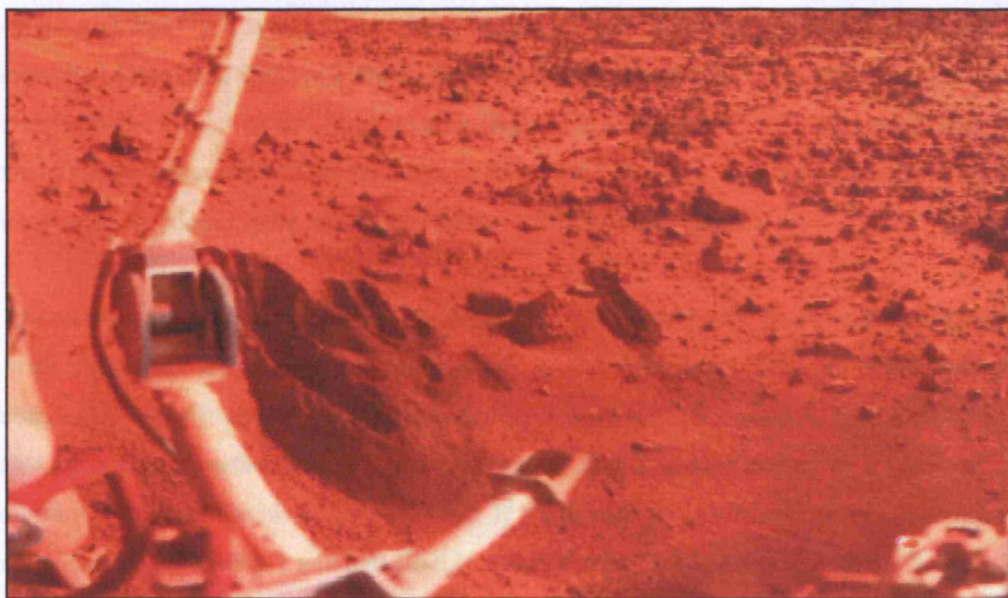


Figure 2.5 Trenches dug by the sampler (at lower centre) at the Viking 1 lander site in the sandy flats location. The boom (at top left) carried the meteorological sensors (image courtesy of NASA).

The sample types analysed on Mars were classified into fines, duricrust and bulk (Baird et al., 1977). The fines were obtained by sieving through the sampler mesh into the receiving funnel of the XRFS. These fines came from different microsites in the accessible vicinity of the lander and included 'protected' fines that were from deep trenches or below rocks. Duricrust (consolidated formation of fines) was observed at both sites and sampled by sieving while the arm was away from the lander to remove the fines material followed by delivery to the XRFS. However, duricrust was not successfully sampled at site Utopia Planitia because it disintegrated during the sieving process. The bulk samples were obtained by opening the jaws of the sampler to release its entire contents into the funnel inlet. Several attempts were made to sample small pebbles sized rocks but these were not successful because of the paucity of such samples at the site.

The final results of the XRFS analyses by both Viking landers are given in Clarke et al. (1982) with interim results in Clark et al. (1976a). Over 2 years of instrument operation, 21 samples were delivered to the XRFS of which 17 were analysed to high precision. The concentrations were reported for the elements Si, Al, Fe, Mg, Ca, K, Ti, S and Cl. For some samples Rb, Sr, Y and Zr were reported. The spectra of the first samples analysed at Chryse Planitia (S1) and Utopia Planitia (U1) are shown in Figure 2.6. For comparison, spectra of other analogue materials are also presented. 8063 is a syenogabbro (from Empire, Colorado), 8064 is a biotite peridotite (from Caribou, Colorado) and 8066 is a shale (from Knoxville, Tennessee). The spectrum U1 shows a clear peak in the region of Rb, Sr, Y and Zr (after Clark et al., 1977). Compared to any simple igneous rock unit encountered on the Earth or Moon, the Martian samples analysed by the XRFS were lower in Al, higher in Fe and much higher in S and Cl concentrations.

The chemical composition of the fines (including the protected fines) contained abundant Si and Fe, with significant concentrations of Mg, Al, S, Ca and Ti. This composition was almost indistinguishable between the two lander locations that were 6725 km apart. This implied Mars is covered by a single surface regolith unit component that is homogeneous as a result of global eolian transport. Only the elements S, Cl and Ti had appreciable differences in concentration in protected fines. The Viking 1 site had slightly more Ti and Cl but less S than at the Viking 2 site. There was a strong correlation between the concentrations of Ti and Fe which was expected from the fact that Ti is commonly found as an interstitial substitute for Fe in many iron-bearing minerals.

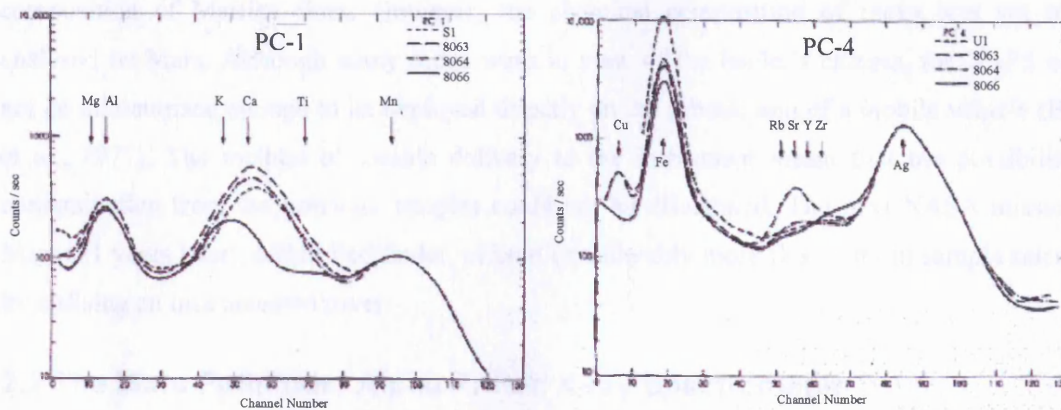


Figure 2.6 Spectra of geological materials analysed on the Martian surface by (left) the Viking 1 XRFS at Chryse Planitia (S1) excited with ^{55}Fe and detected by PC-1 and (right) the Viking 2 XRFS at Utopia Planitia (U1) excited by ^{109}Cd and detected by PC-4 (b).

At the Chryse site, four samples of Duricrust were analysed which contained 50% higher S than the fines. At Utopia Planitia, where no duricrust was sampled, the S content between the sampled fines had little variation. These duricrust samples were interpreted as sulphate salt-enriched cemented variations of the fines material from interaction of volcanic gases with surface material. Upper limits were assigned for 0.5 % K₂O and the atmospheric level of Ar at 0.15 millibar (Clark et al., 1976b). At both sites, the trace elements Sr, Y and Zr were detected (Clark et al., 1976a) at concentrations near or below 100 parts per million (Table 2.2). Rb was apparently below the limit of detection. Overall, these results could not discriminate between the various explanations for the origin of the fine material but it was concluded that they certainly had a primitive mafic or ultramafic origin.

Element	Chryse Planitia	Utopia Planitia
Rb	≤ 30	≤ 30
Sr	60 ± 30	100 ± 40
Y	70 ± 30	50 ± 30
Zr	≤ 30	30 ± 20

Table 2.2 Trace element abundances at two sites on Mars expressed as ppm (after Clark et al., 1976a).

The Viking XRFS instruments performed the first *in situ* measurements of the chemical composition of Martian fines. However, the chemical composition of rocks was yet to be analysed on Mars. Although many rocks were in view of the lander's camera, the XRFS could not be miniaturised enough to be deployed directly on the robotic arm of a mobile vehicle (Baird et al., 1977). The method of sample delivery to the instrument meant that the possibility of contamination from the previous samples could not be discounted. The next NASA mission to Mars (21 years later), called Pathfinder, offered considerably more flexibility in sample selection by utilising an instrumented rover.

2.3 The Mars Pathfinder Alpha Proton X-ray Spectrometer

The NASA Mars Pathfinder mission was intended primarily as a demonstrator for new Mars landing technology. Pathfinder successfully landed at Ares Vallis in a region called Chryse Planitia on 4th July 1997. Its payload consisted of three scientific instruments: the Imager for Mars Pathfinder (IMP), the Alpha Proton X-ray Spectrometer (APXS), and the Atmospheric

Structure Investigation / Meteorology Package (ASI/MET). The Pathfinder rover, called Sojourner, was equipped with the APXS to measure the geochemical composition of Martian geological materials (Figure 2.7). In particular, this mobility meant the APXS could make the first direct measurements of rocks whereas previously their geochemical composition had to be inferred from the Viking XRFS analyses and the Martian meteorites. Key science results from the mission were reported regarding geology and geomorphology; mineralogy and geochemistry, surface material properties, atmosphere and meteorological properties, magnetic properties of the regolith and the rotational and orbital dynamics of Mars (Golombek et al., 1997).

The APXS (described in Rieder et al., 1997a) consisted of two parts: the electronics box and the sensor head (Figure 2.8). The sensor head contained the alpha, proton and X-ray detectors and ^{244}Cm radioisotope sources and was mounted on the APXS deployment mechanism (ADM) on the front of the rover. The electronics box was located inside the warm electronics box (WEB) inside the rover. The ADM permitted the APXS to be deployed against rock or soil samples in a variety of positions.

The sensor head had a diameter of 52 mm and length of 80 mm; the electronics box had dimensions of $71 \times 81 \times 65$ mm. The instrument had an overall mass of 600 g with a power consumption of 340 mW. A typical measurement took 10 hours, which was split into several shorter measurements.

The APXS analysed the elemental composition of rocks and soils using (i) X-ray fluorescence Spectroscopy, (ii) Rutherford backscattering of alpha particles and (iii) emission of protons from (α , p) reactions. The first two techniques are complementary; the alpha particle backscattering mode is sensitive to light elements (C, O), whereas the X-ray fluorescence mode is sensitive for elements Na to Fe (Brückner et al., 2003).

The nine ^{244}Cm radioisotope sources in the sensor head emit both X-rays and alpha particles. The X-rays were from ^{240}Pu (the daughter of ^{244}Cm) that emits Pu L lines (predominantly at 14.3 and 18.3 keV). The ^{244}Cm sources also emit alpha particles of which 76.7% are of energy of 5.8 MeV and 23.3% of energy 5.766 MeV (Lederer et al., 1967). The total activity of the sources was 45 mCi (1.7 GBq). X-ray fluorescence from the sample was induced by (i) incident primary Pu L X-rays and (ii) alpha particle induced X-ray emission (PIXE). The two modes of excitation are complementary (Omand et al., 2005). Alpha particle excitation has a high K shell ionisation cross

section for low Z elements but the cross section decreases rapidly for increasing Z . In contrast, for X-ray excitation with the Pu L X-rays, the ionisation cross section increases with increasing Z . Thus the two modes of excitation used simultaneously are suited to induce X-ray fluorescence for both low Z elements (using alpha particles) and higher Z elements (using Pu L X-rays).

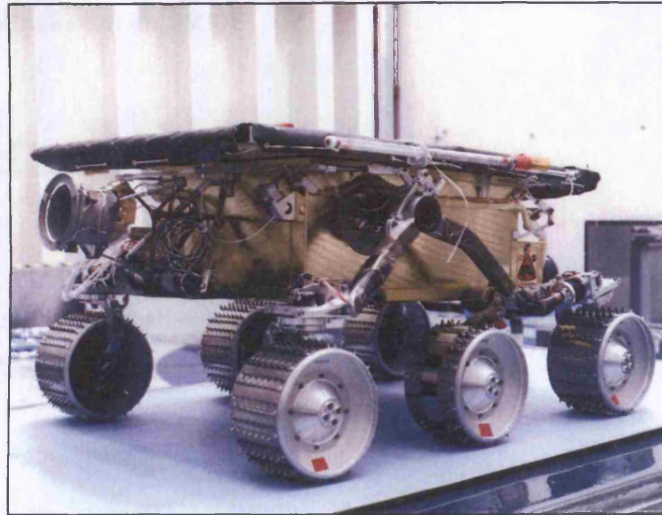


Figure 2.7 The Sojourner rover equipped with the APXS. The rover has a mass of 11 kg and is 280 mm high, 630 mm long and 480 mm wide. The APXS sensor head is shown on the front of the rover attached to the ADM (image courtesy of NASA).

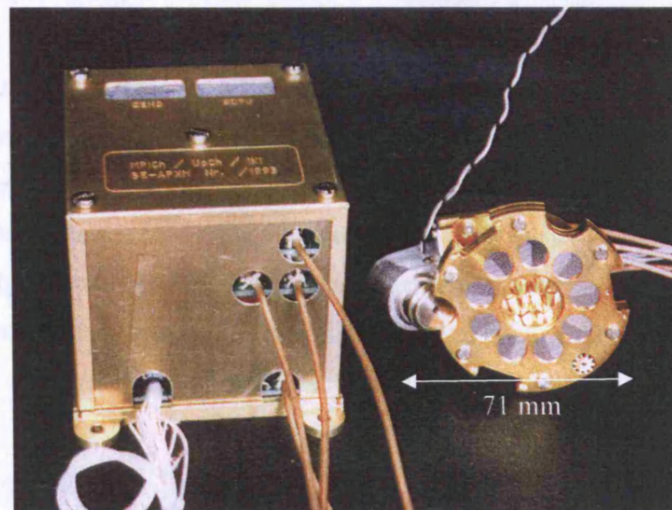


Figure 2.8 A photograph of the Pathfinder APXS sensor head (right) with electronics box (left). The 7 inner circles on the sensor head are the alpha particle detectors, the 9 outer circles are the ^{244}Cm sources. The cylindrical object on the left pointing towards the centre is the X-ray detector (after Rieder et al., 1997a).

The Rutherford backscattering technique, developed by Turkevich (1961), is a complementary method for geochemical analyses, and was implemented by the Surveyor lunar landers (for example, Turkevich et al., 1969). Alpha particles incident on a material can backscatter off the nuclei of the constituent elements. The energy E of a scattered alpha particle in relation to its initial energy E_o , is a function of the atomic mass A of the target atom and the scattering angle θ and is given by (Rutherford et al., 1930):

$$\frac{E}{E_o} = \left(\frac{4 \cos \theta + (A^2 - 16 \sin^2 \theta)^{0.5}}{A + 4} \right)^2. \quad (2-2)$$

The APXS operates in backscattering mode, where the angle of scattering is constrained to approximately 180° , and Equation 2-2 becomes:

$$\frac{E}{E_o} = \left(\frac{A - 4}{A + 4} \right)^2. \quad (2-3)$$

The energy spectrum of the backscattered alpha particles is characterised by (i) the maximum energy at which alpha particles are measured (determined by Equation 2-3) which provides information on the elemental makeup of the target and (ii) the intensity of the particles which gives information on the relative elemental composition (Patterson et al., 1965). For an infinitely thin sample composed of a single element, the alpha particles will lose no energy traversing the sample and the energy spectrum will consist of a single peak. However, for an infinitely thick sample, the alpha particles scatter from a range of depths from the surface of the sample to up to 10s of μm deep. Alphas scattered from deeper in the sample lose energy during the entry and exit and the resulting energy spectrum has a shelf like structure with a step. The height of the step corresponds to the concentration of an element and the energy of the edge is indicative of the element (, right).

The alpha particles, protons and X-rays were detected by different types of solid state detectors (Rieder et al., 1997a). The backscattered alpha particles were detected by a silicon detector (35 μm thick). At the rear of each alpha particle detector was a 700 μm silicon detector that suppressed the charged-particle cosmic ray background. Protons emitted from the sample,

originating from bombardment of alpha particles, were detected by the 'sandwich' of these two detectors. However, for APXS measurements on Mars, the proton signal was so weak as to render this mode redundant. The alpha particle spectra from Mars (, left) contain a significant carbon peak that arises from alpha particles from the source that backscatter from the Martian atmosphere, composed predominantly of CO₂, and are subsequently detected.

The X-rays were detected by an Amptek Si-PiN diode (Redus et al., 2001) with a resolution of ~260 eV at 6.4 keV (Fe K_α). The diode was mounted on a Peltier cooler (used for laboratory testing only), the front end of a charge sensitive preamplifier and a temperature sensor. These components were enclosed in a housing 12 mm in diameter and 10 mm thick with a 8 μm Be window mounted on its front. The detector employed a tungsten collimator to shield the detector from the X-rays and Gamma-rays originating from the ²⁴⁴Cm sources. The electronics processed the pulses from the detectors, measured their amplitudes and binned them into one of 256 bins.

The Pathfinder APXS underwent a preliminary calibration at the Max-Planck Institut für Chemie (Mainz, Germany) with initial results were reported in Rieder et al. (1997a) but an extensive recalibration was later performed by Brückner et al. (2003) and Foley et al. (2003a). Fitting of X-ray spectra was challenging because of the poor energy resolution of the detector. For example, the spectral lines Na, Mg, Al, Si, P, S, Cl heavily overlapped. To improve on the simple Gaussian peak fitting, measurements of pure elemental samples were made to derive the peak shapes for K_α and K_β lines in addition to escape peaks. The peaks deviated from an ideal Gaussian shape with a shoulder on the low energy side that changed shape as a function of energy. Therefore, a weak peak next to a large one could contain a considerable amount of counts from its neighbour. The peak areas were converted into concentrations using a program that incorporated a Fundamental Parameter model that took into account the instrument geometry, excitation by X-rays and alpha particles and matrix effects in the sample. The program also used the measured relationship between the elemental X-ray intensities and corresponding concentrations in geochemical reference materials and meteorites.

The final results from the Pathfinder APXS, summarised below, are given in Foley et al. (2003b) and Brückner et al. (2003) with interim results given in Wänke et al. (2001). In total measurements of five rocks and six soils in total were made over the lifetime of the mission with the APXS measurements performed at night. The X-ray spectrum of rock 'Barnacle Bill' and the alpha particle spectrum of rock 'Wedge' is shown in .

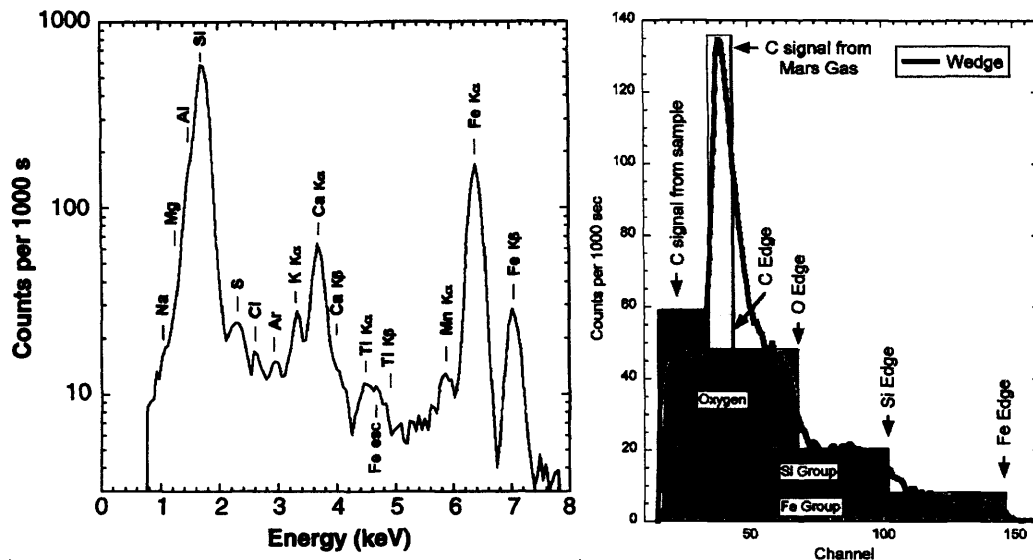


Figure 2.9 (Left) APXS X-ray spectrum of rock ‘Barnacle Bill’ showing constituent elemental lines (after Rieder et al., 1997b). (Right) Alpha particle spectrum of rock ‘Wedge’ showing main elemental contributors. The spectrum shows a large component of atmospheric carbon but an absence of a carbon signal from the rock (after Brückner et al., 2003).

The rocks at the Mars Pathfinder site were covered by various amounts of dust (Figure 2.10). The short penetration depths of the X-rays and alpha particles from the ^{244}Cm sources meant that analyses were not purely of the bulk rock composition but included a dust component. The geochemical composition of the soils showed a remarkable similarity with soils at the Viking 1 and 2 landing sites. This provided further evidence that mixing via global dust storms have generated a globally homogeneous regolith unit. The soils had a high concentration of S which confirmed the Viking results. Since the concentration of S in rocks was expected to be small, the S content was used as a marker for the amount of covering of dust on rocks in order to ‘subtract’ its composition. The mean soil sulphur concentration was 2.7% while the S concentration of rocks was 0.8% to 2.0% which exceeds by far the concentrations encountered in igneous rocks. An upper level of 0.3% sulphur was chosen for rocks based on Martian shergottites meteorites.

The compositions of the rocks (high Si and low Mg) implied that they were felsic (more evolved) in contrast to the mafic rocks inferred from the composition of the Mars meteorites and Viking soil results. There was a higher K content (at 0.5%) in the soils than at the Viking sites (which set an upper limit of 0.12% K) which implied that the soil was K-enriched by a contribution from the local rocks (whose soil-free K component was 1.1%).

The alpha mode of the APXS detected no carbon in any of the rocks or soils, although there was a significant component of atmospheric carbon from CO₂. It was concluded that any carbon, if present, was at levels below the detection limit of 0.8%. However, tests with a copy of the instrument were able to successfully detect carbon in the Mars meteorite ‘Murchison’ under Martian atmospheric conditions (Brückner et al., 2003).

The Pathfinder mission succeeded in demonstrating the lander technology and paved the way for the more ambitious Mars Exploration Rovers (MER). Although the Pathfinder mission was successful in allowing the APXS instrument to be deployed on a rover to analyse rocks, there was no ability to prepare rock surfaces. This meant it was difficult to infer the bulk composition of the rocks that had a veneer of dust and/or a geochemically distinct weathered rind. The enhanced payload of the MER rovers addressed this shortcoming with the inclusion of a rock preparation tool.



Figure 2.10 The Sojourner rover on Mars with the APXS deployed by the ADM to analyse rock ‘Yogi’ (image courtesy of NASA).

2.4 The Mars Exploration Rovers Alpha Particle X-ray Spectrometers

The Mars Exploration Rovers mission (shown in Figure 2.11) has the overarching science objective to search for evidence of past and current water activity on the surface of Mars (Squyres et al., 2003). Water is one of several essential prerequisites for life. The mission

consists of two identical rovers called 'Spirit' and 'Opportunity'. Spirit landed on 4th January 2004 in Gusev Crater and Opportunity landed on 25th January 2004 at Meridiani Planum. At the time of writing, both rovers continue to successfully operate on Mars. The rovers carry a panoramic camera (Pancam) and navigation camera on a mast 1.4 m in height from the base of the wheels. The mast also carries the periscope for the Miniature Thermal Emission Spectrometer (Mini-TES). Three instruments are attached to the robotic arm of the rover, the instrument deployment device (IDD). These are the Mössbauer Spectrometer (MS), Microscope Imager (MI) and Alpha Particle X-ray Spectrometer (APXS). In addition, the Rock Abrasion Tool (RAT) is used for the preparation of rocks. Two hazard cameras are mounted on the front of the rover and two on the rear. In comparison to Pathfinder, the MER APXS not only benefited from the RAT to prepare rock surfaces and remove dust and/or weathering rinds but its analyses could be interpreted in the context of the results from the other instruments.



Figure 2.11 Artist's impression of the Mars Exploration Rover with IDD deployed against a rock (image courtesy of NASA/JPL).

The new APXS (Figure 2.12) instrument for MER is described in Rieder et al. (2003). The new instrument is called the Alpha 'Particle' X-ray Spectrometer since the proton mode was made redundant by improvements in the X-ray mode performance. The instrument has several improved design features based on the 'lessons learned' from the Pathfinder APXS. In particular, the use of a superior X-ray detector, a coaxial arrangement of sources and detectors and

protective doors with a calibration target were some of the primary design changes.

The sensor head is cylindrical in shape, 53 mm in diameter and 84 mm in length with an insulating flange on its end of dimensions 68 × 68 mm. The X-ray detector lies on the central axis of the instrument with a ring of six (instead of nine for Pathfinder APXS) ^{244}Cm sources around it and the rectangular alpha detectors further out. The six sources had a total activity of 30 mCi (1.1 GBq). This new coaxial arrangement of sources and detectors ensured that both sets of detectors see the same part of the sample.

The X-ray detector is a silicon drift detector (Lechner et al., 2004) with a 10 mm² active area and 5 μm thick Be window with an energy resolution of 160 eV at 5.9 keV. The resolution of the X-ray detector is twice as good as the Pathfinder instrument resulting in improvements in the sensitivity by at least a factor of 10 for all elements (for Na by a factor of 50). What were formerly the proton detectors mounted behind the alpha detectors for the Pathfinder APXS are now used to measure the background contribution due to cosmic radiation at the surface of Mars and high energy gamma radiation from the ^{244}Cm sources and Mössbauer source. Both detectors are collimated: the X-ray detector has a Zr collimator; the alpha particle detector has twenty layers of stainless steel foil with a honeycomb structure etched in.

Ti foil covers the sources to prevent contamination of the sample from recoil sputtering of material in the sources. The foil also reduced the energy of the incident alpha particles from 5.80 MeV to 5.17 MeV to reduce the interaction cross section with carbon in CO₂. This foil in combination with the new source-collimator-detector geometry reduced the background signal from Martian CO₂.

Unlike the Pathfinder APXS, the MER APXS has a calibration target mounted on the inside of two doors which have the additional function of protecting the interior components from dust contamination. The doors can be opened by pressing the contact ring at the front face of the sensor head against a surface and closed using a release lever. Both can be done using the IDD thereby avoiding any extra mechanisms for the APXS. The calibration target consists of a set of thin layers of Au, Kapton and Ni on top of the Cu-Be body of the doors. The C in the Kapton provides a suitable target for the alpha particle mode. For the X-ray mode, the Au L and M lines in addition to Ni K and Cu K lines provide peaks across the full energy range of the spectrum from Au M_α (at 2.1 keV) to Au L_γ (at 13.3 keV). An additional calibration target is a pellet

composed of magnetite mounted on the rover chassis that is suitable for both the calibration of the MS, since it is an iron bearing mineral, and also the APXS, since it contains a range of elements whose fluorescence X-rays are detectable by the instrument.

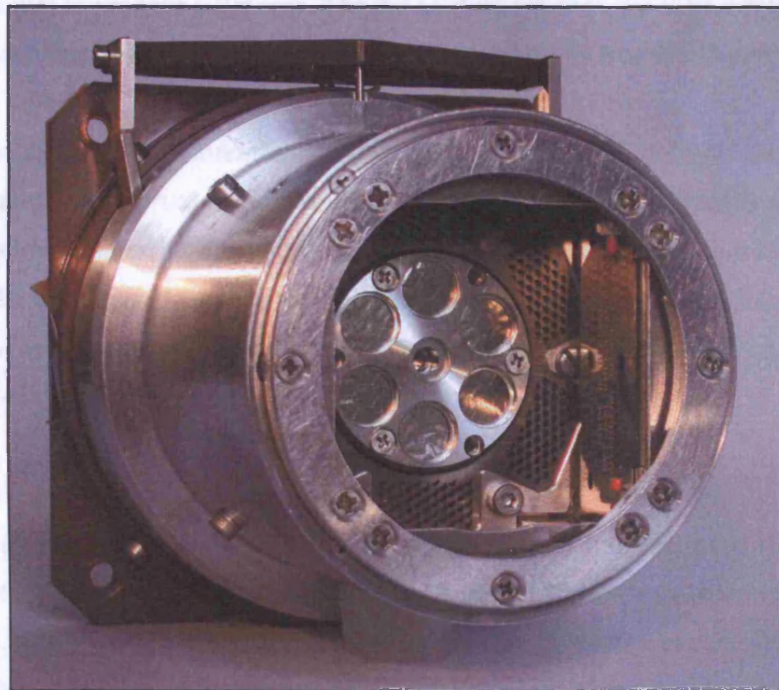
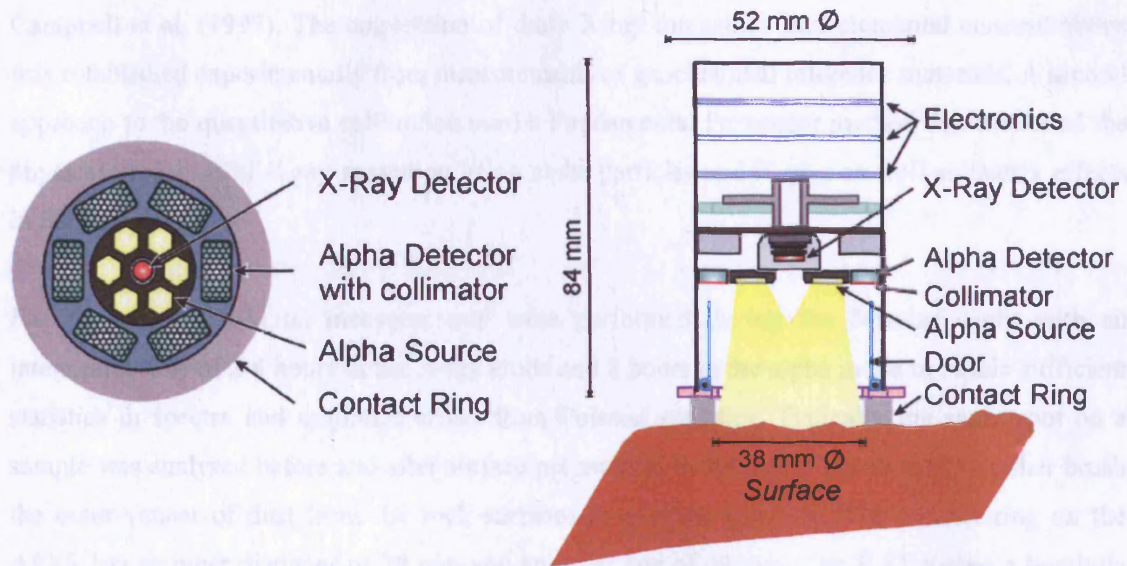


Figure 2.12 The APXS for the MER rovers. (Top) A schematic of its main components. (Bottom) An image of the flight model APXS (after Rieder et al., 2003).

The calibration (Gellert et al., 2006) of the flight instrument was performed using 11 standards (8 geostandards and 3 meteorites) as well as oxide and metal standards. The instruments were calibrated in a vacuum chamber under Mars atmospheric conditions. The fitting of the spectra to derive elemental peak intensities employed a sophisticated model of peak shapes as developed by Campbell et al. (1997). The conversion of these X-ray intensities into elemental concentrations was established experimentally from measurements of geochemical reference materials. A second approach to the quantitative calibration used a Fundamental Parameter method that modelled the physical processes of X-ray excitation using alpha particles and X-rays as well as matrix effects in the sample.

For operations on Mars, measurements were performed during the Martian night with an integration time of 2-4 hours in the X-ray mode and 8 hours in the alpha mode to obtain sufficient statistics in spectra and minimise errors from Poisson statistics. Typically the same spot on a sample was analysed before and after surface preparation by the RAT. It was used to either brush the outer veneer of dust from the rock surfaces or perform grinding. The contact ring on the APXS has an inner diameter of 38 mm and an outer one of 49 mm. The RAT makes a borehole of diameter 45 mm to produce a flat area. The APXS does not fit in the RAT borehole but instead makes its measurements at some close standoff distance, typically less than 5 mm.

The initial results from measurements performed in the first 90 sols at Gusev Crater and Meridiani Planum are reported in Gellert et al. (2004) and Rieder et al. (2004) respectively and summarised below. The major element compositions of the soils matched those at the Viking 1, Viking 2 and Pathfinder landing sites which added yet further evidence for a global mixing of the regolith to produce an approximately homogeneous unit. Again, the soils were characterised by a high S and Cl content.

In the first 90 sols at Gusev, three rocks were analysed called Adirondack, Humphrey and Mazatzal. After grinding by the RAT, the chemical signature (rich in Mg, poor in K) of the rocks were similar to primitive basaltic rocks found on Earth and to basaltic shergottites (a type of Martian meteorites). But the Cl and S levels (the lowest of which were at ~0.15 and ~0.5 % respectively) were higher than in basaltic Martian meteorites. It was suggested that the high Cl and S could originate from some combination of alteration veins, residual dust in vugs (small cavities in rocks) and weathering rind on rock surfaces. For example, the rock Mazatzal had a higher S and Cl compared to the average soil composition and Gobi, the only soil with similarly

high S and Cl, was located close to Mazatzal. This suggested some contamination from the local soil. When the rock was brushed, there were elevated levels of Cl and P and the concentration of Br increased from 30 to 100 ppm. The subsequent grinding then removed almost all the S and Cl, whereas the Br concentration increased further to 170 ppm. This was attributed to a white vein in the rock and an alteration zone observed with the MI which indicated some modification by past aqueous activity. A similar Br/Cl enhancement has been seen for aqueously altered portions of olivine in the Martian meteorite Nakhla. The same chemical signature is also found in terrestrial evaporates from salt lakes.

At the Opportunity landing site in Meridiani Planum, the rover landed in Eagle crater near some rock outcrops. Again the composition of the soil was approximately the same as all other landing sites. All the major elements were present in the same concentrations except for Fe due to the variable amounts of hematite-rich spherules (nicknamed 'blueberries') at the site.

The rocks had a high and variable ratio of bromine to chlorine. The APXS examined a rocky outcrop (Figure 2.13) at the base the Eagle crater wall. For the 'McKittrick' site on 'El Capitan', for which the APXS spectrum is shown in Figure 2.14, the S concentration increased from 5.1% to 8.4% and the Br concentration increased from 270 ppm to 430 ppm after abrading by the RAT. This showed a significant enrichment in the Br to Cl ratio compared to the primitive carbonaceous chondrite ratio.

A direct measurement of the blueberries was performed on an outcrop where there was a large concentration of them in a depression called 'Berry Bowl'. This showed a very high Fe content at 24.1% and a low S. The high Fe:Mn ratio was indicative of an iron bearing mineral hematite which was confirmed in later Mössbauer spectra.

The results at the Opportunity site provided strong evidence for some alteration by water. They suggested that at some time in the site's history, water containing sulphuric (and hydrochloric) acid, derived from volcanic gases, reacted with rocky material to form brines. This would react with olivine to form Mg and Fe sulphates and also silica would have formed. The 'blueberries' were interpreted as spherical mineral structures formed by groundwater percolating through porous rocks. In all, the APXS was successful in detecting the chemical signatures in the rocks and soils at this site that were indicative of interaction with water at some time in its history.

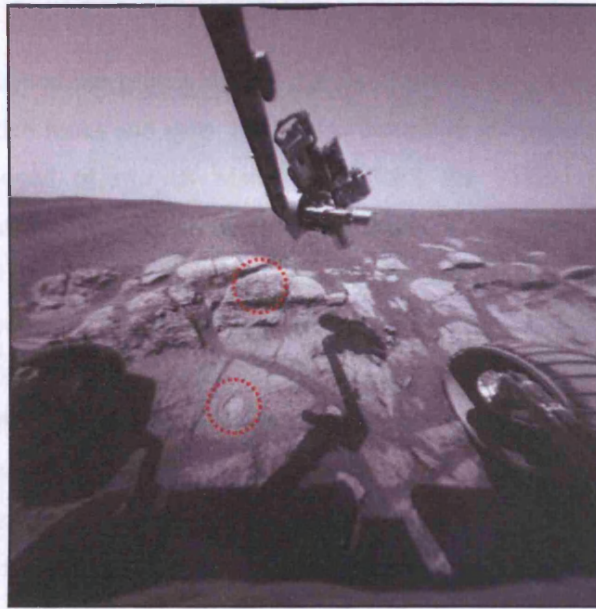


Figure 2.13 Image taken on sol 35 by Opportunity rover's Hazard avoidance camera. The rover is analysing a rocky outcrop, called El Capitan. The red circles indicate areas where the RAT has prepared the surface. The lower hole is on McKittrick, the upper one on Guadalupe (Image courtesy NASA/JPL/Cornell).

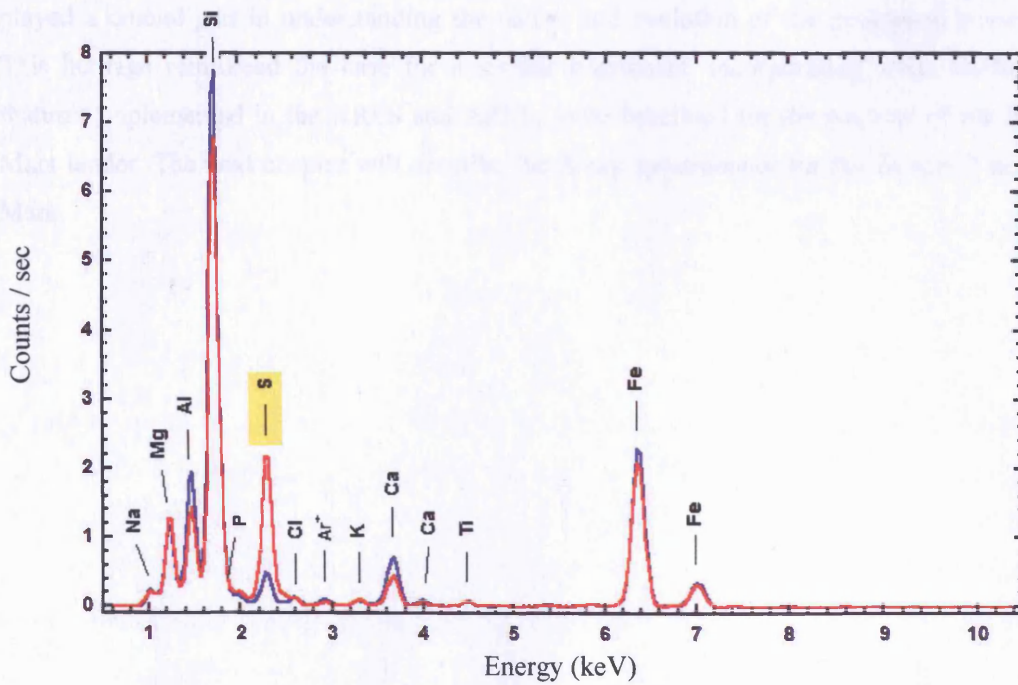


Figure 2.14 APXS X-ray spectrum of 'McKittrick' (red) which has the highest sulphur content ever found on Mars and neighbouring soil (blue) 'Tarmac' (image courtesy of NASA/Max Plank Institute).

2.5 Summary

This chapter has described the principle of X-ray fluorescence as a technique to determine the geochemistry of Martian rocks and soils. It has also described the previous X-ray spectrometers that have been deployed *in situ* on Mars. The XRFS for Viking made the first *in situ* measurements of Martian regolith. It utilised ^{55}Fe and ^{109}Cd sources for primary excitation meaning it was capable of excitation of fluorescence X-rays from a broad range of elements including trace elements Rb, Sr and Zr. However, its poor resolution due to the use of GPCs limited its analytical performance. The APXS for Pathfinder could be highly miniaturised, owing to advances in solid state detector technology, such that it was mounted as part of the Sojourner rover. Its mobility meant it made the first measurements of Martian rocks. However, the ^{244}Cm sources, while being efficient at excitation of low Z elements (from alpha particle bombardment) and high Z elements (from Pu L X-rays), were not capable of excitation of Rb, Sr and Zr like the Viking XRFS. The APXS for the MER rovers had a much improved resolution, owing to the replacement of a Si-PiN diode with a Si drift detector, such that it could clearly separate the K lines of elements Na, Mg, Al and Si (Figure 2.14). The APXS on each MER rover was the first to detect geochemical signatures in rocks and soils that provided strong evidence for alteration by water. For each mission, the geochemical analyses by these X-ray fluorescence spectrometers played a crucial part in understanding the nature and evolution of the geological environment. This heritage reinforced the case for a similar instrument, incorporating some of the design features implemented in the XRFS and APXS, to be baselined for the payload of the Beagle 2 Mars lander. The next chapter will describe the X-ray spectrometer for the Beagle 2 mission to Mars.

Chapter 3

The X-ray Spectrometer for Beagle 2

This chapter describes the scientific objectives and payload of the Beagle 2 mission to Mars. The X-ray fluorescence spectrometer (XRS), one instrument in the payload, is introduced. This chapter describes the operation of the flight model (FM) and flight spare (FS) XRS, the study of which is the subject of this thesis, and the facility used for its calibration and testing.

3.1 Introduction

The Beagle 2 mission was the lander for ESA's Mars Express orbiter (Schmidt, 2003). It was named after the ship HMS Beagle on which Charles Darwin and Robert FitzRoy sailed during 1831-1836. The observations Darwin made during the voyage inspired him to develop his theory of natural selection which led to the publication of the seminal work "The Origin of Species" in 1859. In keeping with the spirit of the Beagle voyage, the primary objective of Beagle 2 was to establish whether life is present or has ever existed on Mars.

Mars Express was launched on 2nd June 2003 from Baikonur aboard a Soyuz-Fregat rocket. The lander was ejected from Mars Express for descent on 19th December 2003 and entered the Martian atmosphere on 25th December. Beagle 2 failed to communicate during its first expected radio contact on Christmas Day. The lander did not respond to subsequent attempts to communicate with it and on the 6th February 2004 it was declared lost. A subsequent inquiry (Sims, 2004) concluded several possible reasons for its loss and outlined key 'lessons learned' to inform the design of future Mars missions.

3.2 The Beagle 2 Lander for Mars

Beagle 2 was due to land in the Isidis Planitia region of Mars (Bridges et al., 2003) and operate for a nominal mission duration of 180 sols. The primary objective of the mission was the detection of extinct and/or extant life on Mars. A supporting objective was an assessment of the biological potential of the landing site in the planet's history. The overall scientific objectives of Beagle 2 were to carry out (Sims et al., 1999):

- i) a geomorphological characterisation of the landing site;
- ii) a geological investigation of the rocks, including light element chemistry, composition, mineralogy, petrology and age;
- iii) a determination of the oxidation state of the Martian surface, both within rocks and at

- protected locations beneath rocks;
- iv) a search for five criteria which would provide strong evidence that life processes could have operated in the past on Mars, namely a) the existence of liquid water either presently or in the past, b) appropriate inorganic minerals such as carbonates, c) carbonaceous debris, d) organic matter of complex structure and e) a certain level of isotopic fractionation of carbon;
 - v) a full characterisation of the composition of the atmosphere and the processes involved in the seasonal climatic changes or diurnal cycling;
 - vi) a search for trace atmospheric species (eg, methane) which would be indicative of extant life at some location on Mars.

The Beagle 2 lander carried a unique science payload designed to achieve these objectives. This payload was capable of allowing Beagle 2 to achieve several exceptional analyses never before attempted on Mars. These include radiometric dating of rocks (see Chapter 8), trace element analysis of rocks and soils, analysis of the subsurface regolith to 1.5 m, and the search for biologically derived trace constituents of geological materials.

The fully deployed Beagle 2 (Figure 3.1) consisted of a main base with a diameter of ~66 cm that was divided into three sectors containing (i) the principal scientific instrument, called the Gas Analysis Package (GAP), (ii) the robotic arm and (iii) the lander systems. There were five solar arrays, one on the lid and four on fold-out petals. The lander had a 9 kg experimental payload mass out of a total landed mass of 33 kg meaning it had the highest payload to support systems mass ratio of any lander for Mars. The robotic arm carried a highly integrated suite of contact instruments called the Position Adjustable Workbench (PAW). The Environmental Sensor Suite (ESS) sensors were positioned at various locations including a solar array petal, the lander body and on the PAW. The scientific instruments and their primary function are detailed in Table 3.1.

The Environmental Sensor Suite (Towner et al., 2004) was designed to investigate and monitor the meteorological conditions at the landing site and assess the astrobiological implications of the local radiation and oxidative environment. This was to have been achieved using several sensors to measure total radiation dose, UV flux, atmospheric temperature, pressure, wind speed and direction, dust characteristics (momentum, direction, rate) and the level of atmospheric oxidisers.

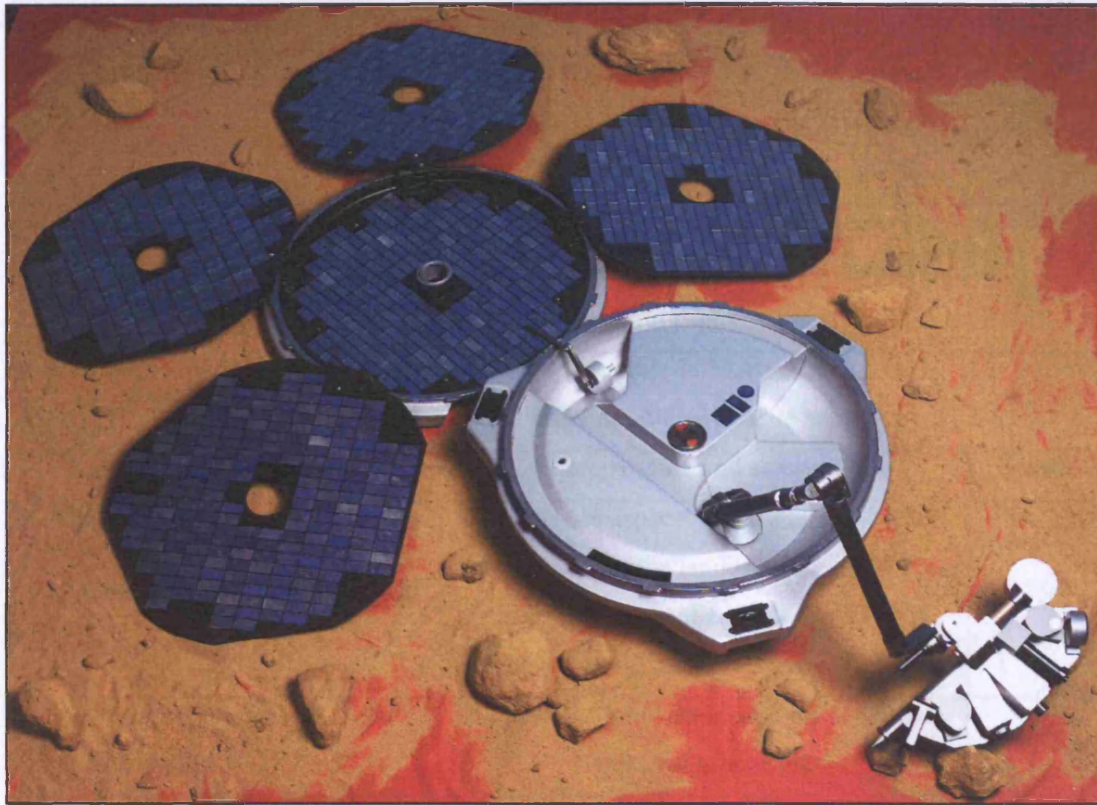


Figure 3.1 A model of the deployed Beagle 2 lander. There are five solar panels in total with one in the 'lid' and four attached around it. The lander base of diameter ~66 cm, is divided into three sectors comprising (i) the principal scientific instrument, called the Gas Analysis Package (GAP), (ii) the robotic arm with a suite of scientific instruments on the end and (iii) the lander systems.

The Gas Analysis package (Wright et al., 2003) was designed to perform many of the investigations associated with the exobiological goals of Beagle 2. It is a miniaturised mass spectrometer capable of conducting three main studies which are (i) the search for organic matter, (ii) analysis of total light element composition and (iii) atmospheric analysis. It is capable of analysing rock, soil or atmospheric samples. It can perform quantitative and stable isotopic measurements of gases including H_2 , N_2 , O_2 and CO_2 . The instrument can also analyse noble gases, including Ne, Ar and Xe, as well as trace constituents indicative of extant life (such as CH_4). A unique aspect of its investigations is its analysis of organic matter. The technique of stepped combustion can distinguish between the various origins of carbon species (particularly organic derived carbon) by the temperature at which they burn in oxygen. This stepped combustion technique also enables a measurement of the level of isotopic fractionation of carbon which is indicative of organically derived carbon.

Instrument	Primary Function	Mass (g)
Mössbauer spectrometer (MBS)	Iron-bearing mineralogy of rocks and soils	540
Stereo Camera System (SCS)	Multispectral stereo panoramic imaging of surroundings	175.5, 174.5
X-ray Spectrometer (XRS)	Geochemistry of rocks and soils	154
Gas Analysis Package (GAP)	Search for organic matter, light element content, atmospheric analysis	5740
Microscope (MIC)	Investigate nature of Martian rocks, soils and fines on particulate scales	151
Rock Corer-Grinder (RCG)	Rock preparation and sampling tool	348
Environmental Sensor Suite (ESS)	Characterise aspects of the meteorological environment of the landing site; investigate astrobiological implications for the local radiation and oxidative environment	156
PLanetary Underground TOol (PLUTO)	Subsurface soil sampling and regolith physical properties	890

Table 3.1 The Beagle 2 scientific payload instruments with their primary function listed.

The PAW (Figure 3.2) carried several instruments and tools designed to be manoeuvred to the target surface by the robotic arm. The Stereo Camera System (Griffiths et al., 2005) consists of two cameras, positioned on opposite sides of the PAW. It can deliver panoramic images of the landing area using multispectral filters. The Microscope can perform close up imaging of rocks and soils (with its own illumination from LEDs) to provide information on surface texture and probe for microstructures of possible biological origin (Thomas et al., 2004). Two spectrometers can carry out a compositional and mineralogical analysis of rocks and soils. The first spectrometer was the XRS for analyses of major and trace element geochemistry (Section 3.3). The second instrument was the Mössbauer Spectrometer (Klingelhöfer et al., 2003) whose primary aim was to identify the relative abundances of iron-bearing minerals in rocks. The Mössbauer spectrometer can be used to conduct several studies including the nature and extent of weathering processes involving iron-bearing phases (Schröder et al., 2004). The payload also included two subsurface sampling tools (Richter et al., 2002). The first tool is the Rock Corer-Grinder which can remove the weathered and dust covered surface layers of rock to expose the ‘fresh’ interior and also sample the rock to deliver rock chippings to the GAP. The second tool is Planetary Underground Tool which is capable of sampling the subsurface regolith by penetrating

vertically into it to depths of 1.5 m. It has a slender cylindrical shape that contains an internal hammering mechanism to propel it forwards with a sampling tip at its leading end. It is also capable of lateral movement across the surface of the regolith and can be diverted underneath boulders for sampling. A calibration target for the XRS, MBS, SCS and MIC was situated on the lander body. It consisted of an aluminium alloy plate that featured disc-shaped depressions into which various minerals were deposited and had an overall appearance designed to appear similar to a 'spot painting' by the popular artist Damien Hirst. Visually the spots were multicoloured and had a texture on the granular scale for calibration of the SCS and MIC. Several of the spots were composed of iron oxides suitable for calibration of the Mössbauer Spectrometer. Other spots were composed of minerals such as Rutile (TiO_2) and Wulfenite (PbMoO_4) that contained elements whose fluorescent X-rays were within the spectral range of detection of the XRS.

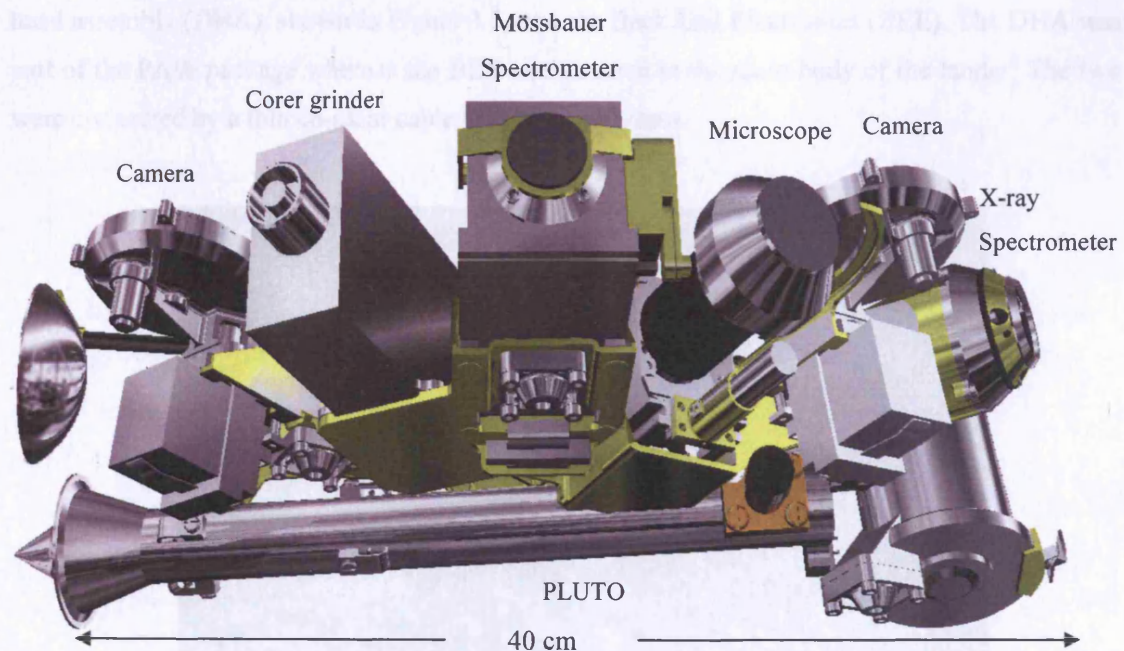


Figure 3.2 Computer aided design image of the Beagle 2 PAW with constituent instruments labelled. PLUTO is shown stowed in its launch tube but with its sampling tip protruding.

3.3 The Beagle 2 X-ray spectrometer

The X-ray spectrometer was an important instrument for the Beagle 2 payload since the determination of the geochemistry of Martian rocks and soils can contribute to an understanding of the origin and evolution of Mars and the implications for the planet harbouring life at some time during its history. The scientific goals of the XRS were to:

- (i) Perform an analysis of the major and trace element composition of rocks and soils.
- (ii) Perform an *in situ* radiometric dating of rocks using the $^{40}\text{K} \rightarrow ^{40}\text{Ar}$ technique with K measured by the XRS and ^{40}Ar measured by the GAP.

The XRS had several similarities with previous X-ray Spectrometers deployed on Mars. It utilised the same radioisotope sources as the XRFS on the Viking landers (Clarke et al., 1977) but the fluorescent X-rays were detected by the same solid state detector as that employed for the Pathfinder APXS (Rieder et al., 1997a).

The XRS was highly miniaturised in order to be accommodated as part of the Beagle 2 lander payload. Indeed, to be accommodated on the PAW it was divided into two parts: the detector head assembly (DHA), shown in Figure 3.3, and the Back End Electronics (BEE). The DHA was part of the PAW package whereas the BEE was situated in the main body of the lander. The two were connected by a thin co-axial cable via the arm harness.

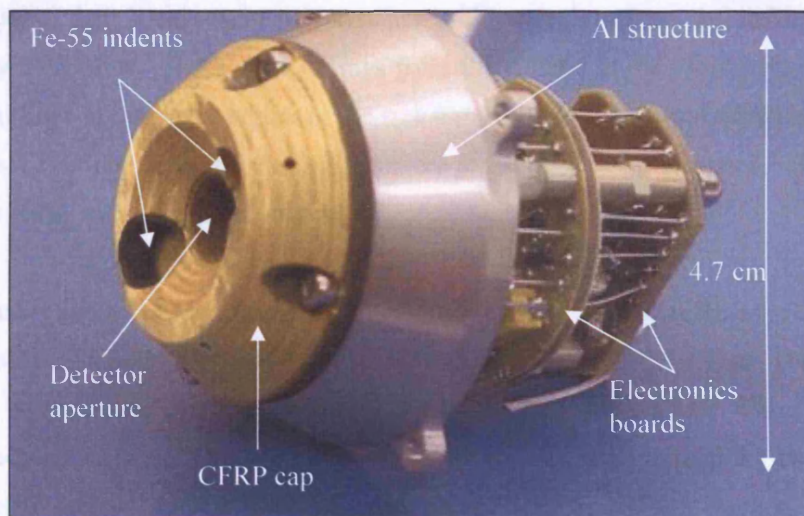


Figure 3.3 The Detector Head Assembly of the XRS with constituent components labelled. The aluminium ring on the CFRP cap is not shown.

The BEE consisted of a single electronics board ($120 \times 80 \times 15$ mm) of mass 98 g. The DHA was approximately cylindrical in shape of diameter 47 mm, height 47 mm and mass 58 g. The DHA consisted of an aluminium cover which housed electronic circuit boards and the Si-PiN diode. A carbon fibre reinforced plastic (CFRP) structure on the front of the Al cover housed the four

radioisotope sources. Two ^{55}Fe sources were mounted in the front of the CFRP structure and two ^{109}Cd sources were mounted in the rear at 90° positions to the ^{55}Fe sources. Uniquely for an X-ray spectrometer, the sample was excited by two types of sources simultaneously as opposed to sequential source excitation used in some terrestrial X-ray Spectrometers (Potts et al., 1995) or single source excitation as with the APXS (Rieder et al., 1997a). The mainly carbon composition of the CFRP structure was chosen so that X-ray fluorescence from the structure (C K at 277 eV) was below the lower energy limit of detection of the XRS. The CFRP structure was not robust enough to make direct contact with rocks and soils and so an aluminium contact ring was mounted on the front of the CFRP structure.

The ^{55}Fe and ^{109}Cd disc-shaped radioisotope sources* decay by electron capture and emit X-rays. The total activity of the ^{55}Fe sources (emitting primary Mn K X-rays) was ~ 60 MBq with a half life of 2.7 years. The total activity of the ^{109}Cd sources (emitting primary Ag K and L X-rays) was ~ 5 MBq with a half life of 1.3 years. The half lives of the sources were long enough for them to have an appreciable activity for the nominal mission duration of 180 sols (~ 0.5 year). The ^{55}Fe and ^{109}Cd sources are well suited to excite the major and trace elements respectively because the primary energies of their X-rays were well matched to the energies of the absorption edges of the elements of interest. However the Ag L X-rays from the ^{109}Cd sources can interfere with the K shell elemental lines in the major region of the spectrum. The sources were therefore mounted at the rear of the CFRP cap such that the L lines were attenuated by 3 mm of carbon that has an extremely low X-ray transmission at ~ 3 keV.

The Si-PiN diode (Figure 3.4) is a reversed biased diode consisting of a positive-type (doped with Boron), intrinsic (no doping) and negative-type (doped with Phosphorus) region. The diode has a layer of gold on each side of it across which the bias voltage is applied. When the diode is reversed biased any free carriers are swept out of the bulk of the material by the field and a depletion layer is created. In this state, the only charge created is from thermal excitation of electrons above the narrow bandgap (1.14 eV at room temperature) of silicon. To minimise the noise from the generation of these charges, the diode is cooled to typically 250 K.

To be detected, a fluorescent X-ray must pass through the p-type layer and interact with the depleted region of the Si-PiN diode. This interaction is typically by photoelectric absorption which creates an inner shell vacancy of a Si atom in combination with an energetic photoelectron.

* Isotope Product Laboratories, 24937 Avenue Tibbitts, Valencia, CA 91355

The energy associated with the inner shell vacancy is absorbed in the crystal following emission of Auger electrons or multiple low-energy X-rays from the atom that create ionisation events. The photoelectron and various Auger electrons travel through the depleted region and ionise other atoms in the crystal lattice to produce secondary electrons. This process ends when the electrons come to the end of their stopping range that is considerably shorter than the thickness of the crystal. The secondary X-rays are absorbed by photoelectric absorption. The result of all these processes is to produce a number of free electron-hole pairs (with a standard deviation given by Equation 4-5) which is proportional to the energy of the incident X-ray (~ 3.68 eV per electron-hole pair). The experimental characterisation of this detector is discussed in Chapter 4.

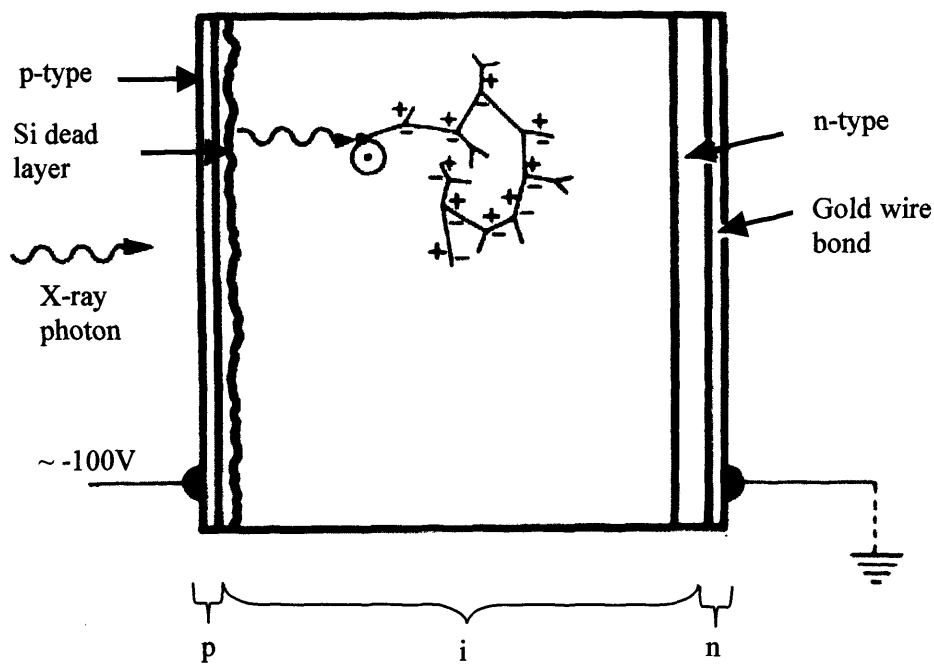


Figure 3.4 A schematic representation of a Si-PiN diode. The constituent positive (p), intrinsic (i) and negative (n) type layers are shown (adapted from Jenkins et al., 1995). The diode is held at a reverse bias voltage of ~ 100 V.

The operation of the XRS is as follows. The Beagle 2 robotic arm positions the XRS DHA such that it is in contact with a target (rock, soil or atmosphere) for a measurement duration of a Martian night (~ 12 hours). The primary radiation from the XRS's radioisotope sources excite fluorescent X-rays from the constituent elements of the sample which are detected by a Si-PiN

diode. Each X-ray deposits its energy in the diode to produce a number of electron-hole pairs in the depleted region. The reverse bias voltage sweeps the electrons towards the rear contact and the total charge is converted into a voltage via a preamplifier that is co-mounted with the diode in the DHA. The preamplifier collects the charge on a feedback capacitor to produce an output pulse whose voltage is proportional to the energy of the original X-ray.

This voltage pulse is processed by the back end electronics (BEE). The signal from the preamplifier has a low signal to noise ratio. The pulse shaping circuit amplifies and widens the pulse into a shape that approximates a Gaussian. The multichannel analyser measures the amplitude of each output pulse from the circuit and converts it into a digital signal which is binned into one of 4096 channels according to its amplitude. The amplitude of the pulse is directly proportional to the energy of the incident X-ray. As the fluorescent X-rays are detected, they are accumulated into a pulse height histogram over an integration time.

The Amptek Si-PiN diode (Redus et al., 2001) had a thickness of 300 μm and area of 7 mm^2 . The detector was housed inside a package with a 7.5 μm thick beryllium window and was hermetically sealed and filled with nitrogen at a pressure of 1 atm. The beryllium window had a transmission of 0.44 to Na K_{α} X-rays. The temperature of the diode was monitored using one Analog Devices* AD590 temperature sensor. The detector contained a thermoelectric cooler (TEC) that was used pre-flight to cool the detector for testing on the laboratory bench. The DHA electronics were on three printed circuit boards (PCBs). The top PCB housed the detector element and filtering components for the high voltage bias supply (100 V). The middle PCB contained the pre-amplifier that employed a reset method. A reset is required because charge accumulates on the capacitor and the output voltage rises with each detected photon. There is a limit to this voltage that is dependent upon the preamplifier supply voltage and so the capacitor was discharged periodically. The rear circuit PCB contained components to regulate the voltage supply for the pre-amplifier.

The Back End Electronics contained the pulse processing circuit. The peak height was captured by a peak-hold circuit and digitised by an analogue to digital converter (ADC). The data were binned to 12 bit resolution (~ 6.4 eV/bin). The BEE was powered to 6 V for normal operation. The BEE temperature was monitored using two AD590 temperature sensors, one on each side of the board.

* One Technology Way, P.O. Box 9106, Norwood, MA 02062-9106, U.S.A.

The XRS would have been subject to a challenging thermal environment on Mars, especially since the instrument was intended to operate during Martian night such that passive cooling of the Si-PiN diode could be employed. The operating temperature of the Si-PiN diode is between -20 °C and -60°C. Thermal modelling of the landing site (Sykes, 2003a) suggested that the DHA would have experienced temperatures of between -90°C and +5°C. However, the power dissipation from the heater layers in the DHA PCB would have kept the Si-PiN diode at a temperature of nominally -40°C for the majority of time for which the XRS was operating. The temperature inside the lander was modelled to vary between -60°C and 0°C but power dissipation from the electronics and heater layer would have prevented its temperature falling below -15°C.

It is of interest to compare the XRS to the Alpha Particle X-ray Spectrometer (APXS) for the Mars Exploration Rovers (described in Chapter 2) since they have closely related science objectives and functions (Table 3.2).

The Beagle 2 XRS is capable of excitation of trace elements such as Rb, Sr, Y and Zr because of the use of ¹⁰⁹Cd sources for primary excitation that emit Ag K X-rays. In contrast, the APXS ²⁴⁴Cm sources emit Pu L X-rays but the Compton and Rayleigh scattered Pu L_α X-rays overlap with Rb K_α and Sr K_α in APXS spectra (Rieder et al., 2003). In addition, in APXS spectra there is a Zr K line arising from fluorescence of the collimator on the detector which is an interference with Zr K fluorescent X-rays from the sample. However, the alpha mode of the APXS (that the XRS does not have) is capable of the detection of carbon, although there is interference with the CO₂ in the Martian atmosphere. The APXS has a superior resolution to the XRS which is of use to resolve peaks of major elements such as Na, Mg, Al and Si. The mass and size of the XRS are smaller than the APXS because these resources were severely constrained on Beagle 2.

The FM XRS was incorporated into the Beagle 2 payload and the flight spare XRS, a copy of the FM XRS, was characterised in the laboratory. The ambitious timescale for the build, qualification and delivery of the FM XRS meant that it was delivered with a basic level of calibration. The bulk of the calibration work was performed with the FS XRS and took place under vacuum in the calibration facility. The detailed calibration work with the FS could be applied to the FM since they were essentially identical. In addition, since both instruments analysed the same set of reference materials, the results could have been cross referenced. The Beagle 2 calibration target would have been used to check that the detection efficiency (discussed in Section 4.3) of the

instrument remained unchanged compared to before launch. Although the calibration of the FS XRS was originally intended to support the calibration of the FM XRS, after the failure of Beagle 2 the calibration work became focussed informing the design of future versions of the instrument.

Instrument	Beagle 2 XRS	MER APXS
Principle of analysis	X-ray fluorescence	X-ray fluorescence, Rutherford backscattering, Particle induced X-ray fluorescence
Elemental Range	Major, minor and trace elements including Rb, Sr, Y, Zr. Not carbon.	Major, minor and trace elements. Overlap of Pu L _α Compton and Rayleigh scatter peaks with Rb K _α and Sr K _α . Alpha mode capable of measuring carbon.
Radioisotope sources	⁵⁵ Fe (×2) ~60 MBq total and ¹⁰⁹ Cd (×2) ~5 MBq emit Mn K (5.90 and 6.49 keV) and Ag K (22.16 and 24.94 keV) and L X-rays	²⁴⁴ Cm (6) ~1.1 GBq emits Pu L X-rays (predominantly 14.28 and 18.28 keV) and alpha particles (~5.8 MeV)
Detector	Si-PiN diode 7 mm ² area	Silicon drift detector 10 mm ² area, alpha particle detectors
Resolution	~340 eV at 5.9 keV	~160 eV at 5.9 keV
Mass	58g (DHA) + 98g (BEE)	250g (sensor head) + 120g (electronics)
Dimensions	DHA: Cylindrical 47 mm diameter, 47 mm length BEE: 120 × 80 × 15 mm	Sensor head: Cylindrical 53 mm diameter, 90 mm length Electronics board: 170 × 100 × 10 mm
Power	~3 W	~0.3 W

Table 3.2 A comparison of the characteristics of the APXS with the XRS.

3.4 Calibration Facility

The calibration facility (Figure 3.5) for the XRS, developed at the University of Leicester Space Research Centre, is a vacuum chamber that is cylindrical in shape and 44 cm in length and 30 cm in diameter. The XRS DHA was mounted within the chamber and connected to the BEE on the bench via a feedthrough out of the rear flange. The chamber was connected to a scroll pump and evacuated to a pressure of ~1 mbar. A turbo pump then pumped the chamber down to pressures of typically $5 \cdot 10^{-7}$ mbar.

The DHA was attached to an L-plate that was in turn attached to a cold plate separated by a plastic insulator piece from a cold finger. The cold finger was cooled by liquid nitrogen (at temperatures of 63 – 77 K) which was contained in a reservoir above the chamber. Heaters in the cold plate controlled the temperature of the XRS such that the detector temperature was typically 250 K. The purpose of the insulator was to impede the thermal coupling of the cold finger to the cold plate. The temperatures of the DHA and BEE were monitored using the temperature sensors.

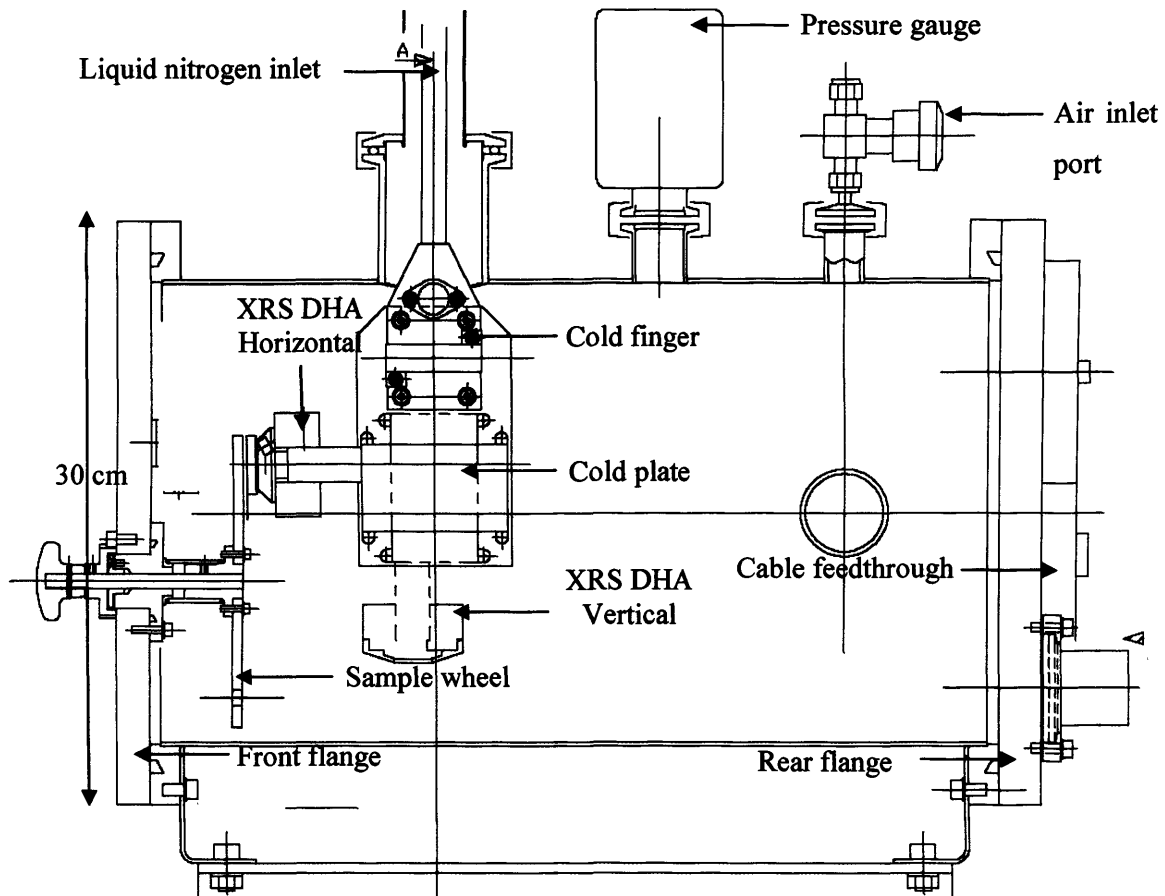


Figure 3.5 Schematic of the XRS calibration facility.

The DHA was positioned horizontally facing the sample wheel mounted on the inside of the front flange of the chamber. On the perimeter of the wheel were eight sample plates (Figure 3.6, top). The samples used to calibrate the XRS were either geological reference material (whose composition is known to a high degree of accuracy) consisting of a powder pellet or pure elemental samples. The sample wheel was manually rotated from outside the chamber such that each sample on the wheel was presented flush against the CFRP cap for analysis. An alternative configuration allowed the XRS to analyse samples, such as rock slabs, that were too big to be

mounted on the sample wheel (Figure 3.6, bottom). The XRS L-plate was positioned such that the DHA was pointing vertically downwards. The sample was mounted on a platform below the XRS with four screws, one in each corner. The screws were used to raise the platform such that the slab was flush against the CFRP cap. Once the DHA was under vacuum and cooled, the BEE was turned on. The BEE was connected to a PC data acquisition card and spectral acquisition software, developed in-house, was used to collect the data for a fixed integration time and display the spectrum.

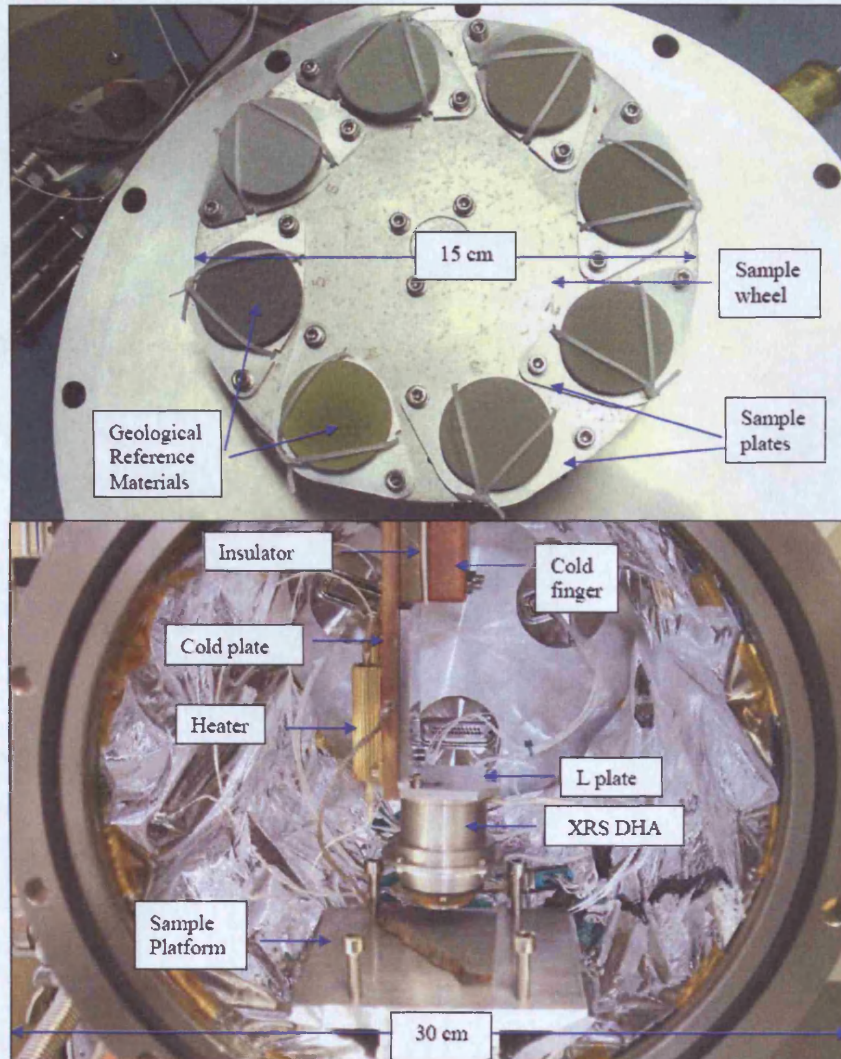


Figure 3.6 (Top) Geological reference materials used for the calibration of the XRS (listed in Chapter 5) in the form of pressed powder pellets mounted on the sample wheel which is in turn mounted on the front flange of the vacuum chamber. (Bottom) The XRS DHA in the calibration facility. The front flange on which the sample wheel is mounted is removed. The DHA is positioned vertically downwards to perform measurements of a rock slab on the platform.

3.5 Summary

This chapter has described the Beagle 2 lander mission, its science objectives and payload. A scientific objective of Beagle 2 was to perform a geological investigation of rocks at the landing area and the XRS was included in the payload to perform *in situ* geochemical analyses of Martian rocks and soils. The XRS, described in detail in this chapter, exhibited several unique design features. It was highly miniaturised to be accommodated on Beagle 2. It also employed dual source excitation (as opposed to sequential excitation) using ^{55}Fe and ^{109}Cd sources with the fluorescent X-rays detected by a Si-PiN diode. A comparison was made to the APXS which highlighted the extended trace element capability of the XRS (ie, Rb, Sr and Zr) compared to capability of the APXS to analyse C using the RBS technique. The development of this instrument required testing in the calibration facility, which has been described. The next four chapters will discuss the experimental work with the XRS starting with its experimental characterisation.

Chapter 4

Characterisation of the X-ray Spectrometer

This chapter describes the basic characterisation of the FS XRS, prior to its detailed calibration (Chapter 5). Basic characteristics such as gain, energy resolution and spectral artefacts present are described in detail. Measurements and modelling of system deadtime and quantum detection efficiency are presented. Finally, the gain variation of the XRS with temperature of its components is described.

4.1 Spectrum Gain and Energy Resolution

The raw data from a typical measurement by the XRS (the operation of which has been described in detail in Chapter 3) of the geochemical composition of a sample is a pulse height histogram. This X-ray spectrum consists of number of counts (on the y axis) versus channel number (on the x axis). It contains peaks which correspond to characteristic emission lines from X-ray fluorescence of elements in the sample; the energy of these lines can be used to identify the elements using Moseley's law (Moseley, 1913, 1914). Figure 4.1 is an X-ray spectrum of the geochemical reference material Whin Sill Dolerite (WS-E) from a 3 hour duration measurement.

The channel number is converted into X-ray energy (usually units of keV) primarily to perform a qualitative evaluation of the spectrum and identify the elements associated with characteristic lines but also ultimately for a quantitative analysis (Chapter 5). This is the process of energy (or gain) calibration which can be achieved using two or more reference peaks of a known energy. The Mn K and Ag K X-rays, emitted from the ^{55}Fe and ^{109}Cd sources respectively, are both Rayleigh and Compton backscattered from the sample and subsequently detected by the Si-PiN diode. Separate Ag K Compton and Rayleigh peaks are identifiable in the spectrum. In contrast, the spectrum appears to have solely Rayleigh scattered Mn K_{α} and K_{β} peaks since their energy difference to the less intense Compton scattered Mn K_{α} and K_{β} X-rays is smaller than is resolvable by the XRS (as discussed later in this Chapter). Rayleigh backscattered peaks are suitable reference lines since they are always present in spectra with an identifiable energy, regardless of the sample composition.

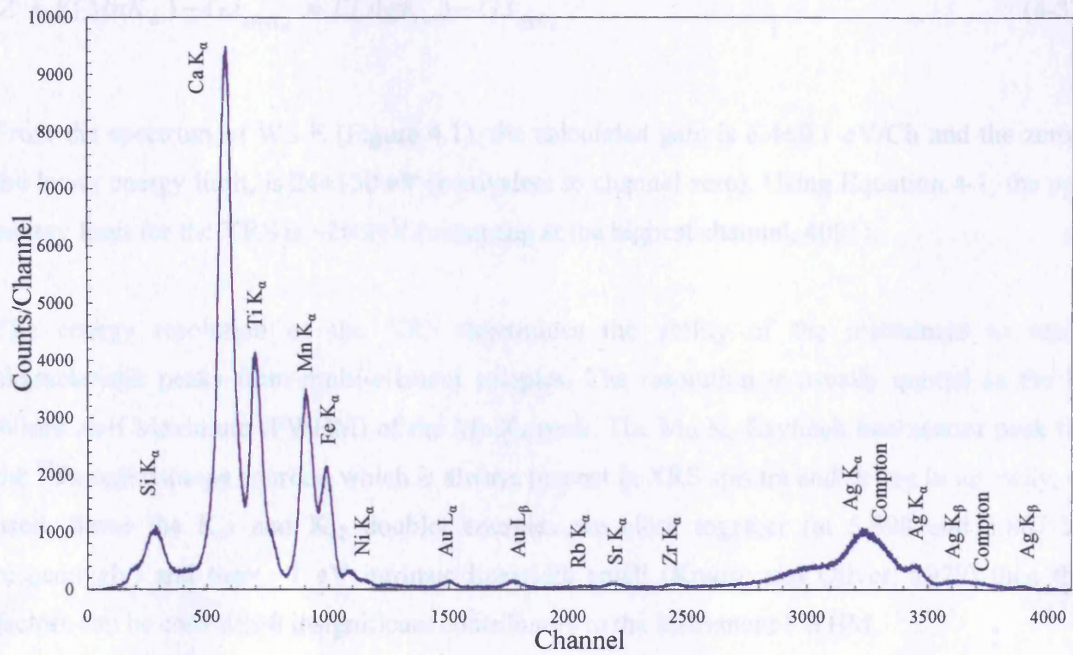


Figure 4.1 The raw pulse height histogram from the XRS measurement of WS-E. All the prominent K_{α} lines are labelled. Where the lines overlap, the most intense K_{α} line is labelled for clarity.

The relationship between the channel number, i , and the corresponding energy, E , is given by:

$$E(i) = G \cdot i + Z, \quad (4-1)$$

where G is the gain (keV/channel) and Z is the zero offset (keV) or the energy of channel zero.

If the Mn K_{α} and Ag K_{α} peaks are utilised for the energy calibration, then the gain is given by:

$$G = \frac{E(\text{Ag}K_{\alpha}) - E(\text{Mn}K_{\alpha})}{i_{\text{Ag}K_{\alpha}} - i_{\text{Mn}K_{\alpha}}}. \quad (4-2)$$

The zero offset, Z , is calculated by using either the Mn K_{α} or Ag K_{α} Rayleigh backscattered peaks, using the following expression:

$$Z = E(MnK_{\alpha}) - G.i_{MnK_{\alpha}} = E(AgK_{\alpha}) - G.i_{AgK_{\alpha}} \quad (4-3)$$

From the spectrum of WS-E (Figure 4.1), the calculated gain is 6.4 ± 0.1 eV/Ch and the zero, or the lower energy limit, is 24 ± 130 eV (equivalent to channel zero). Using Equation 4-1, the upper energy limit for the XRS is ~ 26 keV (occurring at the highest channel, 4096).

The energy resolution of the XRS determines the ability of the instrument to resolve characteristic peaks from multi-element samples. The resolution is usually quoted as the Full Width Half Maximum (FWHM) of the Mn K_{α} peak. The Mn K_{α} Rayleigh backscatter peak from the ^{55}Fe radioisotope sources, which is always present in XRS spectra and strong in intensity, was used. Since the $K_{\alpha 1}$ and $K_{\alpha 2}$ doublet energies are close together (at 5.898 and 5.887 keV respectively) and their ~ 1 eV intrinsic linewidth small (Krause and Oliver, 1979) then these factors can be considered insignificant contributors to the instrument FWHM.

The dominant factors that contribute to the FWHM in the case of the Si PiN diode (Knoll, 2000; Nicholson, 1974) are from noise introduced from (i) detector processes, (ii) electronic pulse processing and (iii) detector leakage currents. Since these factors are statistically independent of one another then they are added in quadrature to obtain the overall noise. The measured FWHM (in terms of energy eV) of an X-ray line, ΔE_{Total} , is given by:

$$\Delta E_{\text{Total}} = \sqrt{\Delta E_{\text{Det}}^2 + \Delta E_{\text{Leak}}^2 + \Delta E_{\text{Elec}}^2} \quad (4-4)$$

where ΔE_{Det}^2 is the contribution due to detector processes, ΔE_{Elec}^2 is the contribution due to the electronic pulse processing system and ΔE_{Leak}^2 is the contribution attributable to the detector leakage current. Each of these contributors is described in detail below.

The value of ΔE_{Det}^2 is governed by the statistics of the creation of electron-hole pairs in the diode for a given incident X-ray. This sets the ultimate limit to the energy resolution of the instrument since careful design can minimise the electronic contributors. The statistical variation of the number of electron hole pairs is lower than that predicted by Poisson statistics. This difference is due to secondary electron-hole pair generation not being independent and an empirical modifier to the Poisson value, called the Fano factor (Fano, 1947), is used. The standard deviation on the number of electron-hole pairs created is given by:

$$\sigma_N = \sqrt{FN} = \sqrt{\frac{FE}{\omega}}, \quad (4-5)$$

where F is the Fano factor for Si, ω is the average energy to create one electron-hole pair in Si and E is the X-ray energy (in eV).

The contribution to the FWHM from the detector resolution, ΔE_{Det}^2 , is obtained from multiplying Equation 4-5 by ω , to obtain units of energy (eV), and 2.35, to convert from standard deviation to FWHM, and is given by:

$$\Delta E_{Det} = 2.35\sqrt{F\omega E}. \quad (4-6)$$

The value for ω is taken to be ~ 3.68 eV (Fraser et al., 1994). The Fano factor is taken as ~ 0.16 for Si (Owens et al., 2002; Fraser et al., 1994). The values of ω and F are treated as constants for the characterisation of the Si-PiN diode. In fact, ω has a weak dependence on temperature and can vary from ~ 3.62 eV at room temperature to 3.70 eV near absolute zero (Bertolini and Coche, 1968). Theoretical work by Fraser et al. (1994), confirmed by experiment by Owens et al. (2002), has shown that the ionization energy and the Fano factor are both dependent upon the energy of the X-ray. Substituting these values for F and ω into Equation (4-6), the intrinsic detector resolution for Si at 5.90 keV is ~ 140 eV.

The second, and most dominant, contributor to the noise arises from pulse processing (amplification and shaping) of the pulse from the pre-amplifier to a level that matches the input range of voltages for the MCA. The input pulse before the MCA ideally has a voltage that is directly proportional to the energy of the X-ray. The electronic noise sources randomly alter this voltage amplitude to contribute to the overall system noise. These electronic noise sources (described in Nicholson, 1974) come from (i) pulse pileup, (ii) the ballistic deficit and (iii) random noise arising from Johnson (thermal) noise:

(i) Pulse pileup, originating from the overlap of two pulses that occur nearly simultaneously, becomes more dominant when the detector encounters a large flux of X-rays at the detector and hence large count rates. However, during the normal operation the XRS receives ~ 150 counts per

second during the analysis of silicate rocks then this contribution can be ignored.

(ii) The ballistic deficit is concerned with the shape of the voltage pulse from the pre-amplifier arising from the collection of charge from the detector after an X-ray event. This pulse shape (width and amplitude) depends on the charge collection time and the shaping time constant of the pre-amplifier. An infinitely large time constant means the amplitude of the voltage pulse is at its maximum. For a finite time constant, the amplitude of the voltage pulse is less than this maximum amplitude. The ballistic deficit is the difference in amplitude between the voltage pulse produced the infinite (ideal) and finite (real) time constants. However, the input current pulse shape from the detector varies due to statistical factors involving variations in the time to collect the charge because of charge trapping and recombination in the detector. Therefore the ballistic deficit is not constant but has a noise component associated with it and contributes to the electronic noise.

(iii) Johnson noise (Johnson, 1928) arises from the thermal motion of the charge carriers inside a conductor which alters the voltage in a conductor. The thermal noise power is dependent only on temperature and the Boltzman constant and is constant throughout the frequency spectrum (also described as white noise). This noise produces fluctuations superimposed on a given voltage signal thereby degrading its signal to noise. The most important source of noise is from components near the start of the signal processing chain since the signal strength is at its weakest relative to the noise. Noise generated at this point is amplified by the same level as the signal. Therefore, significant noise is introduced at the pre-amplifier stage, the majority of which arises from Johnson noise.

The final contributor to the noise arises from leakage current from the thermal generation of electron-hole pairs within the depleted region of the detector. This process is statistical meaning the leakage current has some variation. The Johnson noise from the pre-amplifier and the dark current from the detector is reduced by cooling these components to 250 K.

In summary, for a device like the Si PiN diode operating in the range 1-25 keV, the major contributor to the noise (Knoll, 2000; Hollstein, 1970) is from the electronic pulse processing, followed by the detector processes and finally the detector leakage currents. Out of the electronic noise sources the Johnson noise associated with the pulse processing components, in particular the pre-amplifier, is the dominant contributor.

An insignificant contributor to the noise arises from the multi channel analyser (MCA). The MCA converts an analogue voltage (that is proportional to the energy of the detected X-ray) at its input into a digital code (corresponding to one of 4096 channels) at its output. As the series of voltages are digitally converted they are binned into a pulse height histogram over an integration time to produce the resulting spectrum. Each output code produced corresponds to a finite range of voltages. However, a real MCA deviates from an ideal system because this input range of voltages varies according to the output code and this is referred to as differential nonlinearity. Channels that are too wide will collect more counts than those that are too narrow. The differential nonlinearity for the MCA employed by the XRS, expressed as the maximum percentage deviation of the ideal channel width to the real channel width, is typically less than 1%. Therefore, this is an insignificant contributor to the overall system noise compared to the other sources.

A spectrum of reference material GSP-1 composed of Granodiorite was acquired for an integration time of 3 hours. The Mn K_{α} and K_{β} and Fe K_{α} and K_{β} peaks were each modelled as a Gaussian function on a linear background (Figure 4.2). Their relative intensities were set as the fundamental ratio between K_{α} and K_{β} for each element (Thompson et al., 2001). A satisfactory fit for the Mn K_{α} line is a Gaussian with a FWHM value of ~ 390 eV. This means that, from Equation 4-4, the contribution from the processing electronics is ~ 370 eV. The resolution of the FM XRS was found using an identical method to be ~ 340 eV at Mn K_{α} .

This ~ 50 eV difference in the resolution of the FM and FS XRS arises from differences in the intrinsic Si-PiN detector resolution. In fact, the detector with the superior resolution was chosen for incorporation into the FM XRS. The resolution of a commercial Amptek X-ray Spectrometer that employs the same Si-PiN detector is quoted ~ 185 eV FWHM at Mn K_{α} (Redus et al., 2001). The limiting factor in the resolution of the FS and FM XRS compared to the Amptek XRS is the noise contribution from the different design of the (larger, more massive) pre-amplifier and amplifier electronics.

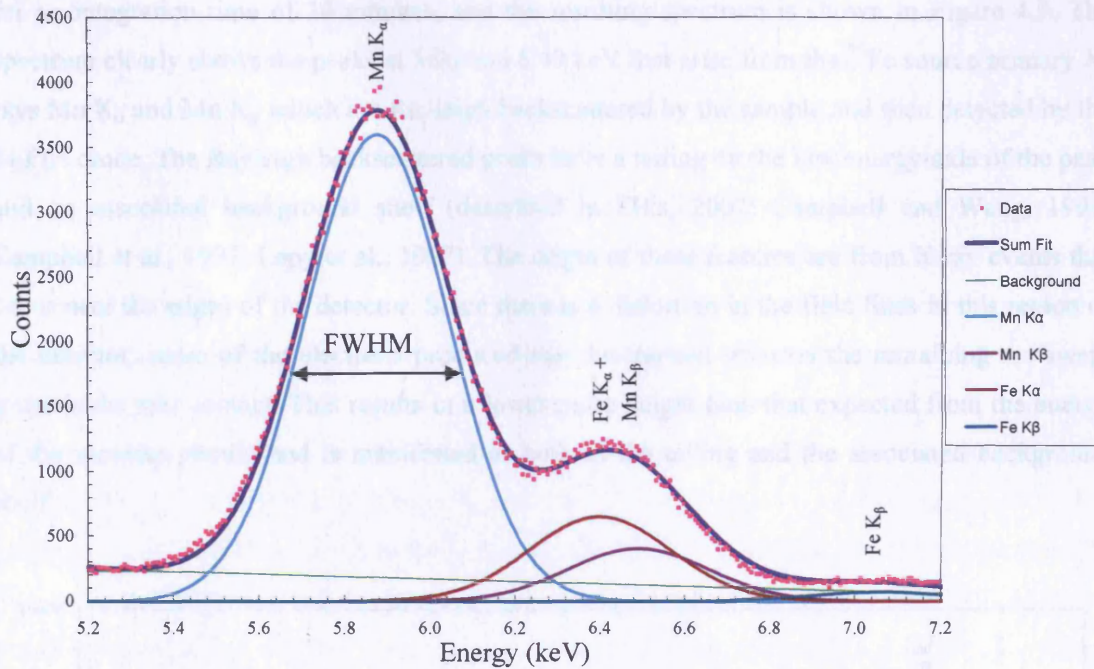


Figure 4.2 Plot of fit of Mn K_{α} and K_{β} and Fe K_{α} and K_{β} to WS-E spectrum. The pink dots are the measured spectrum. The blue line represents the fit and is the sum of four Gaussians, with a FWHM of ~ 390 eV, corresponding to Mn K_{α} and K_{β} and Fe K_{α} and K_{β} X-ray lines on a linear background (green line).

4.2 Spectrum Artefacts and Background

A typical spectrum contains not only characteristic X-ray fluorescence emission lines but also a number of different spectral artefacts that originate from the instrument, in addition to the Rayleigh and Compton backscattered lines from the radioisotope sources. Also, all the spectral peaks lie on a background which must be characterised.

To investigate the spectral artefacts and the background, a measurement of a rectangular block of PolyTetraFluoroEthylene (PTFE) of dimensions $30 \times 40 \times 15$ mm was performed. This low atomic number material was used so that the X-ray fluorescence lines from the sample were below the lower energy threshold of the XRS. Therefore, the spectrum should contain only peaks representing spectral artefacts superimposed on a background. The effect of excitation using the ^{55}Fe and ^{109}Cd sources on the spectrum was investigated by using each pair in succession for analysis of the plastic sample.

Firstly, the XRS analysed the plastic sample using only the ^{55}Fe sources for primary excitation

for an integration time of 30 minutes, and the resulting spectrum is shown in Figure 4.3. The spectrum clearly shows the peaks at 5.90 and 6.49 keV that arise from the ^{55}Fe source primary X-rays Mn K_{α} and Mn K_{β} which are Rayleigh backscattered by the sample and then detected by the Si-PiN diode. The Rayleigh backscattered peaks have a tailing on the low energy-side of the peak and an associated background shelf (described in Ellis, 2002; Campbell and Wang, 1991; Campbell et al., 1997; Lepy et al., 1997). The origin of these features are from X-ray events that occur near the edges of the detector. Since there is a distortion in the field lines in this region of the detector, some of the electrons produced may be trapped whereas the remaining are swept towards the rear contact. This results in a lower pulse height than that expected from the energy of the incident photon and is manifested as both as the tailing and the associated background shelf.

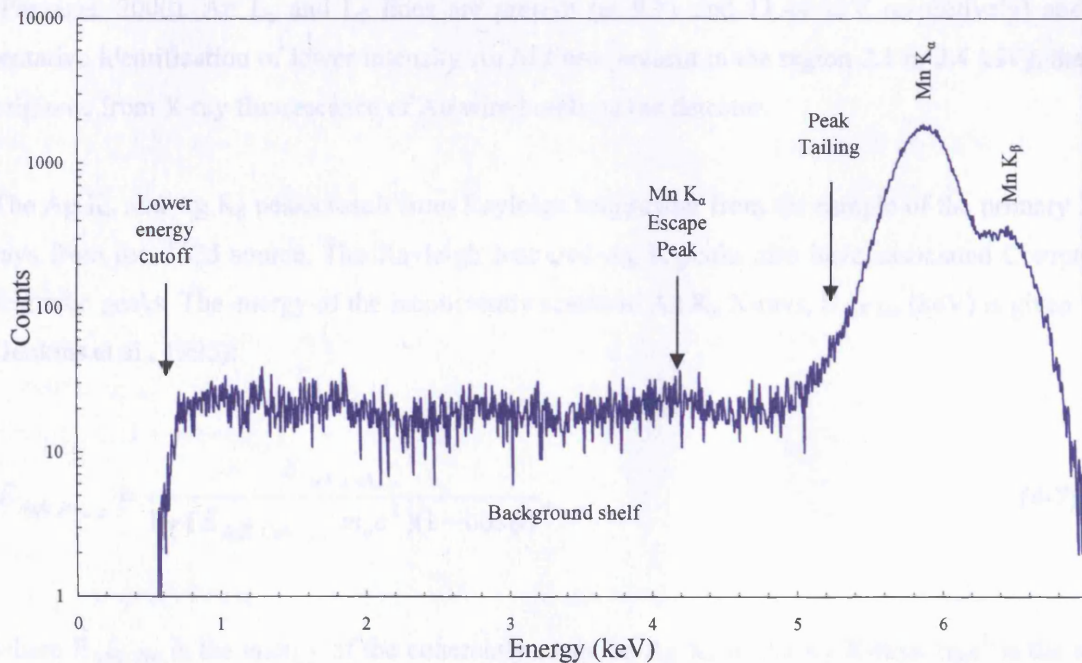


Figure 4.3 XRS spectrum of plastic sample using solely the ^{55}Fe sources for an integration time of 30 minutes. The Mn K_{α} and K_{β} X-rays originate from the ^{55}Fe sources. The Mn K_{α} peak has noticeable tailing on the low energy side and an associated background shelf and escape peak. The low energy cutoff for the spectrum at ~ 0.6 keV is shown.

The escape peak associated with Mn K_{α} is also present. For X-rays incident on the detector with energy higher than the Si K absorption edge, the detection process involves the generation of predominantly Si K_{α} fluorescent X-rays. Mostly these Si K X-rays are absorbed in the detector

material, resulting in a charge generated proportional to the energy of the incident X-ray, but occasionally the Si K_{α} X-rays will escape. The probability of escape is high if the X-ray is absorbed near to the front of the detector material. In the case when a Si K_{α} X-ray escapes, the energy detected will be 1.74 keV less than the energy of the original X-ray. Hence for Mn K_{α} , a peak is present in the spectrum at 4.2 keV (5.90 minus 1.74 keV). At energies of ~ 10 keV the intensity of the escape peak is small at $\sim 3\%$ that of the parent peak (Ellis, 2002). The lower energy cutoff at ~ 0.6 keV (\sim channel 65) is set by a low level discriminator that rejects pulses for digitisation that have a magnitude that is lower than some pre-defined channel.

Figure 4.4 shows the spectrum of the plastic sample excited by primary X-rays from the ^{109}Cd sources only. The spectrum contains peaks due to X-ray fluorescence of materials in the instrument. Ni K and lines are present and originate from Ni in the can that houses the detector (Pantazis, 2000). Au L_{α} and L_{β} lines are present (at 9.71 and 11.44 keV respectively) and a tentative identification of lower intensity Au M lines (present in the region 2.1 to 2.4 keV); these originate from X-ray fluorescence of Au wire bonds on the detector.

The Ag K_{α} and Ag K_{β} peaks result from Rayleigh backscatter from the sample of the primary X-rays from the ^{109}Cd source. The Rayleigh scattered Ag K peaks also have associated Compton scattered peaks. The energy of the incoherently scattered Ag K_{α} X-rays, $E_{\text{AgK,Inc}}$ (keV) is given by (Jenkins et al., 1995):

$$E_{\text{AgK,Inc}_{\alpha,\beta}} = \frac{E_{\text{AgK,Coh}_{\alpha,\beta}}}{1 + (E_{\text{AgK,Coh}_{\alpha,\beta}} / m_0 c^2)(1 - \cos \phi)}, \quad (4-7)$$

where $E_{\text{AgK,Coh}}$ is the energy of the coherently scattered Ag K_{α} or Ag K_{β} X-rays, $m_0 c^2$ is the rest mass of an electron (511 keV) and ϕ is the Compton scatter angle.

The Compton scatter angle (defined in Figure 4.5) is the sum of the incidence, θ_1 , and exit, θ_2 , angles:

$$\phi = \theta_1 + \theta_2. \quad (4-8)$$

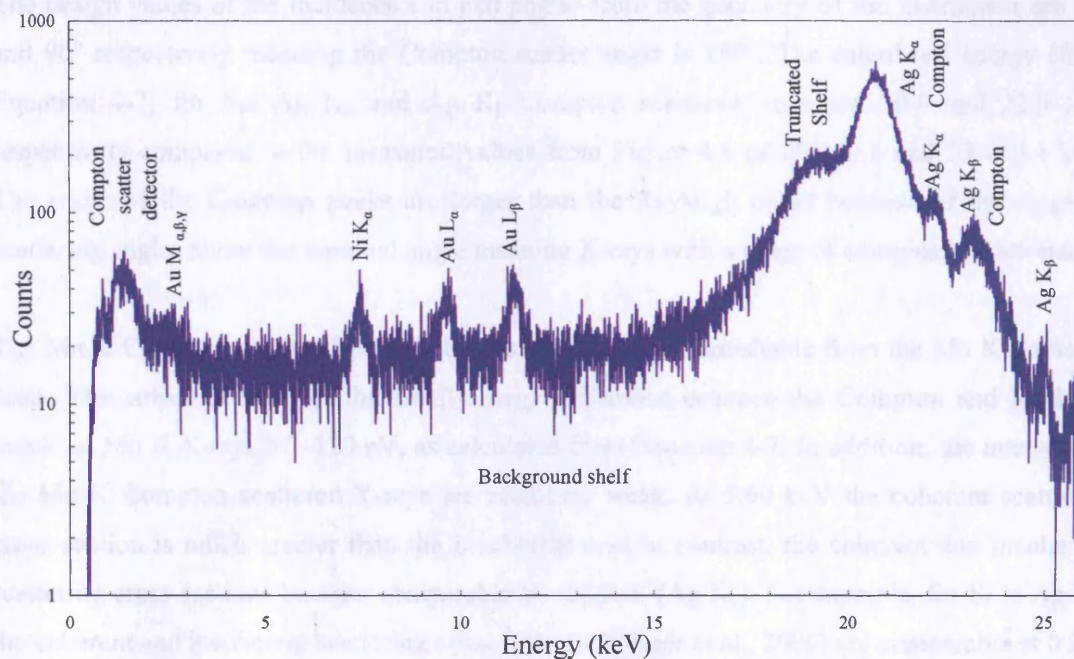


Figure 4.4 XRS spectrum of plastic sample using solely the ^{109}Cd sources for an integration time of 30 minutes. Ag K peaks associated with Compton and Rayleigh scatter of primary X-rays from the ^{109}Cd sources are present. The truncated shelf and background shelf associated with the Compton Ag K peak is from partial charge collection in the detector. The low energy peak at ~ 1.5 keV derives from X-rays incident on the Si-PiN diode and Compton scattering out of the sensitive detector volume without reabsorption, leaving a low energy electron. Ni K originates from Ni in the detector can and Au L from the Au wire bonds in the detector.

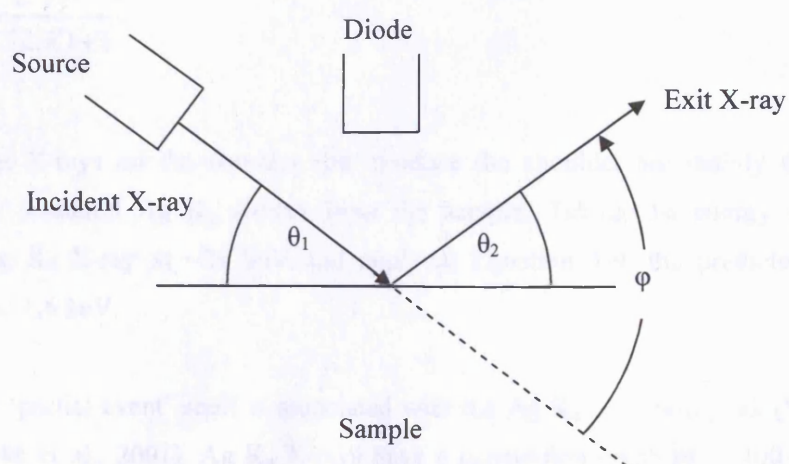


Figure 4.5 Diagram defining angle of incidence, exit and Compton scatter angle.

The design values of the incidence and exit angles from the geometry of the instrument are 60° and 90° respectively meaning the Compton scatter angle is 150°. The calculated energy (from Equation 4-7) for the Ag K_α and Ag K_β Compton scattered lines are 20.5 and 22.9 keV respectively compared to the measured values from Figure 4.4 of 20.7±0.3 and 23.2±0.4 keV. The width of the Compton peaks are larger than the Rayleigh peaks because of the range of scattering angles about the nominal angle meaning X-rays with a range of energies are detected.

The Mn K Compton scattered peak in Figure 4.3 is not distinguishable from the Mn K Rayleigh peak. This arises because of the small energy difference between the Compton and Rayleigh scattered Mn K X-rays of ~120 eV, as calculated from Equation 4-7. In addition, the intensity of the Mn K Compton scattered X-rays are relatively weak. At 5.90 keV the coherent scattering cross section is much greater than the incoherent one; in contrast, the coherent and incoherent scattering cross sections become comparable at ~22 keV (Ag K_α). For example, for Si at Ag K_α, the coherent and incoherent scattering cross sections (Berger et al., 2006) are comparable at 0.213 cm²/g and 0.141 cm²/g respectively. At Mn K_α the coherent cross section is ~13 times greater than the incoherent scattering cross section at 1.08 cm²/g and 0.081 cm²/g respectively.

The low energy ‘Compton shoulder’ at 1.4±0.2 keV (Figure 4.4) derives from X-rays incident on the Si-PiN diode and Compton scattering out of the sensitive detector volume without reabsorption, leaving a low energy electron. The energy at which the shoulder occurs, E_e, for a Compton scatter angle of 180°, is given by (Jenkins et al., 1995):

$$E_e = \frac{E}{(mc^2 / 2.E) + 1}. \quad (4-9)$$

The incident X-rays on the detector that produce the shoulder are mainly the coherent and incoherently scattered Ag K_α X-rays from the sample. Taking the energy of the Compton scattered Ag K_α X-ray at ~21 keV and applying Equation 4-9, the predicted energy of the shoulder is at 1.6 keV.

A truncated ‘partial event’ shelf is associated with the Ag K_α Compton peak (Van Gysel et al., 2003; Kalinka et al., 2001). Ag K_α X-rays have a penetration depth of ~1400 μm in Si (Potts, 1987) and so events can occur near the rear of the detector. The Si-PiN diode is partially depleted meaning the depletion region extends to ~200 μm out of a total wafer thickness of 300 μm. The

events that occur at the exit face of the detector (in the field free region) migrate more slowly than those in the depleted region. The electrons are more likely to be trapped or recombine and this results in partial charge collection. This produces a lower pulse height than expected and is manifested as the truncated shelf in the spectrum.

Figure 4.6 shows the spectrum from a measurement of the plastic sample using simultaneous excitation with both ^{55}Fe and ^{109}Cd sources in the CFRP structure for a total integration time of 30 minutes. The features in the previous spectra (Figures 4.3, 4.4) are combined in this spectrum. The shelf on the low energy side of the Mn K lines rises because these peaks are superimposed on the shelf from the Ag K lines. A typical spectrum of a rock sample contains the spectral artefacts from the instrument along with the characteristic X-ray emission lines from elements within the rock.

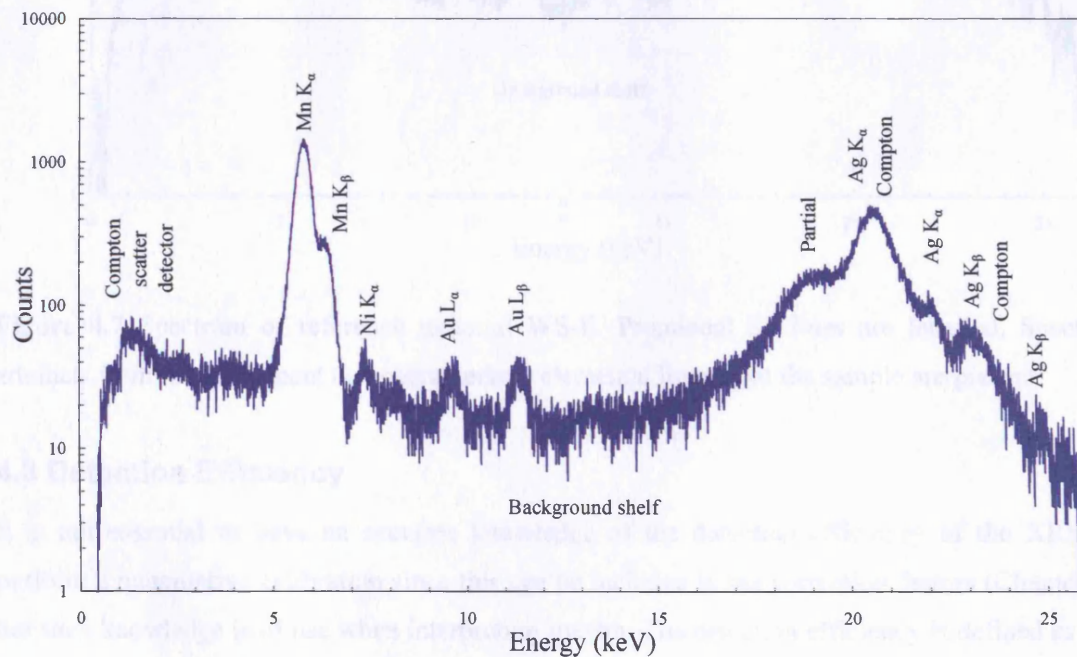


Figure 4.6 XRS spectrum of plastic using both ^{55}Fe and ^{109}Cd sources.

Figure 4.7 is a spectrum of reference material WS-E for a 3 hour integration time. The major elements, represented by characteristic lines Si K, Ca K, Ti K and Fe K, are present and correspond to concentrations of typically 1-10s of % level in the sample (Govindaraju et al., 1994). The Si K peak overlaps with those of Mg K, Al K and P K lines. Trace elements are represented in the spectrum with characteristic lines Rb K, Sr K and Zr K and have typical

concentrations of 10-100s ppm (Govindaraju et al., 1994). The Rayleigh scattered $Mn K_{\beta}$ peak overlaps with $Fe K_{\alpha}$ (Fe is present in the sample) and the Compton and Rayleigh scattered $Ag K_{\alpha}$ and $Ag K_{\beta}$ lines are clearly present. All of the peaks are superimposed on the general 'shelf structure' background.

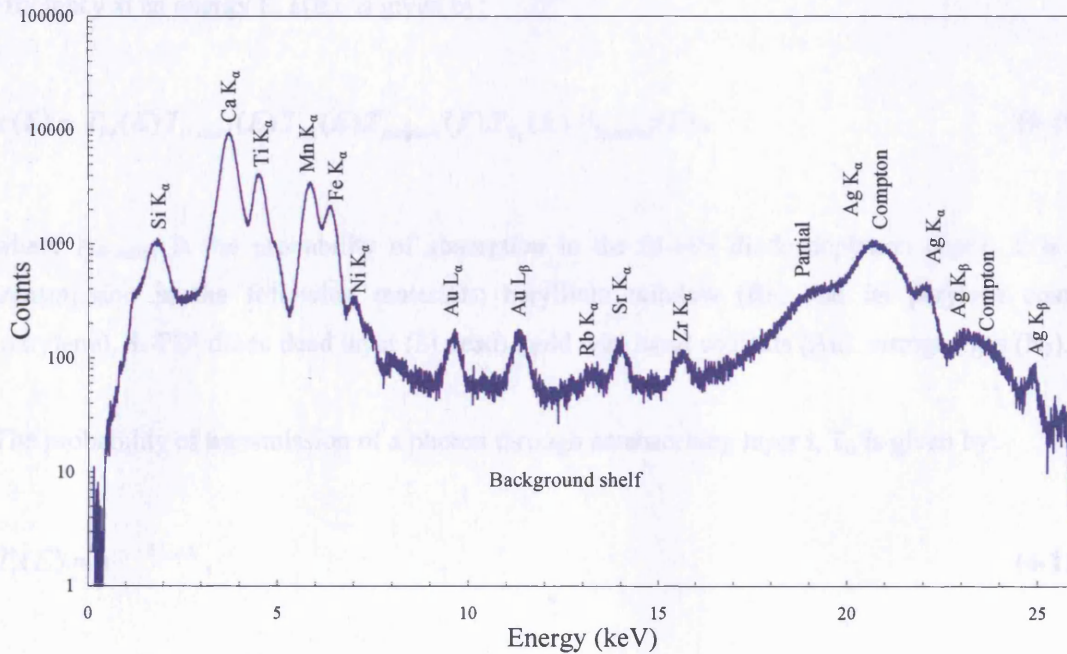


Figure 4.7 Spectrum of reference material WS-E. Prominent K_{α} lines are labelled. Spectral artefacts from the instrument and characteristic elemental lines from the sample are present.

4.3 Detection Efficiency

It is not essential to have an accurate knowledge of the detection efficiency of the XRS to perform a quantitative calibration since this can be included in the correction factors (Chapter 5) but such knowledge is of use when interpreting spectra. The detection efficiency is defined as the fraction of incident photons incident on the detector at a given energy E that are absorbed in the detector active volume and give rise to a detectable pulse. Incident photons are absorbed in the layers of material in advance of the depleted region of the detector. The absorbing layers and their thicknesses (Pantazis, 2000) for the XRS are:

- Beryllium window on the detector can ($7.5 \mu\text{m}$)
- Coating of parylene on the Beryllium window ($3 \mu\text{m}$)
- Nitrogen gas at 1 atm in the hermetically sealed detector can (1.5 mm path length)

- Gold wire bond contacts on the Si-PiN diode (70 nm)
- Silicon dead layer on the front face of the Si-PiN diode (100 nm)

In order to be detected, the photon must be absorbed in the Si-PiN diode which has a depleted region thickness of 200 μm of a total thickness of 300 μm (Pantazis, 2000). The detection efficiency at an energy E , $\varepsilon(E)$, is given by:

$$\varepsilon(E) = T_{Be}(E) \cdot T_{Si.dead}(E) \cdot T_{Au}(E) \cdot T_{parlyene}(E) \cdot T_{N_2}(E) \cdot A_{Si.active}(E), \quad (4-10)$$

where $A_{Si.active}$ is the probability of absorption in the Si-PiN diode depletion depth; T is the transmission in the following materials: beryllium window (Be) and its parlyene coating (parlyene), Si-PiN diode dead layer (Si dead), gold wire bond contacts (Au), nitrogen gas (N_2).

The probability of transmission of a photon through an absorbing layer i , T_i , is given by:

$$T_i(E) = e^{-\mu(E)_i \rho t_i}, \quad (4-11)$$

where $\mu(E)$ is the mass absorption coefficient (Berger et al., 2006) at energy E (cm^2/g), ρ is the density of the material (g/cm^3) and t is the thickness of the layer (cm).

The probability of photoelectric absorption within the Si sensitive volume, $A_{Si.active}$, is given by:

$$A_{Si.active}(E) = 1 - T_{Si.active}(E) = 1 - e^{-\tau(E)\rho t}, \quad (4-12)$$

where $\tau(E)$ is the photoelectric mass absorption coefficient at energy E (Berger et al. 2006).

The components of the detection efficiency were modelled, as shown in Figure 4.8. The transmission through the beryllium window has a strong effect on the detection efficiency at low energies (< 3 keV) but the transmission of the gold contacts, parlyene and nitrogen are also major contributors. At the higher energies (> 5 keV) the efficiency is dominated by absorption in the Si depletion depth. The only absorption edges to occur are from the Si dead layer and Au wire bonds. Si has a K edge that occurs at 1.839 keV; Au has two principal M edges at 2.206 and

2.291 keV and between these energies there is a large change in the mass absorption coefficient which increases from 919 to 2360 cm²/g. In addition, there are three smaller M edges at 2.743, 3.148 and 3.525 keV that are not associated with such a large change in the mass absorption coefficient. The impact of the edges on the overall detector efficiency is that it sharply falls at 2.206 keV because of the transition in the mass absorption coefficient between the Au M_I and Au M_{II} edges. Also, there are two small steps in detection efficiency at 2.743 keV, associated with the Au M_{III} edge, and at 1.839 keV associated with an edge in the transmission of the Si dead layer.

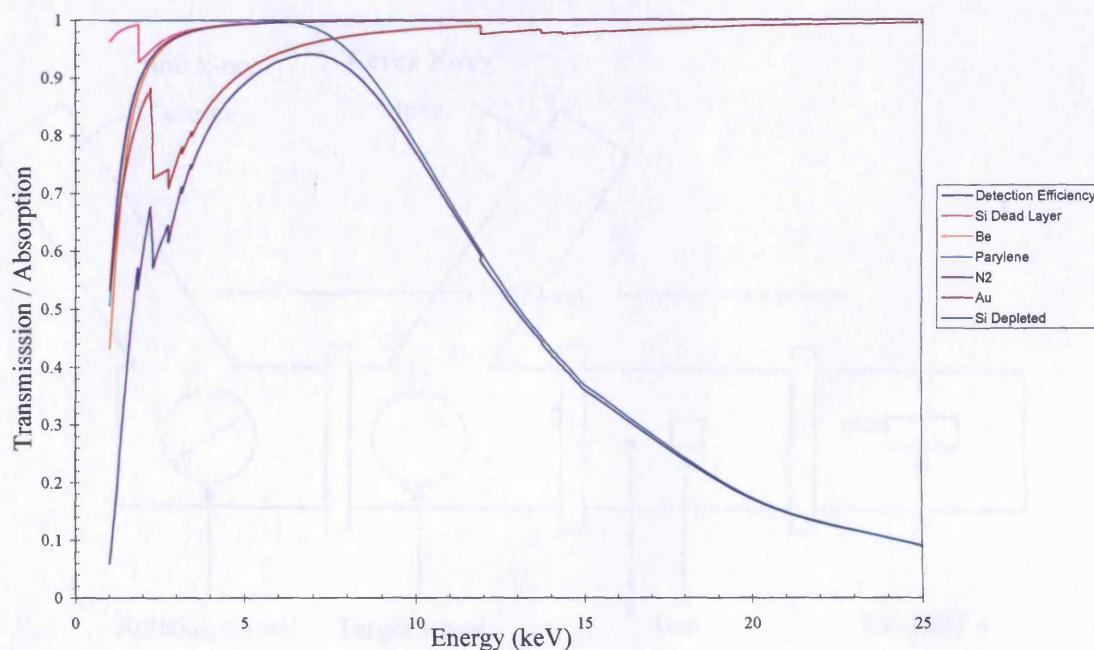


Figure 4.8 Plot of energy dependence of the components of the Si-PiN diode quantum efficiency. The overall detection efficiency (dark blue curve), the product of these contributing factors, is also shown.

Measurements of the detection efficiency were made by Butcher (2003) in the Space Research Centre JET-X Test Facility (Fletcher-Holmes, 2000) a schematic of which is shown in Figure 4.9. The Si-PiN detector was part of a commercial Amptek XR-100T X-ray spectrometer system (Redus et al., 2001). It consisted of two parts: the XR-100T module, which comprises the detector, cooling system and preamplifier, and a type PX2T power supply and amplifier. The XR-100T was operated inside a vacuum chamber at a pressure of 10⁻⁷ mbar. The chamber was mounted at the end of the detector test facility beamline. Two X-ray sources were employed: (i) a

commercial ‘Kevex’* electron bombardment X-ray tube that was used to induce fluorescence from various target materials mounted on a target wheel and (ii) a soft X-ray source, developed in-house (Pearson, 1984), which employed a heated cathode to emit electrons that were incident on a coated anode to induce X-ray fluorescence from the elements in the coating. The X-rays from the soft X-ray source were polychromatic and a crystal grating that was able to rotate was used to provide monochromatic X-rays. A gas proportional counter (GPC) whose quantum efficiency was calculable to a high degree of accuracy (Fletcher-Holmes, 2000) was used to measure the reference count rate from the sources. It was able to be inserted into the path of the beamline for measurements.

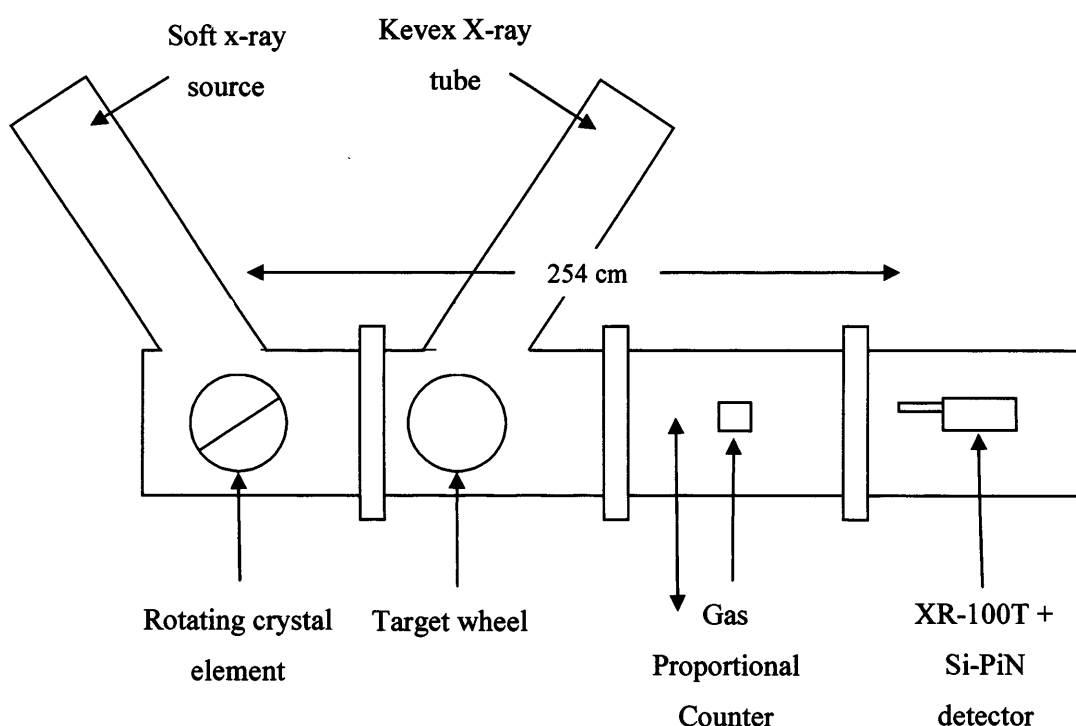


Figure 4.9 Schematic of the JET-X Test Facility used for the measurements of the quantum efficiency of the Si-PiN diode. The Gas Proportional Counter (GPC) could be moved in or out of the beamline.

Measurements at Mg K, Al K, Si K, Cl K, Ti K, Fe K and Cu K energies were made using both a Gas Proportional Counter and the XR-100T in the beamline. The XRS detection efficiency is given by:

* Kevex X-ray Inc., 320 El Pueblo Road, Scotts Valley, CA 95066, USA.

$$\varepsilon(E) = \frac{N_{XRS}}{N_{GPC}} \cdot \varepsilon_{GPC}(E) \cdot G, \quad (4-13)$$

where N_{XRS} and N_{GPC} are the number of counts in the FWHM of the peak of energy E for the XRS and GPC respectively, ε_{GPC} is the quantum efficiency of the GPC and G is a geometric factor incorporating differences in the distance from the sources for the GPC and XRS and differences in the detector areas for the two instruments. The results are shown in Figure 4.10.

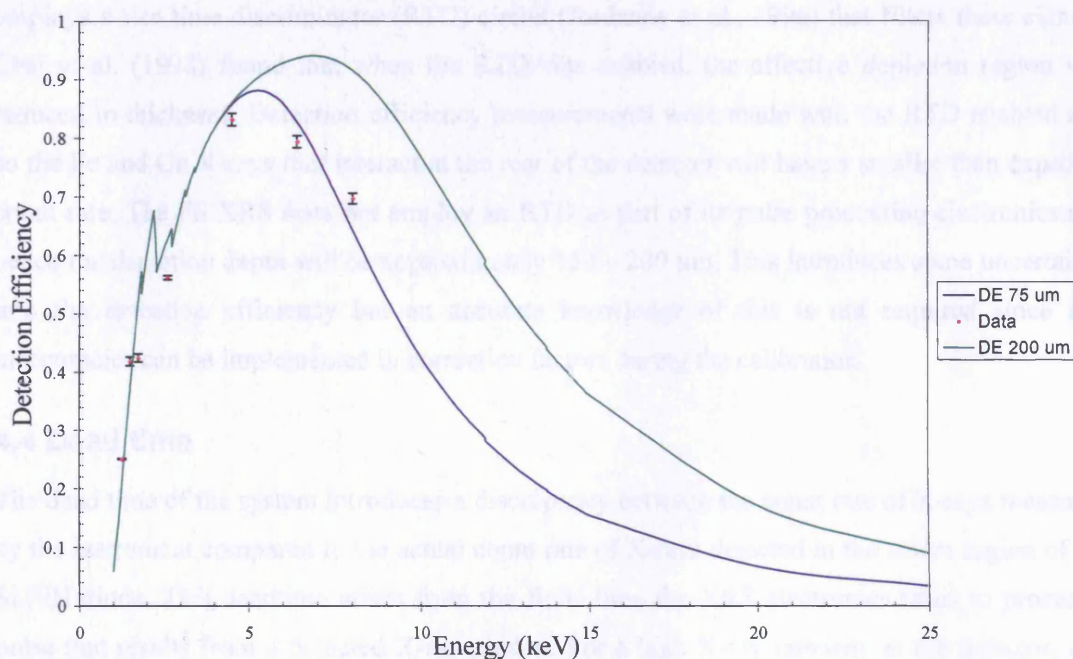


Figure 4.10 Measurements of the XRS detector detection efficiency compared to the modelled detection efficiency (DE). The blue curve corresponds to the best fit depletion depth at 75 μm and the green curve corresponds to the expected depletion depth (Pantazis, 2000) at 200 μm .

The data agrees with the modelled detection efficiency at the energies below 5 keV which means that the composition and thicknesses of the absorbing layers are correct. For higher energies where the detection efficiency is limited by the depletion depth, the best fit for the data corresponds to a depletion depth of 75 μm whereas the expected depletion depth (Pantazis, 2000) is $\sim 200 \mu\text{m}$.

The disagreement between the data and the expected detection efficiency arises from the fact that the effective depletion depth is actually of order 75 μm . The Ti, Fe and Cu K X-rays interact with the detector near its rear, owing to their large critical penetration depth (the thickness of silicon at which 99% of the incident X-rays are absorbed). For example, Fe has a critical penetration depth of 170 μm in Si (Potts, 1987). The partially depleted Si-PiN diode has a ~ 200 μm depletion region out of a wafer thickness of 300 μm . Several authors have found experimentally that the 300 μm thickness Si-PiN diodes (of 7 mm^2 area) are partially depleted with depletion depths at 147 μm (Wegrzynek et al., 2003a), 209 μm and 145 μm (Szaloki et al., 2001). Absorption events that occur near the rear 100 μm of the detector are collected more slowly than normal events and a smaller amount of charge collected than expected from the energy of the X-ray. The PX2T employs a rise time discriminator (RTD) circuit (Jordanov et al., 1996) that filters these signals. Ebel et al. (1998) found that when the RTD was enabled, the effective depletion region was reduced in thickness. Detection efficiency measurements were made with the RTD enabled and so the Fe and Cu X-rays that interact at the rear of the detector will have a smaller than expected count rate. The FS XRS does not employ an RTD as part of its pulse processing electronics and hence the depletion depth will be approximately 150 – 200 μm . This introduces some uncertainty into the detection efficiency but an accurate knowledge of this is not required since any inaccuracies can be implemented in correction factors during the calibration.

4.4 Dead time

The dead time of the system introduces a discrepancy between the count rate of X-rays measured by the instrument compared to the actual count rate of X-rays detected in the active region of the Si-PiN diode. This deadtime arises from the finite time the XRS electronics takes to process a pulse that results from a detected X-ray photon. For a high X-ray intensity at the detector, it is possible for a pulse to be produced while the previous pulse from an earlier X-ray detection event is being processed. In this case, the new pulse is ignored. This introduces a systematic error between the input count rate (the rate at which X-rays are detected) and the output count rate (the count rate measured by the XRS as a system). For a given total integration (or real) time, T , the dead time, T_D , is the amount of time for which the XRS is not acquiring data. The real time is given by:

$$T = T_L + T_D, \quad (4-14)$$

where T_L is the live time, the time for which the XRS is acquiring data.

The main electronic contributors to the XRS deadtime, in order of severity, arise from (i) the time for the MCA to read data into the PC, (ii) the BEE pulse processing time and (iii) the reset time of the detector pre-amplifier. Measurements of the XRS deadtime was performed by using a function generator to inject voltage pulses into the XRS electronics, bypassing the Si-PiN detector and preamplifier (part of the DHA) in the pulse processing chain. The pulse was similar to that generated by the DHA with a length of 100 μ s and amplitude of 10 mV. The pulses were generated at various frequencies ranging from 100 to 1500 Hz. Measurements of the output count rate were performed by recording a spectrum for a 2 minute integration time.

After initial measurements, it was found that the limiting factor on the deadtime was the Multichannel Analyser (MCA). The MCA read in 1000 events, for a live time t_l , and then read this data into a PC for a deadtime t_d , 0.7 s, during which time it acquired no further data. The deadtime introduced as a result of the MCA can be derived. The time to acquire 1000 events is the live time, t_l , and is given by:

$$t_l = \frac{1000}{I_i}, \quad (4-15)$$

where I_i is the input count rate.

This is followed by a period of dead time, $t_d = 0.7$ s.

The total dead time T_D for a given total real measurement time T is given by:

$$T_D = t_d \cdot \frac{T}{t_l + t_d} = \frac{0.7T}{\frac{1000}{I_i} + 0.7}. \quad (4-16)$$

The measured intensity, I_m , is given by:

$$I_m = I_i \cdot \frac{T_L}{T}. \quad (4-17)$$

Substituting for the live time T_L from Equation 4-14 and subsequently for the deadtime T_D from Equation 4-16 into Equation 4-17 results in the relationship between I_m and I_i in the case where the deadtime is limited by the MCA:

$$I_m = \frac{I_i}{1 + 7 \times 10^{-4} I_i}. \quad (4-18)$$

Equation (4-18) was plotted in Figure 4.11 (brown curve) and compared to the data (purple stars). Both the data and the model apply to the case where the MCA deadtime is limiting.

To eliminate the effect of the MCA deadtime, its operation was adjusted such that all of the data was stored during data acquisition and not uploaded to the computer. In the case of the Beagle 2 FM XRS this source of deadtime would not be present because it was designed to store the data as a histogram and then later upload via an uplink to Mars Express and then back to Earth.

The next limiting source of deadtime arises from the time for the BEE to process a pulse (eg, from the analogue to digital conversion time and the amplifier pulse processing time). Again, pulses similar to that generated by the DHA were injected into the BEE and the deadtime was measured using an oscilloscope to be $t_d = 220 \mu\text{s}$. For high input count rates, say 1500 Hz, if the pulses were regular, then the system never encounters deadtime since the time between pulses (at $\sim 670 \mu\text{s}$) is longer than $220 \mu\text{s}$. However, if the pulses are randomised then there is a finite chance of receiving a pulse during the deadtime period that is subsequently ignored. The generation of fluorescence X-ray photons occur as random events and obey the laws of Poisson statistics. Assuming that the deadtime is non-extending (meaning any pulses received within the deadtime interval are ignored), then the relationship between the input and the output count rate is given by the following expression (Jenkins et al., 1995):

$$I_m = \frac{I_t}{1 + t_d I_t} = \frac{I_t}{1 + 2.2 \times 10^{-4} I_t}. \quad (4-19)$$

This relationship is plotted in Figure 4.11 (purple curve).

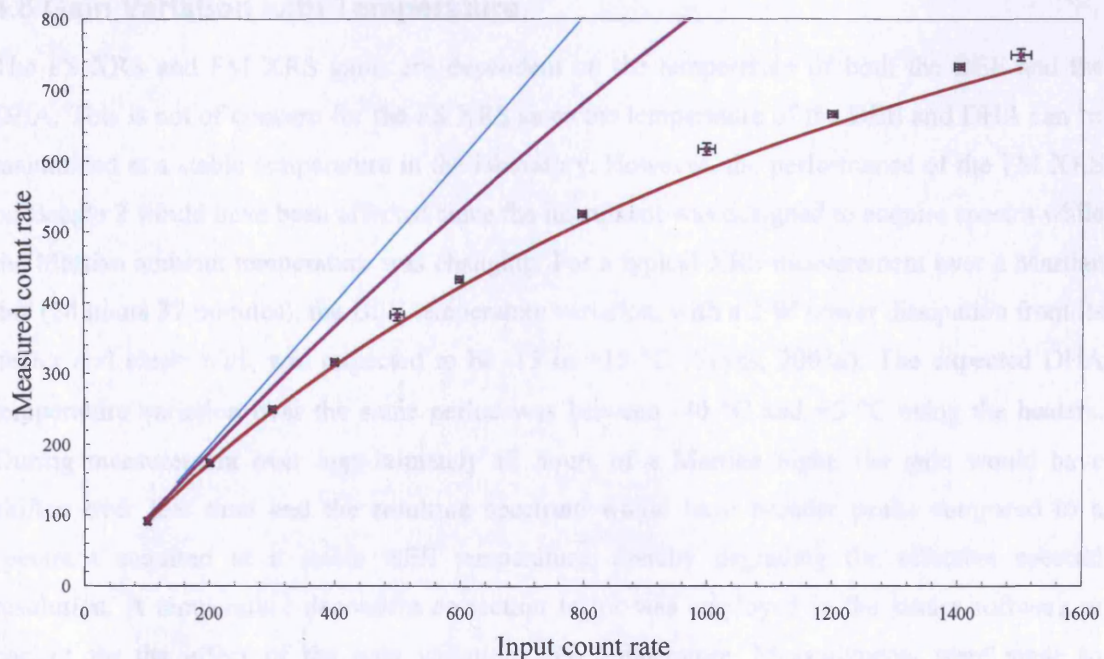


Figure 4.11 Plot of measured count rate versus the input count rate. The modelled throughput curves apply for the case where MCA deadtime is limiting (brown curve), the pulse processing is limiting (purple curve) and the one-to-one relationship where there is no deadtime (blue line). Measurements of the count rate for a given input count rate in the case where the deadtime is limited by the MCA are shown (purple stars).

The final source of deadtime occurs from the reset time of the detector pre-amplifier. The pre-amp is of a charge sensitive design and requires periodic resets to prevent detector leakage currents (and X-ray event generated charge) forcing the output into saturation. The reset period was measured to be 6.8 ms at a rate of typically every 480 ms, depending upon the detector temperature. This is equivalent to a deadtime of 1.4%.

In summary, the major contributor to the deadtime (the MCA) was eliminated. For normal operation, the count rates encountered for measurements of silicate rocks were ~150 counts per second, low enough for the deadtime to be ignored. For some measurements of pure element samples during the calibration of the XRS, the count rates were high enough to warrant a correction using Equation 4-19. For example, the detected flux of Vanadium fluorescence X-rays is ~400 counts per second and the percentage difference between the input and measured count rate is 9%.

4.5 Gain Variation with Temperature

The FS XRS and FM XRS gains are dependent on the temperature of both the BEE and the DHA. This is not of concern for the FS XRS since the temperature of the BEE and DHA can be maintained at a stable temperature in the laboratory. However, the performance of the FM XRS on Beagle 2 would have been affected since the instrument was designed to acquire spectra while the Martian ambient temperature was changing. For a typical XRS measurement over a Martian day (24 hours 37 minutes), the BEE temperature variation, with a 2 W power dissipation from its heater and electronics, was expected to be -15 to +15 °C (Sykes, 2003a). The expected DHA temperature variation over the same period was between -40 °C and +5 °C using the heaters. During measurement over approximately 12 hours of a Martian night, the gain would have shifted over that time and the resulting spectrum would have broader peaks compared to a spectrum acquired at a stable BEE temperature, thereby degrading the effective spectral resolution. A temperature dependent correction factor was employed in the lander software to correct for the effect of the gain variation with temperature. Measurements were made to characterise this gain variation with temperature using both the FS XRS and FM XRS.

The temperature of the electronic components in the DHA was measured by use of the temperature sensor mounted next to the Si-PiN diode. The temperature of the BEE was measured using the pair of temperature sensors mounted to the Printed Circuit Board (PCB) on opposite sides designated MT25 as the primary sensor and MT23 as the backup. The temperature as measured by MT25 and MT23 differs by a few degrees when the BEE was powered because of the temperature gradients present in the PCB. The temperatures quoted below were from the primary sensor M25.

Measurements of gain variation with temperature for the FM XRS were taken in a thermal vacuum chamber at Birmingham University, Department of Physics and Astronomy (Butcher, 2003). In order to vary the temperature of the DHA and BEE independently, they were both installed inside the chamber under vacuum at 10^{-7} mbar and mounted to separate plates for cooling. The DHA was attached to a cold finger cooled by liquid nitrogen via a plate that had resistive heaters to control the temperature upwards from -196 °C. The BEE stood on a table through which coolant (called Galden, a type of perfluoropolyether^{*}) flowed and which was

* Manufactured by Kurt J. Lesker Company (Kurt J. Lesker Company, PO Box 951677, Cleveland, OH 44193).

thermally coupled to it via four leg supports. The BEE was radiatively isolated from the chamber by wrapping it in a thermal blanket and the only thermal transfer was conductive loss through the legs. The BEE was cooled to various steady state temperatures between $-10\text{ }^{\circ}\text{C}$ and $+50\text{ }^{\circ}\text{C}$ and the DHA steady state temperature was varied between $-20\text{ }^{\circ}\text{C}$ and $-60\text{ }^{\circ}\text{C}$. The FM XRS performed measurements of a “mixed metal” sample consisting of a flat mosaic of Al, Mo, Ti and Cu foils for integration times of 10 minutes per spectrum. The gain values were calculated using the Ti K_{α} , Mn K_{α} , Cu K_{α} and Mo K_{α} lines as calibration peaks. The results are plotted in Figure 4.12; there are a total of 5 curves, each one corresponding to steady state DHA temperatures of $-20\text{ }^{\circ}\text{C}$, $-30\text{ }^{\circ}\text{C}$, $-40\text{ }^{\circ}\text{C}$, $-50\text{ }^{\circ}\text{C}$ and $-60\text{ }^{\circ}\text{C}$.

Figure 4.12 shows that the gain variation of the FM XRS is dominated by the BEE temperature and not by that of the DHA. For a fixed BEE temperature ($+24\text{ }^{\circ}\text{C}$), the gain is $\sim 7\text{ eV/channel}$, and has a maximum variation of 1.2 % when the DHA temperature is decreased from $-20\text{ }^{\circ}\text{C}$ to $-60\text{ }^{\circ}\text{C}$. In contrast, the gain is 6.33 eV/Ch at a BEE temperature of $+50\text{ }^{\circ}\text{C}$ (for DHA temperature of $-20\text{ }^{\circ}\text{C}$) and this increases by 20 % when the BEE temperature is reduced to $-10\text{ }^{\circ}\text{C}$.

The powered BEE under thermal vacuum conditions could only be cooled to a steady state temperature of $-10\text{ }^{\circ}\text{C}$ owing to poor thermal coupling to the cold plate at a temperature of $-75\text{ }^{\circ}\text{C}$. To take measurements below this temperature, the BEE was not powered, and allowed to cool to a steady state temperature of $-58\text{ }^{\circ}\text{C}$. The BEE was then switched on and, as its temperature rose dynamically because of power dissipation in the electronics, measurements of gain were taken by acquiring consecutive 2 minute spectra. The first measurement corresponded to the lowest starting BEE temperature at $-38\text{ }^{\circ}\text{C}$. The final measurement of gain, at a temperature of $-12.5\text{ }^{\circ}\text{C}$, was when the BEE had reached thermal equilibrium and so this data is equivalent to a measurement of the gain of the XRS when the BEE is at a stable temperature. However, this temperature is an average of the temperatures at the beginning and end of the two minute spectrum and so does not correspond to the lowest steady state temperature at $-10\text{ }^{\circ}\text{C}$. The measurements of the gain variation of the FM XRS with BEE temperature for the steady state (blue squares) and dynamic (blue stars) cases are shown in Figure 4.13.

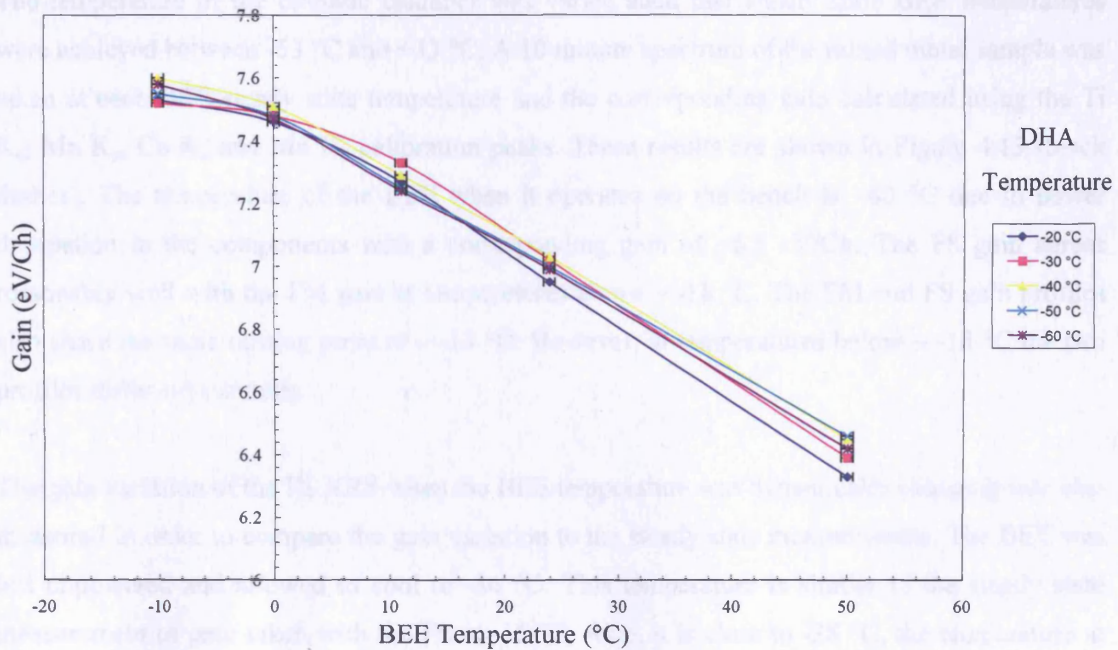


Figure 4.12 The gain variation of the FM XRS with steady state temperature of the BEE and DHA. Each curve corresponds to a different fixed DHA temperature while the BEE temperature is varied between temperatures of -10°C and $+50^{\circ}\text{C}$. The BEE temperature is an average of the five BEE temperatures corresponding to the five measurements of gain at each DHA temperature.

Repeat measurements of the gain variation with temperature were taken with the FS XRS. This was in order to verify the measurements of gain taken using the FM and reproduce measurements below a BEE temperature of -10°C but with the temperature in steady state and not dynamically changing. Convective cooling was employed with the aim of attaining a steady state temperature of the BEE at -50°C .

The experimental arrangement consisted of a non-evacuated climatic chamber, in which the XRS BEE was housed. To prevent the formation of ice on the BEE when the chamber was cooled, it was placed inside an antistatic bag inflated by a flow of dry nitrogen through it. To assist cooling of the gas, it flowed through a copper coil housed inside the chamber before it entered the bag. The DHA was housed inside the calibration facility (described in section 3.4) and cooled to a constant temperature of $-40 \pm 1^{\circ}\text{C}$. This is identical to the temperature of the DHA for the same measurements taken with the FM.

The temperature of the climatic chamber was varied such that steady state BEE temperatures were achieved between -53 °C and +33 °C. A 10 minute spectrum of the mixed metal sample was taken at each BEE steady state temperature and the corresponding gain calculated using the Ti K_{α} , Mn K_{α} , Cu K_{α} and Mo K_{α} calibration peaks. These results are shown in Figure 4.13 (black dashes). The temperature of the BEE when it operates on the bench is ~40 °C due to power dissipation in the components with a corresponding gain of ~6.5 eV/Ch. The FS gain agrees reasonably well with the FM gain at temperatures above ~ -18 °C. The FM and FS gain profiles also share the same turning point at ~ -13 °C. However, at temperatures below ~ -18 °C the two profiles differ substantially.

The gain variation of the FS XRS when the BEE temperature was dynamically changing was also measured in order to compare the gain variation to the steady state measurements. The BEE was left unpowered and allowed to cool to -34 °C. This temperature is similar to the steady state measurement of gain taken with the FS at -36 °C. Also, it is close to -38 °C, the temperature at which the gain of the FM XRS was measured when its BEE temperature was dynamically changing. The BEE was then powered and consecutive 1 minute spectra were taken. The results are shown in Figure 4.13 (black stars).

The FS gain variation when the BEE temperature is changing dynamically is reasonably small compared to those measurements taken when the BEE temperature is in steady state (comparing the black stars with the black dashes in Figure 4.13). The effect of measuring gain when the BEE temperature is dynamically changing is to flatten the gain variation profile compared to the steady state measurements. The profile of the gain variation of the FS when the BEE temperature is dynamically changing (black stars) is similar to the profile of the similar FM measurements (blue stars).

The reason for the flattening of the gain variation lies with the poor thermal coupling between the components in the BEE responsible for the gain variation and the pair of temperature sensors. When the BEE is powered on at a cold temperature, heat is dissipated through the gain critical components and they heat up at a faster rate than the temperature sensors that are mounted to the PCB. Hence, the gain of the XRS is constant because the gain critical components have quickly attained a steady state temperature. However, since the PCB temperature is still increasing, the temperature measured by the sensors is also increasing and so the profile is flattened. Eventually the temperature of the PCB stabilises and achieves thermal equilibrium with the gain critical

components. In conclusion, the measurements of the gain when the FM and FS temperature was dynamically changing showed that there was a fixed time after the BEE is switched on before the temperature sensors and gain critical components reach thermal equilibrium. However, a correction cannot be derived using these measurements since on Mars the ambient temperature will be changing sufficiently slowly such that all components on the BEE are in thermal equilibrium at any one time.

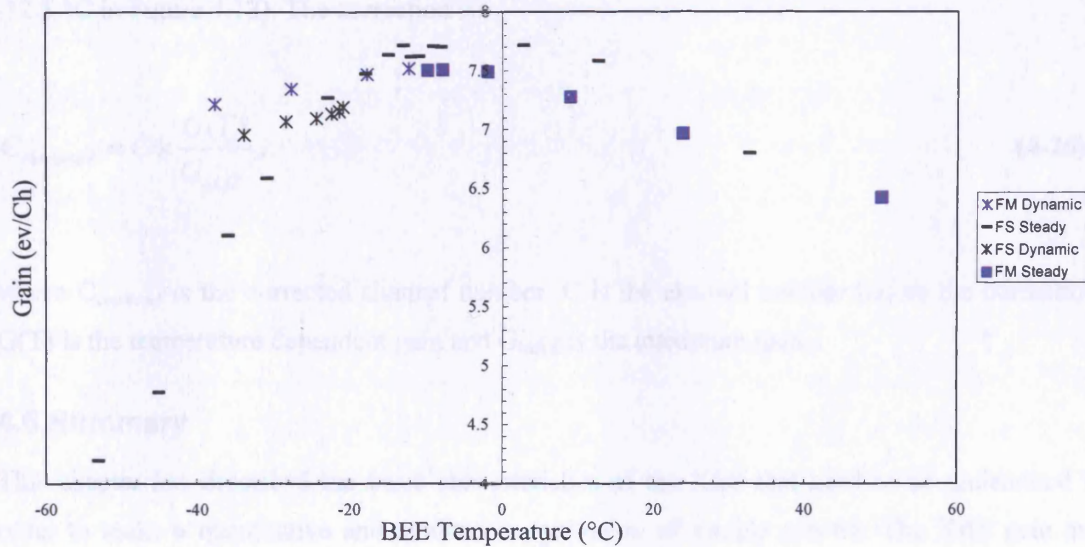


Figure 4.13 The gain variation of the FM and FS XRS with BEE temperature. For each XRS, measurements were made with the BEE at steady state temperature for the FS (black dashes) and the FM (blue squares). In addition measurements were made with the BEE temperature dynamically changing for the FS (black diamonds) and FM (blue diamonds). For clarity error bars (± 0.5 °C for all measurements) are not present on the data points.

Thermal modelling of Beagle 2 on the Martian surface (Sykes, 2003a) predicted that the FM BEE temperature variation over a measurement period would have been -15 °C to $+15$ °C with a 2 W heat dissipation in the BEE. Any gain correction would have been derived from an interpolation of the data from a combination of the gain profiles of the FM and FS XRS. There were direct measurements of the FM steady state gain measurements at temperatures above -10 °C. However, this temperature is not low enough to provide data to -15 °C. To extend the data to a lower temperature, the FM gain measurement where the BEE temperature was dynamically changing (blue stars) were interpolated to -18 °C which is the temperature at which this profile intersects the FS profile where the BEE is at a steady state temperature (black dashes).

During a measurement by the XRS, each voltage pulse that was digitised into a channel number was multiplied by a correction factor by the lander software before it was added to the pulse height histogram. The correction was dependent upon the temperature of the primary temperature sensor in the BEE. These temperature dependent correction factors were derived from an interpolation of the normalised gain data in Figure 4.13. After the correction is applied, the resulting pulse height histogram has a gain equivalent to the maximum gain (7.5 eV/Ch at -12.5 °C in Figure 4.13). The correction is:

$$C_{corrected} = C \times \frac{G(T)}{G_{MAX}}, \quad (4-20)$$

where $C_{corrected}$ is the corrected channel number, C is the channel number before the correction, $G(T)$ is the temperature dependent gain and G_{MAX} is the maximum gain.

4.6 Summary

This chapter has described the basic characteristics of the XRS that need to be understood in order to make a quantitative and qualitative evaluation of sample spectra. The XRS gain and energy resolution were measured. The origins of spectral artefacts were identified in order to distinguish between characteristic X-rays from the sample and those from the instrument. The detection efficiency of the instrument was modelled and measured. The deadtime of the system was determined and the major initial contributor eliminated. This enabled the input count rate to be accurately measured by the XRS necessary for quantitative calibration. Finally, the gain variation of the XRS with temperature of the DHA and BEE was investigated. This does not impact upon the calibration of the FS XRS since the temperature of the BEE and DHA were stable in the laboratory.

Chapter 5

Calibration of the X-ray Spectrometer

This chapter describes the calibration of the XRS which enables the instrument to convert the raw X-ray pulse height distribution from the measurement of a geological sample of unknown composition into elemental concentrations. The fitting of spectral peaks and background to derive X-ray fluorescence intensities of characteristic lines is described. This chapter outlines the theoretical basis of the quantitative calibration technique employed, which is based on the Backscatter Fundamental Parameter method, and the experimental steps taken to calibrate the XRS. The results from a compositional analysis of reference materials are presented.

5.1 Introduction

The calibration the Beagle 2 XRS enables the instrument to perform a geochemical analysis of a sample of unknown composition. Similarly, the previous X-ray Spectrometers successfully deployed on Mars have been calibrated, aspects of which are described in Gellert et al. (2006) and Rieder et al. (2003) for the MER APXS, Foley et al. (2003a) for the Pathfinder APXS and Clark et al. (1977), Clark and Baird (1973) and Toulmin et al. (1973) for the Viking XRFS. The calibration of the XRS allows its raw data, a pulse height distribution, to be converted into elemental concentrations with known uncertainties. This analysis consists of several parts. The first part is an energy calibration followed by a qualitative evaluation of the spectrum to identify characteristic X-ray lines from elements in the sample (described in Chapter 4). The second part consists of peak fitting of these characteristic lines to derive background subtracted areas and corresponding intensities. The third part is the conversion of these intensities into concentrations using an algorithm based on the Fundamental Parameter method (Wegrzynek et al., 2003a, 2003b).

5.2 Analysis of Reference Materials

The calibration of the XRS is based upon its measurements of geochemical reference materials (listed in Table 5.1). These are rocks and soils that are ground into a fine powder (of particle size ~ 10 s of μm) and $\sim 10\text{g}$ is mixed with a small amount of binder (eg, polyvinylpyrrolidone-methyl cellulose) and pressed into a disc-shaped powder pellet of diameter 30 mm and thickness 5 mm (Potts, 1987). Geochemical reference materials are used for calibration because their elemental composition is known to a high degree of accuracy. Reference materials are international standards and defined by the International Organisation for Standardisation (ISO, 1992) as, “a

material or substance one or more of whose property values are sufficiently homogeneous and well established to be used for the calibration of an apparatus, the assessment of a measurement method, or for assigning values to materials”.

In the context of the XRS calibration, the property values are the concentrations of elements in the reference material. An accurate knowledge of the composition of the reference materials is required for quantitative calibration in order to establish the relationship between the elemental X-ray fluorescence intensities as measured by the XRS and corresponding concentrations.

XRS measurements of the reference materials were performed using the experimental setup described in Chapter 3. The integration time for each measurement was 3 hours to achieve appreciable counts in the spectrum. Typically, the measured count rate was ~ 150 counts s^{-1} , meaning deadtime losses were negligible.

The reference materials are in an ideal format for the calibration of the XRS. They are homogenous since the rocks samples they are composed of are ground into a fine powder and compressed into pellets. The dimensions of the pellets are also suitable for analysis. Their diameter is greater than the diameter of the analysis footprint of the XRS (25 mm). Also, their thickness (at 5 mm) is greater than the critical penetration depth (the depth at which 99% of the incident X-ray intensity is attenuated) of the X-rays from the radioisotope sources in silicate rocks. For example, the Ag K_{α} X-rays from the ^{109}Cd sources have a critical penetration depth 2.8 mm into rhyolite, 2.1 mm into andesite and 1.6 mm into basalt (Potts et al., 1997a).

Reference Material	Rock Type	Supplier	Reference
AC-E*	Granite	CRPG	Govindaraju, 1995
AGV-1	Andesite	USGS	Govindaraju et al., 1994
BCR-1	Basalt	USGS	Gladney et. al., 1990
BHVO-1	Hawaiian Basalt	USGS	Gladney and Roelandts, 1988
G-2	Granite	USGS	Gladney et. al., 1992
G-94	Threlkeld microgranite	IAG	Thompson et al., 1996
GH*	Granite	CRPG	Govindaraju, 1995
GSP-1	Granodiorite	USGS	Gladney et al., 1992
GXR-2*	Park City, Utah soil	USGS	Gladney and Roelandts, 1990
Mars-1B	Basalt, Mauna Kea	JSC	Allen et al., 1998
Mica-Fe	Biotite	CRPG	Govindaraju, 1995
OU-1	Bardon Volcanic Tuff	IAG	Thompson et al., 1998
OU-2	Belford dolerite	IAG	Thompson et al., 2000
OU-3	Nanhoron microgranite	IAG	Potts et al., 2000
PCC-1	Periodotite	USGS	Gladney et al., 1991
PM-S	Microgabbro	CRPG	Govindaraju et al., 1994
QLO-1	Quartz Latite	USGS	Gladney and Roelandts, 1988
RGM-1*	Rhyolite	USGS	Gladney and Roelandts, 1988
SDO-1	Devonian Ohio Shale	USGS	Kane et al., 1990
SRM 2709	San Joaquin soil	NIST	NIST, 2003
SRM 2710	Montana soil	NIST	NIST, 2003
SRM 2711	Montana soil	NIST	NIST, 2003
STM-1	Nepheline Syenite	USGS	Gladney and Roelandts, 1988
WS-E	Dolerite	CRPG	Govindaraju et al., 1994

Table 5.1: Reference materials used for the calibration of the XRS with rock type, supplier and reference for accepted geochemical composition. The full names for the suppliers are as follows: Centre de Recherches Petrographiques et Geochimiques, France (CRPG); Johnson Space Centre, NASA, USA (JSC); National Institute of Standards and Technology, USA (NIST); International Association of Geoanalysts (IAG); US Geological Survey, USA (USGS). The reference materials labelled (*) were not analysed by the XRS but were amongst those analysed by two X-ray spectrometers described in Chapter 6.

5.3 Qualitative Analysis and Spectral Fitting

Each spectrum of a reference material (for example the spectrum of WS-E shown in Figure 5.1) contains a set of peaks, some originating from X-ray fluorescence of the constituent elements in the sample while others are spectral artefacts from the instrument (Chapter 4). These peaks are superimposed on a general background continuum. The nett peak area for each line l of a constituent element x in the sample must be established for quantitative calibration; this involves fitting the background continuum and constituent peaks. Spectral fitting was performed using AXIL (Analysis of X-ray spectra by Iterative Least-squares fitting), an algorithm developed by Van Espen et al. (1987). AXIL is part of the Quantitative X-ray Analysis System software developed by the International Atomic Energy Authority (IAEA, 1996).

The first stage of analysis of the spectrum consists of an energy calibration that allows a qualitative evaluation of the spectrum. As described in Chapter 4, the Mn K_{α} and Ag K_{α} peaks were used to perform an initial gain calibration using Equations 4-2 and 4-3. The energy resolution was determined using the FWHM of the Mn K_{α} peak (Figure 4.2).

The spectrum is split into three parts for fitting corresponding to (i) the major elements, (ii) the trace elements and (iii) the Ag K Rayleigh and Compton scatter peak region. A region of interest used to define each part, as shown in Figure 5.1. The regions of interest are:

- Major region ($E < \sim 8.5$ keV)
- Trace region (8.5 keV $\sim < E < \sim 17$ keV)
- Scatter region ($E > \sim 17$ keV)

For each region, least squares fitting of an analytical function to the data is performed. The analytical function is optimised using the following expression, which is the weighted sum of squares of the differences between the model, $y(i)$, and the measured spectrum y_i for a region of interest (Van Espen, 2002):

$$\chi^2 = \sum_{i=n_1}^{n_2} \frac{1}{\sigma_i^2} [y_i - y(i, a_1, \dots, a_m)]^2, \quad (5-1)$$

where σ_i^2 is the variance of counts in channel i ($\sigma_i^2 = y_i$, according to Poisson statistics), n_1 and n_2 are the lower and upper channel limits of the region of interest and a_1 to a_m are the parameters of

the model. The optimised values of the parameters occur when χ^2 is minimised which can be established by setting the partial derivatives of χ^2 with respect to the parameters to zero:

$$\frac{\partial \chi^2}{\partial a_j} = 0, \quad j = 1, \dots, m. \quad (5-2)$$

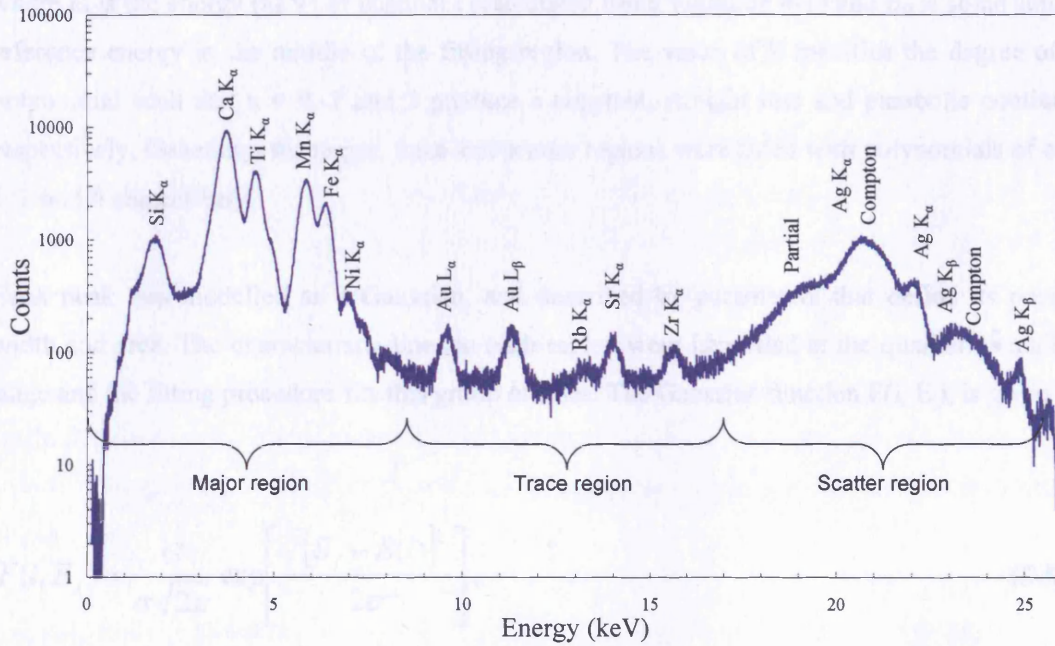


Figure 5.1 Energy calibrated spectrum of reference material WS-E (Dolerite) showing the regions of interest.

The analytical function, $y(i)$, used to describe both the background continuum and the characteristic lines in the spectrum is given by:

$$y(i) = y_B(i) + \sum_P y_P(i), \quad (5-3)$$

where $y_B(i)$ describes the background and $\sum y_P(i)$ describes all the peaks.

As discussed in Chapter 4, the main contributor to the background continuum is from incomplete

charge collection of intense lines in the spectrum but the complexity of a physical model of the continuum means that a mathematical function is used instead (Van Espen, 2002). The background function is described by a polynomial:

$$y_B(i) = a_0 + a_1(E_i - E_0) + a_2(E_i - E_0)^2 + \dots + a_k(E_i - E_0)^k, \quad (5-4)$$

where E_i is the energy (keV) of channel i (calculated using Equation 4-1) and E_0 is some suitable reference energy in the middle of the fitting region. The value of k specifies the degree of the polynomial such that $k = 0, 1$ and 2 produce a constant, straight line and parabolic continuum respectively. Generally, the major, trace and scatter regions were fitted with polynomials of order 1, 2 and 0 respectively.

Each peak was modelled as a Gaussian, and described by parameters that define its position width and area. The characteristic lines in each region were identified at the qualitative analysis stage and the fitting procedure fits this group of lines. The Gaussian function $F(i, E_j)$, is given by:

$$F(i, E_j) = \frac{G}{\sigma\sqrt{2\pi}} \exp\left[-\frac{[E_j - E(i)]^2}{2\sigma^2}\right], \quad (5-5)$$

where E_j is the energy of the X-ray line, $E(i)$ is the energy at channel i (Equation 4-1), G is the gain (eV/channel) and σ is the standard deviation of the peak (eV). The term $G/\sqrt{2\pi}$ is to normalise the Gaussian such that the sum over all channels is unity.

The standard deviation of the peak, σ , is given by (from Equations 4-4, 4-5 and 4-6):

$$\sigma^2 = \left(\frac{\Delta E_{Elec}}{2.35}\right)^2 + F\omega E_j. \quad (5-6)$$

The spectral parameters gain (G), zero (Z) and peak standard deviation (σ) are optimised during the least squares fitting. The group of lines from a single element x are modelled together where:

$$y_p(i) = A \sum_{j=1}^{N_p} R_j F(i, E_j), \quad (5-7)$$

where there are N_p lines in the group, A is the total number of counts for all the lines, F are the Gaussians for the various lines for the element (eg, K line group including the doublets $K_{\alpha 1}$ and $K_{\alpha 2}$) at energy E_j and R_j is the relative transition probabilities for the lines (corrected for detection efficiency).

Spectral peaks have a shape that deviates from a Gaussian shape (Ellis, 2002) since these peaks have an associated low energy tail and background shelf, as shown with the Mn K peaks in the ^{55}Fe spectrum (Figure 4.3), originating from incomplete charge collection from the detector. This shape is more strongly exhibited by strong peaks (those with a significant number of counts) since they have sufficient numbers of counts for this peak shape to be evident. AXIL employs data of experimentally derived values representing the differences between the observed shape and a pure Gaussian. The intensity of characteristic lines in the spectrum, derived from the least squared fitting, was corrected for the intensity of corresponding lines in the background spectrum (Figure 4.6).

Initially, analysis of spectra of 10 reference materials was performed. The materials were AGV-1, BCR-1, GSP-1, G-2, PCC-1, QLO-1, STM-1, Mica-Fe, PM-S and WS-E. Each spectrum was fitted for the major, minor and trace elements commonly found in silicate rocks. Figure 5.2 is a plot of the area of the K_{α} peak of the characteristic line versus concentration for major element Ca and trace element Zr.

To a first approximation, the fluoresced X-ray intensity of a characteristic line is proportional to the elemental concentration. Figure 5.2 shows a clear linear relationship between the peak area and the certified concentration for major element Ca and trace element Zr. However, each best fit line exhibits a non-zero intercept. The expected result is that for zero concentration of an element present then there are zero fluorescent counts. The non-zero intercept arises from an over or under estimation of the background at the fitting stage. In the case of Zr, the number of counts in the peak is comparable to the background area and so the intercept is more sensitive to modelling of the background. The background below the elemental peak is systematically over-estimated, thereby resulting in a consistent under-estimation of the peak area.

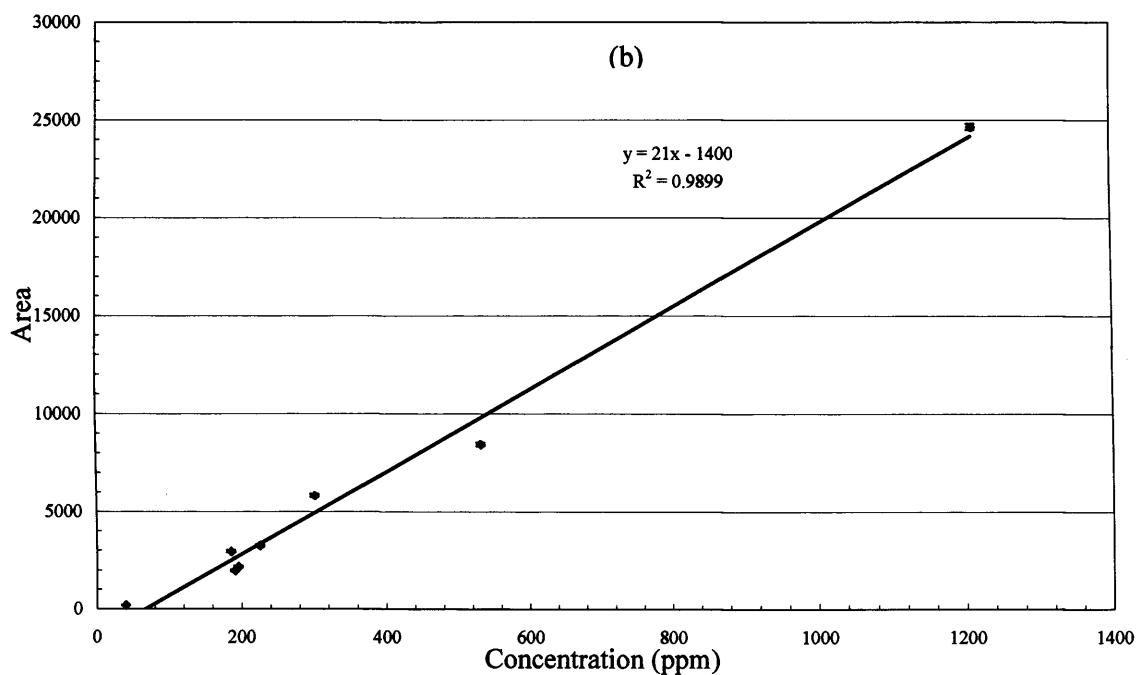
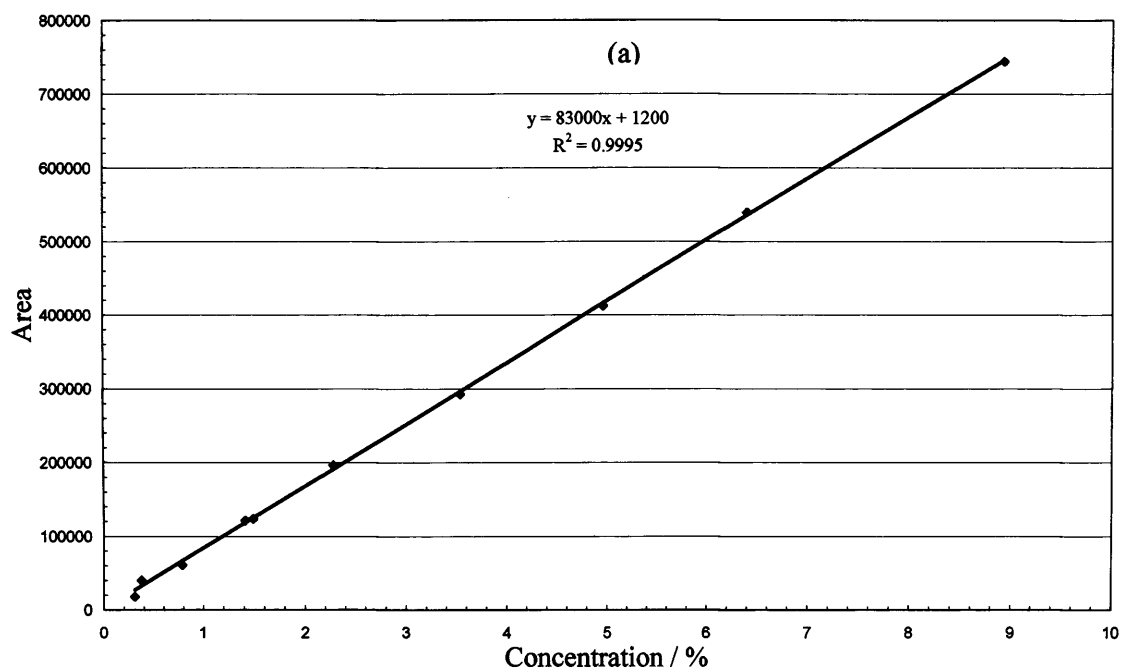


Figure 5.2 Plots of nett peak area of the K_{α} peak versus concentration for (a) Ca and (b) Zr. The uncertainty on each data point is the square root of the total counts; this error is insignificant on the scale used. A linear least squares fit to the data is shown with its equation and the correlation coefficient (r^2).

There were elements for which there was a poor correlation between peak area counts and concentration and the reasons for this are discussed in Section 5.7. The elements for which net peak area had a good correlation to the concentration, as indicated by the correlation coefficient, were Si ($r^2=0.9406$), K ($r^2=0.9922$), Ca ($r^2=0.9995$), Ti ($r^2=0.9772$), Fe ($r^2=0.9314$), Rb ($r^2=0.9786$), Sr ($r^2=0.8992$) and Zr ($r^2=0.9899$). A quantitative calibration was performed for these elements. Measurements were subsequently taken of the full complement reference materials. The relationship between the peak areas and corresponding concentrations provides the information necessary to implement the algorithm to convert the fluorescence intensities of elements in the sample of unknown composition into concentrations. The theoretical basis of this is the Backscatter Fundamental Parameter method.

5.4 The Backscatter Fundamental Parameter Method

Sherman (1955) was first to derive the formulation for the X-ray fluorescence intensities from a sample of known composition irradiated by an X-ray source emitting a polychromatic beam. The derivation applied the fundamental physics of X-ray fluorescence to the problem of the quantitative calibration of an X-ray Spectrometer as opposed to using an empirical relationship; hence this approach was called the Fundamental Parameter (FP) method.

A sample is composed of a set of elements at various concentrations, called the 'matrix', where the respective mass fractions of the elements sum to unity. To a first approximation, the intensity of an elemental fluorescence line is directly proportional to its concentration. However, 'matrix effects' occur where the intensity of both primary X-rays from the sources and fluoresced X-rays are affected by the presence of all the other elements in the sample (Potts, 1987). There is (i) attenuation of both the primary and fluoresced X-rays and (ii) enhancement of the fluorescence intensity of one element relative to another. For example, the Si K line has a strong intensity in silicate rocks owing to its typically large concentration (from 16 – 35 % by weight in the reference materials). The energy of the K_{α} line (at 1.74 keV) is greater than the Al K absorption edge at 1.56 keV. Consequently, it is possible for the Si K X-ray to be absorbed by Al atoms and to induce fluorescence from them. Therefore, the intensity of the Al K fluorescent X-rays is enhanced relative to the Si K X-rays.

The FP method is applicable to samples where the mass fractions of the elements detectable by the X-ray Spectrometer is equal to one. The Backscatter Fundamental Parameter (BFP) approach, first formulated by Nielson (1977), provides a method for determining the composition of samples with complex matrices where the fluorescence X-rays from some elements (typically

low in atomic number) in the sample are not detectable by the X-ray Spectrometer. These elements make up the 'dark matrix'. In the case of silicate rocks, a major component of the dark matrix is oxygen with a K_{α} X-ray line at 525 eV, which is below the lower energy limit of detection of the XRS.

The BFP approach adds two more equations to the FP approach: the intensities of the coherently and incoherently scattered Ag K_{α} radiation. The Ag K_{α} radiation coherently and incoherently scatters off the entire matrix, including those elements in the dark matrix. The intensity of this radiation allows the estimation of the atomic number and mass fraction of two additional elements assumed to represent the dark matrix of the sample. The BFP method applicable to dual source excitation using both ^{55}Fe and ^{109}Cd sources, as developed by Wegrzynek et al. (2003a, 2003b), has been utilised for the calibration of the XRS.

For a flat homogeneous sample, the relationship between the mass per unit area q of an element x and the nett count rate I of a characteristic line l (for the purposes of the derivation they will be considered to be K_{α} or K_{β} , although similar equations can be formulated for the L and M lines) can be written for the case of dual source excitation as (He and Van Espen, 1991):

$$q_x = \frac{I_{x,l}}{\varepsilon(E_{x,l}) \sum_{s=1,2} G'_s K_{x,l}(E_s) F_{x,l}(E_s, E_{x,l}) H_{x,l}(E_s, E_{x,l})} \quad (5-8)$$

Table 5.2 provides a summary of the meaning of the symbols employed for the derivation.

It can be seen that the BFP method takes several factors into account:

- Production cross section, K , of elements excited by primary X-rays of energy E
- Absorption correction, F
- Enhancement correction, H
- Geometric constant, G'_s , that incorporates the source strength and the source-sample-detector geometry
- The detector efficiency, ε

Symbol	Definition
q_x	Mass per unit area of element x (g/cm^2)
c_x	Weight fraction of element x
I_x	Nett count rate of element x (s^{-1})
$\varepsilon(E_{x,l})$	Relative detection efficiency for the characteristic radiation $E_{x,l}$
$s_{1,2}$	Radioisotope 1 ^{55}Fe , 2 ^{109}Cd
G_s	Geometric constant for source s (sr)
$G_{\text{Coh, Inc}}$	Geometric constant for coherent and incoherent Ag K (sr)
T_s	Half life of radioisotope source s (s)
E_s	Energy of primary X-rays from radioisotope source s
$I(E_s)$	Primary intensity at energy E_s
$K_{x,l}(E_s)$	Production cross section of the characteristic line l of the element x for the excitation with photons of energy E_s (cm^2/g)
$F_{x,l}(E_s, E_{x,l})$	Absorption correction factor for line l of element x
$F_{\text{Coh, Inc}}$	Absorption correction factor for coherent and incoherent scattered Ag K
$H_{x,l}(E_s, E_{x,l})$	Enhancement correction factor for line l of element x
ρ	Sample density (g/cm^3)
d	Sample thickness (cm)
θ_1, θ_2	Incident and exit angles (radians), defined in Figure 4.5
$\mu_x(E)$	Mass attenuation coefficient of element x for energy E (cm^2/g)
$\omega_{x,K}$	Fluorescence yield of K shell of element x
$p_{x,K\alpha}$	Emission probability for a K_α line of element x
$\Gamma_{x,K}$	Absorption edge jump ratio (the ratio of the mass attenuation coefficient at the top divided by that at the bottom of the K absorption edge of element x)
$\tau_x(E)$	Photoelectric mass absorption coefficient of element x for energy E (cm^2/g)
$\sigma_{\text{Coh}}, \sigma_{\text{Inc}}$	Mass cross sections for coherent and incoherent scattering of Ag K_α X-rays (cm^2/g)
$q_{A,B}$	Masses per unit area of the two elements, A and B, that represent the dark matrix (g/cm^2)
$E_{x,K}$	Energy of the K absorption edge for element x (keV)

Table 5.2 The symbols employed for the derivation of the BFP technique and their meaning.

The geometric constant, G'_s , changes with time according to the decay of the radioisotope sources and is given by:

$$G'_s = G_s I(E_s) \exp[-t \ln(2)/T_s]. \quad (5-9)$$

The production cross section $K_{x,l}$, when considering K shell X-ray emission only, is given by:

$$K_{x,l}(E_s) = \tau_x(E_s) \frac{r_{x,K} - 1}{r_{x,K}} \omega_{x,K} P_{x,K\alpha} \quad E_s \geq E_{x,K}. \quad (5-10)$$

Equation 5-10 defines the probability that the absorption of an X-ray photon will result in the emission of a K_α X-ray. τ is the cross section of photoelectric interaction resulting in the ionisation of an electron. The second term, involving the absorption jump ratio ($r_{x,K}$), is the fraction of the total absorption that results in the ionisation of K-shell electrons. ω_K , the fluorescence yield, is the probability that an atom will de-excite by the emission of a characteristic K X-ray (as opposed to an Auger electron). $p_{x,K\alpha}$ is the fraction of those atoms that emit a characteristic K_α X-ray (as opposed to K_β).

There is a decrease in intensity of both incidence and fluorescence X-rays due to absorption in the sample. The absorption correction is given by:

$$F_{x,l} = \frac{1 - \exp[-F_{x,l}^{Abs}]}{F_{x,l}^{Abs}}, \quad (5-11)$$

where:

$$F_{x,l}^{Abs} = \sum_{x=1}^n [q_x \times \mu'_x(\theta_1, E_s) + q_x \times \mu'_x(\theta_2, E_{x,l})], \quad (5-12)$$

$$\mu'_x(\theta_1, E_s) = \frac{\mu_x(E_s)}{\sin \theta_1}, \quad (5-13)$$

$$\mu'_x(\theta_2, E_{x,l}) = \frac{\mu_x(E_{x,l})}{\sin \theta_2}. \quad (5-14)$$

Equation 5-8 is the basis for the FP technique. The BFP technique extends the FP technique to account for the dark matrix which is assumed to be composed of two elements A and B. Two additional equations are added to describe coherent and incoherent scattering of Ag K_α radiation from both the dark matrix and the detectable elements in the matrix (Wegrzynek et al., 2003b) which are:

$$I_{Coh} = \varepsilon(E_{Coh})G'_{Coh} \left[\sum_{x=1}^n q_x \sigma_{Coh,x} + q_A \sigma_{Coh,A} + q_B \sigma_{Coh,B} \right] F_{Coh}, \quad (5-15)$$

$$I_{Inc} = \varepsilon(E_{Inc})G'_{Inc} \left[\sum_{x=1}^n q_x \sigma_{Inc,i} + q_A \sigma_{Inc,A} + q_B \sigma_{Inc,B} \right] F_{Inc}, \quad (5-16)$$

$$G'_{Coh} = G_{Coh} I(E_s) \exp[-t \ln(2)/T_2], \quad (5-17)$$

$$G'_{Inc} = G_{Inc} I(E_s) \exp[-t \ln(2)/T_2]. \quad (5-18)$$

The fluorescence yields were taken from the data given by Krause (1979). The mass attenuation coefficients and the photoelectric mass absorption coefficients are from McMaster et al. (1968). The coherent and incoherent scattering coefficients are taken from data by Hubbell et al. (1975). The absorption edge jump ratio is taken from a least squares fitted polynomial function based on the tables in McMaster et al. (1968). The transition probabilities for the K and L lines are from Scofield (1974a, 1974b). All of these data are contained within the Fundamental Parameter

Calculator Software as developed by the IAEA (2005). Equations 5-8, 5-15 and 5-16 form the basis of the BFP algorithm. The incident, exit and Compton scatter angles are defined in Figure 4.5.

5.5 Calculation of the Geometric Constant and Average Incidence and Exit Angles

The implementation of the Backscatter Fundamental Parameter method requires that the ratio of the geometric constants G'_{Fe}/G'_{Cd} , G'_{Coh} , G'_{Inc} and the average incidence (θ_1) and exit (θ_2) angles (defined in Figure 4.5) from Equation 5-8 are established. G'_{Coh} and G'_{Inc} can be evaluated using a standard sample of known composition using the following expressions:

$$I_{Coh} = \varepsilon(E_{Coh})G'_{Coh} \left[\sum_{x=1}^n q_x \sigma_{Coh,x} \right] F_{Coh}, \quad (5-19)$$

and:

$$I_{Inc} = \varepsilon(E_{Inc})G'_{Inc} \left[\sum_{x=1}^n q_x \sigma_{Inc,i} \right] F_{Inc}. \quad (5-20)$$

For the XRS, the average incidence and exit angles were established from measurements of reference materials G-2 and BCR-1 and pure elements / compound SiO₂, V, Cu and Zr. The samples were not excited using the ⁵⁵Fe and ¹⁰⁹Cd sources simultaneously, but instead from solely either the pair of ⁵⁵Fe or ¹⁰⁹Cd sources. Measurements were made with an Al foil of thickness d (40 μm) covering the sample and then repeated without the foil in place.

If the enhancement factor is ignored ($H = 1$), the intensity of fluorescence X-rays from the element x, $I_{x,l}^E$, from Equation 5-8 is:

$$I_{x,l}^E = G'_s \varepsilon(E_{x,l}) q_x K_{x,l}(E_s) F_{x,l}(E_s, E_{x,l}). \quad (5-21)$$

When Al foil covers a sample, it attenuates both the primary X-rays incident on the foil and

fluorescent X-rays from the sample along the path length $d / \sin\theta$. The intensity with the foil in front of the sample, $I_{x,l}^{E+F}$, is:

$$I_{x,l}^{E+F} = I_{x,l}^E \exp\left(-\mu_{Al}(E_s)\rho_{Al} \frac{d_{Al}}{\sin\theta_1}\right) \times \exp\left(-\mu_{Al}(E_{x,l})\rho_{Al} \frac{d_{Al}}{\sin\theta_2}\right). \quad (5-22)$$

Rearranging Equation 5-22 yields:

$$\frac{I_{x,l}^E}{I_{x,l}^{E+F}} = \exp\left(\left[\frac{\mu_{Al}(E_s)}{\sin\theta_1} + \frac{\mu_{Al}(E_{x,l})}{\sin\theta_2}\right]\rho_{Al}d_{Al}\right). \quad (5-23)$$

Equation 5-23 can be rearranged to obtain:

$$\frac{\overbrace{1}^y}{\mu_{Al}(E_s)\rho_{Al}d_{Al}} \ln\left(\frac{I_{x,l}^E}{I_{x,l}^{E+F}}\right) = \frac{\overbrace{1}^m}{\sin\theta_2} \frac{\overbrace{\mu_{Al}(E_{x,l})}^x}{\mu_{Al}(E_s)} + \frac{\overbrace{1}^c}{\sin\theta_1}. \quad (5-24)$$

Equation 5-24 is the equation for a straight line with gradient, m , dependent on θ_2 , and intercept, c , dependent on θ_1 . The measured intensities of fluorescent X-rays with a covering of foil over the sample ($I_{x,l}^{E+F}$) and without one ($I_{x,l}^E$) can be used to calculate y . The value of x is derived from the mass attenuation coefficients of Al at the energies of the source (E_s) and fluorescent X-rays ($E_{x,l}$). This values of x and y were plotted in Figure 5.3 and a linear least squares fit was fitted to the data. The values of the intercept and gradient are $c = 1.4 \pm 1$ and $m = 1.07 \pm 0.04$. The incidence and exit angles were calculated from Equation 5-24 to be $\theta_1 = 44 \pm 41^\circ$ and $\theta_2 = 69 \pm 5^\circ$.

The average exit angle, θ_2 , at $69 \pm 5^\circ$, as determined by the gradient of the line, has a relatively small uncertainty. However, the incidence angle, θ_1 , at $44 \pm 41^\circ$ has a relatively large uncertainty associated with it due to the scatter of data points near the intercept. Therefore, a different method had to be adopted to determine θ_1 which utilised the angle of Compton scattered Ag K_α radiation. The Compton scatter angle, ϕ , is given by:

$$\cos \phi = 1 - mc^2 \left(\frac{1}{E_{AgK,Coh}} - \frac{1}{E_{AgK,Inc}} \right), \quad (5-25)$$

where mc is the rest energy of an electron (511 keV), $E_{AgK,Coh}$ and $E_{AgK,Inc}$ are the energy of the coherently and incoherently scattered Ag K_α radiation respectively. The value of $E_{AgK,Coh}$ is 22.16 keV. The value of $E_{AgK,Inc}$ was measured from spectra.

The Compton scatter angle is the sum of the incidence and exit angles (Equation 4-8).

The average scatter angle for 10 reference materials, as calculated for the Ag K_α line, was found to be $(124 \pm 6^\circ)$. Taking the exit angle as $\theta_2 = 69 \pm 5^\circ$, the incidence angle is calculated to be $\theta_1 = 55 \pm 8^\circ$.

The design values of the incidence and exit angles are $\theta_1 = 60^\circ$ and $\theta_2 = 90^\circ$. The value of $\theta_1 = 55 \pm 8^\circ$ agrees with the design value. This angle set by the geometry of the CFRP cap. However, the exit angle at $\theta_2 = 69 \pm 5^\circ$, is different to the design value. This arises from differences in the actual geometry of the instrument to the ideal designed case. For the FS XRS, the detector window is not exactly central in the CFRP aperture but instead is slightly offset. Measurement of the actual offset geometry of the FS XRS shows that the exit angle is actually $81 \pm 1^\circ$. This discrepancy can be explained by the fact that the detector in its housing could be slightly offset from the centre. However, these angles are directly derived from the linear least squares fit line to the data shown in Figure 5.3. This has a gradient that is heavily dependent upon the data point at $x \sim 84$, $y \sim 92$ and an intercept that is dependent on the cluster of points near the origin. If systematic errors are introduced into the y value of the (84, 92) data point from inaccurate peak fitting then this can strongly influence the gradient of the line and hence the exit angle. Another factor to consider is that the FP method assumes that the incidence and exit angles are well collimated whereas in reality the X-rays are emitted by the source and incident on the detector in a solid angle.

To determine the ratio of the geometric constants for each source, G_{Fe} / G_{Cd} , measurements of a pure elemental sample V was made. Each measurement was made by excitation utilising either the pair of ^{55}Fe or ^{109}Cd sources.

Typically, $F_{x,i}^{Abs} \gg 1$ for a pure element sample and so the absorption factor (Equation 5-11)

becomes:

$$F_{x,l} = \frac{1}{q_x \left[\frac{\mu_x(E_s)}{\sin \theta_1} + \frac{\mu_x(E_{x,l})}{\sin \theta_2} \right]}. \quad (5-26)$$

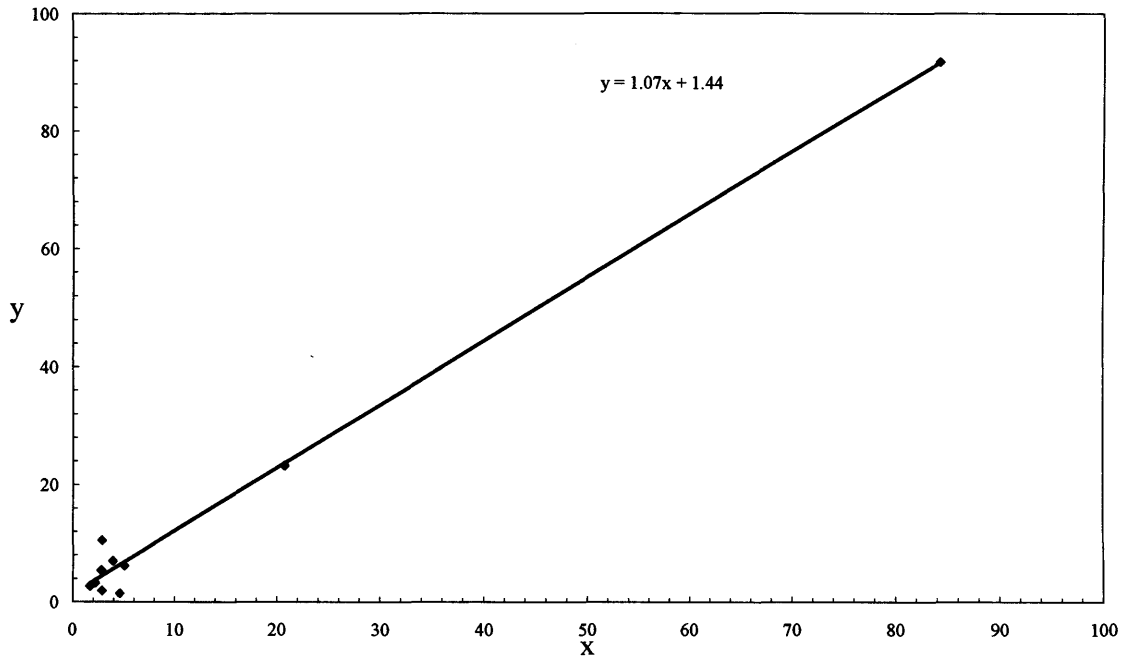


Figure 5.3 Plot of the values of x and y as defined in Equation 5-21. A straight line fit of the data is shown whose gradient and intercept determines the average incident and exit angles.

Assuming the enhancement is negligible ($H = 1$) and substituting into Equation 5-26 into Equation 5-8, we obtain:

$$N_{x,l,s} = G'_s \varepsilon(E_{x,l}) K_{x,l}(E_s) \frac{1}{\frac{\mu_x(E_s)}{\sin \theta_1} + \frac{\mu_x(E_{x,l})}{\sin \theta_2}} t_s. \quad (5-27)$$

Where $N_{x,l,s}$ is the number of counts in a given peak l of element x excited by radioisotope source

s.

The ratio of the number of counts in a peak l of element x excited by ^{55}Fe and ^{109}Cd separately, $N_{x,1}/N_{x,2}$, can be used to obtain the geometric ratio using the following expression:

$$\frac{G'_{Fe}}{G'_{Cd}} = \left\{ \frac{N_{x,l,Fe}}{N_{x,l,Cd}} \right\} \left\{ \frac{K_{x,l}(E_{Cd})}{K_{x,l}(E_{Fe})} \right\} \left\{ \frac{\frac{\mu(E_{Fe})}{\sin \theta_1} + \frac{\mu(E_{x,l})}{\sin \theta_2}}{\frac{\mu(E_{Cd})}{\sin \theta_1} + \frac{\mu(E_{x,l})}{\sin \theta_2}} \right\} \left\{ \frac{t_{Cd}}{t_{Fe}} \right\} \quad (5-28)$$

The ratio $N_{x,Fe}/N_{x,Cd}$ is found from measurement of the nett peak areas of fluorescent peaks excited by either the ^{55}Fe or ^{109}Cd sources. The live time, t, was obtained by measurement of the real time and calculated using Equation 4-19. The values of θ_1 and θ_2 are the average incidence and exit angles calculated previously. The geometric constant for $V K_\alpha$ was estimated as 2.2 ± 0.2 . This estimated value was subsequently optimised during the quantitative calibration (Section 5.6).

5.6 Quantitative Calibration

The parameters necessary for the BFP method to be executed, namely the average incidence and exit angles (θ_1 and θ_2) and the geometric ratio (G'_{Fe}/G'_{Cd}) were calculated. At this stage, the relationship between the nett peak intensity of each element and its concentration was established. A single reference material, G-2, was selected for this calibration and its certified concentration was inserted into the algorithm. The algorithm calculates the coefficients of absorption and enhancement with knowledge of the intensities of the fluorescent lines and the concentration of the constituent elements in the reference material.

In the BFP algorithm, the calculation of absorption and enhancement corrections are started using initial concentrations calculated from measured fluorescent count rates and the instrument sensitivities (counts per second per unit concentration of a given element). Then a new set of concentrations are calculated, taking into account the matrix corrections (including the dark matrix). This procedure is repeated until the relative difference between the concentration results for all elements of two successive iterations is less than 0.1% (Wegrzynek et al., 2003a).

The algorithm was used to determine the concentration of the reference materials BHVO-1 and

GH using the geometric ratio 2.2 ± 0.2 . The overall χ^2 value between the estimated concentrations and the certified concentrations was calculated for several elements. Then the geometric ratio was slightly adjusted in the algorithm, and a quantitative analysis of the reference materials repeated and the χ^2 calculated again. This continued until a value of the geometric ratio was found such that the χ^2 reached a minimum. The optimum geometric ratio G_{Fe}/G_{Cd} was 2.8 ± 0.2 . This value was used for the quantitative analysis of the remaining reference materials.

Measurements of the full suite of reference materials were performed and their estimated compositions obtained. For each analysed element in the reference materials, there was a linear trend between the estimated and certified concentrations. The results for Ca and Zr are shown in Figure 5.4.

It can be seen from Figure 5.4 that the linear least squares fit line for the elements exhibits a systematic bias; the relationship between the estimate and certified concentration is not one-to-one. This non-unity gradient originates from errors in the values of the geometric ratio, the angles of incidence and exit and the detection efficiency. This results in a systematic over or under estimation of the concentrations relative to the certified concentrations. The non-zero intercept originates from the spectral fitting stage where the background is over or under estimated. In addition, outliers in the data that deviate from the general linear trend can influence the gradient and intercept of the linear least squares fit. These bias plots establish a correction that can be applied to the estimation of the composition of samples of unknown composition. The correction is specific for each element and determined from the gradient and intercept of the linear least squares fit line of the data.

Several of the plots had outliers where the concentration of an element was over or under estimated by a significant amount. In general these outliers were not rejected from the plots because they are systematic errors introduced as a direct consequence of the quantitative calibration and spectral fitting used for the XRS. The plot for Ca in Figure 5.4 has two outliers corresponding to AGV-1 and OU-2. The origin of the outliers arose from the application of the BFP algorithm which overestimated the concentration of Ca in these reference materials. The BFP method estimates a weight fraction of fluorescent element i , c_i , from the mass per unit area of the analysed element, q_x , the total mass per unit area of the detected fluorescent elements in the spectrum, q_b , and the total mass per unit area of the elements in the dark matrix, q_d , using the following expression:

$$c_i = \frac{q_x}{q_f + q_d}$$

(5-29)

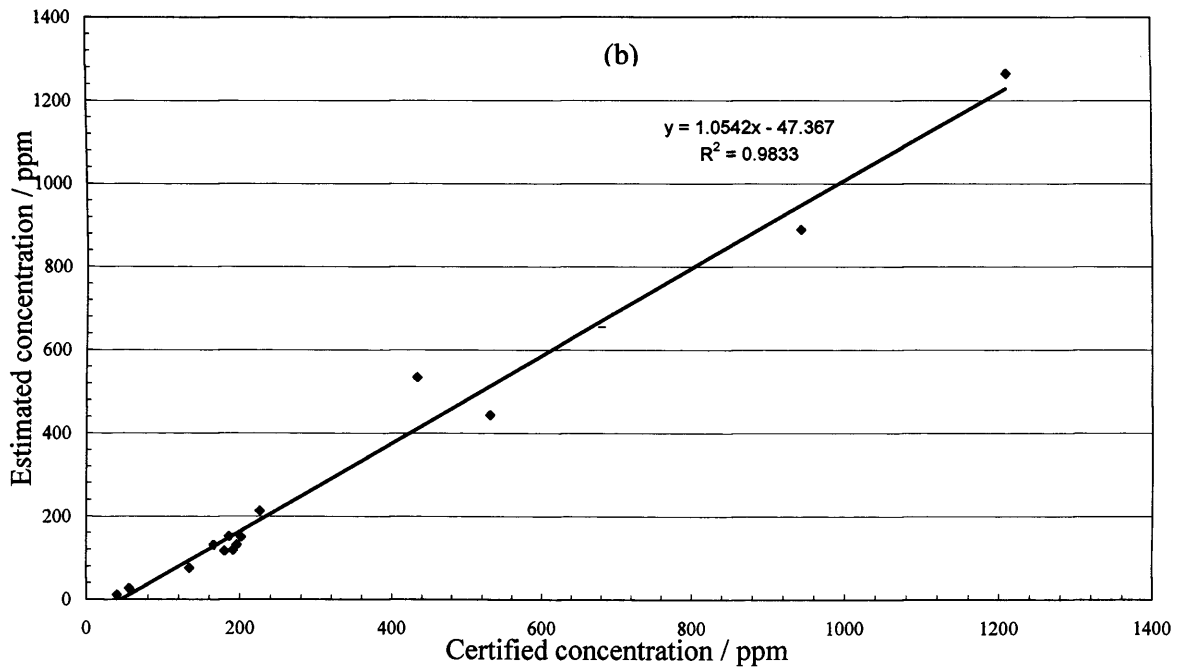
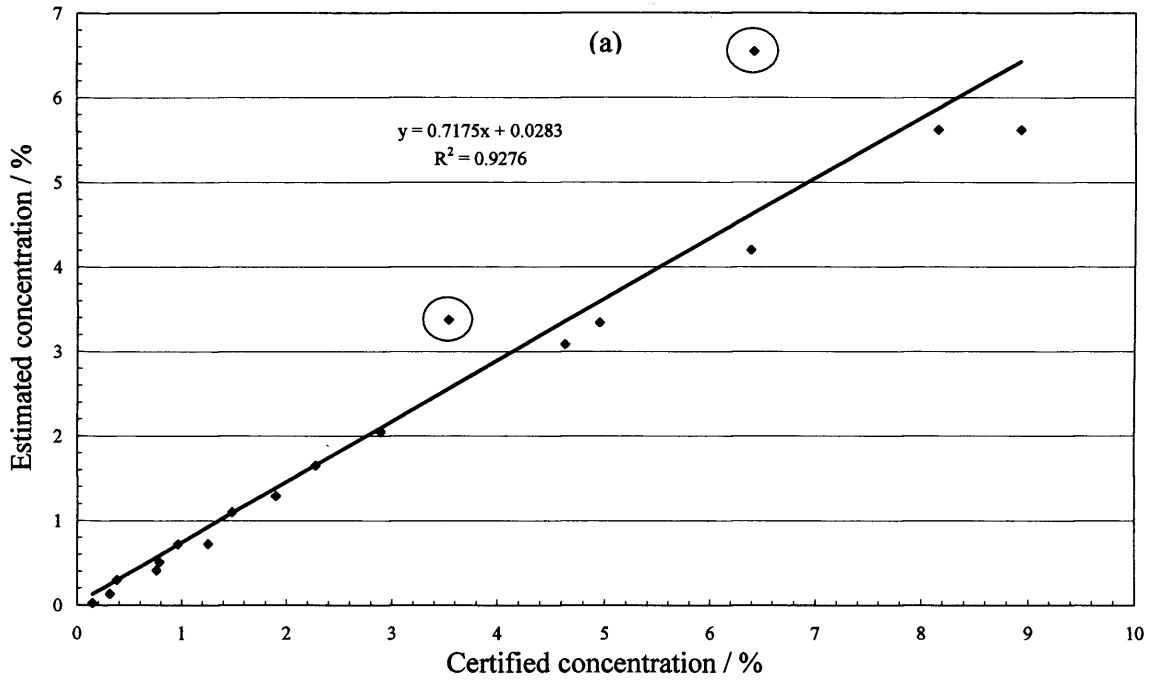


Figure 5.4 The estimated versus certified concentration for Ca (a) and Zr (b). A linear least squares fit to the data is shown with its equation and the correlation coefficient. The circled points in the Ca plot are classified as outliers from the general linear trend.

For the BFP algorithm to correctly estimate q_d , accurate fitting of the Rayleigh and Compton Ag K scatter peaks (Van Gysel et al., 2003) is required. For a small number of reference materials, the area of the Compton scattered Ag K peak was not accurately determined using the fitting procedure employed in AXIL. Any outliers in the bias plots for the analysed elements, such as those in the Ca plot in Figure 5.4, generally arose when q_d was mis-estimated. For example, if q_d is under-estimated then, from Equation 5-30, the weight fraction of any particular element in the sample (c_i) is over-estimated. The mis-estimation of q_d has a greater effect on the estimated concentration of elements present in a greater abundance, particularly Si, than the trace elements. Consequently, there are also outliers corresponding to AGV-1 and OU-2 in the bias plots for other major elements (Fe, Ti, Si). Figure 5.5 is a schematic of the relationship between c_i and q_d from Equation 5-30. The red curve is the relationship where q_x is relatively large (eg, for Si) while the green curve is where q_x is relatively small (eg, for Zr). For a given difference in q_d between the true q_d and the estimated q_d then this produces a larger systematic error in the estimated concentration of a major element than a trace element.

In addition, the BFP method relies on accurate peak areas for the detected fluorescent elements within the spectrum in order to calculate q_f . This applies particularly Si since this is a major component present in tens of percent by weight. However, for Si accurate peak fitting can prove difficult since in that region there is significant overlap with neighbouring lines such as Al K.

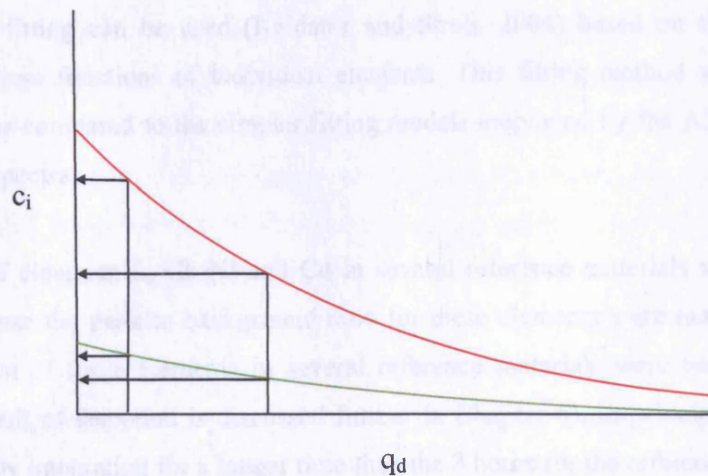


Figure 5.5 A plot showing the relationship between q_d and c_i from Equation 5-30. It shows that for a given systematic error in the value of q_d , the corresponding error on concentration c_i of a major element (red curve) is larger than for a minor element (green curve).

5.7 Discussion

There are two areas where the calibration of the XRS can be improved: the spectral fitting to derive elemental peak areas and the application of the BFP algorithm for quantitative analysis.

An indication of the quality of the performance of the spectral fitting stage is the correlation between the nett peak area and the certified concentration such as that shown in Figure 5.2 for Ca and Zr. There were several major and minor elements whose peak area could not be accurately fitted and consequently there was a poor correlation between the certified concentration and the nett peak area. There are a number of reasons for inaccurate fitting of peak areas. The peak can overlap with neighbouring peaks with the degree of overlap dependent upon the resolution of the spectrometer. In addition, the peak area to background ratio can be too small because the concentration of the element in the sample is less than the detection limit.

The peak areas of elements Na, Mg, Al and P could not be accurately fitted because of the peak overlap as a result of the insufficient resolution of the XRS and close proximity of these peaks. Also, the dominance of the Si K peak in the region makes it difficult to fit the smaller peaks. Indeed, there were difficulties in the accurate determination of the Si K peak area itself because of overlap with weaker neighbouring peaks. Another smaller interference in this region was the relatively weak “Compton shoulder” at ~1.5 keV which was subtracted as background from the reference material spectra. In order to improve fitting of these elements, a more sophisticated

method of peak fitting can be used (Kaldarar and Streli, 2004) based on the experimentally determined response functions of individual elements. This fitting method was found to give superior results as compared to the simpler fitting models employed by the AXIL software used to analyse XRS spectra.

The peak area of elements S, Cl, Ni and Cu in several reference materials was not accurately determined because the peak to background ratio for these elements were not sufficiently high. The concentration of these elements in several reference materials were below their limit of detection (the limit of detection is discussed further in Chapter 6). In principle, these elements can be detected by integrating for a longer time than the 3 hours for the reference materials. Also, many of these peaks again suffered from overlap with much stronger neighbouring peaks. The determination of Ni is more problematic since it is present as a spectral artefact, arising from X-ray fluorescence of the detector housing. However, the intensity of the Ni line in the reference material was corrected for the contribution from Ni X-rays in the background.

The elements for which the XRS were calibrated were those with a reasonable correlation between the nett peak area and certified concentration. These were the major elements K, Ca, Ti, Fe and the trace elements Rb, Sr and Zr. The K peak suffered from overlap with the Ca peak. The K peak was often weaker and appeared as a shoulder on the low energy side of the Ca peak making accurate spectral fitting difficult. In contrast, the elements Ca and Ti show a strong correlation between the area and certified concentration since these peaks were often intense in spectra of reference materials. There was significant overlap between Fe K_{α} and Mn K_{β} where the Mn K radiation arises from the ^{55}Fe sources. Wegrzynek et al. (2003a) used AXIL to fit spectra of soil samples that contained a large amount of Mn. There was a large discrepancy for the estimated Mn concentration compared to the certified version due to the large peak overlap of the Mn K_{α} peak with an intense Fe K_{α} peak. Overall, the limiting factor in the performance of AXIL to fit overlapping lines was the resolution of the XRS.

An indication of the quality of the performance of the quantitative analysis is an examination of the correlation between the estimated and the certified concentration such as that shown in Figure 5.4 for Ca and Zr. The application of the BFP algorithm for quantitative analysis had an effect on both the scatter of the points in these plots and the presence of outliers. The scatter in points in the estimated versus certified concentration plots (Figure 5.4) is greater than that in the peak area versus certified concentration plots (Figure 5.2) for the reference materials. Therefore the

application of the quantitative analysis algorithm, while successfully predicting a concentration from the peak area, has introduced systematic errors. Therefore, in this case there is some merit in applying the simple method of measuring elemental intensities and using the calibration lines established by measurements of the reference materials, such as Figure 5.4, to predict elemental concentrations. This is a consequence from Equation (5-8) which states that if absorption and enhancement corrections are ignored then the concentration is directly proportional to the intensity. However, the accuracy of this method is limited by matrix effects, specifically the terms F and H in Equation (5-8), and incomplete knowledge of the dark matrix corrections which are both corrected for by the quantitative algorithm. Therefore it is justified to improve the BFP algorithm by addressing its limitations since ultimately it can prove to produce more accurate results than empirical methods.

The first such improvement is to avoid the use of simple methods to determine the net Compton Ag K_α peak intensity since these can lead to inaccurate results. Peak fitting is difficult for the Compton Ag K_α peak due to the non-Gaussian shape and a simple peak integration technique is used in AXIL to sum the channel contents over the region of interest. Methods that use the coherent scatter intensity for the correction of the dark matrix, such as the BFP algorithm, are more sensitive to inaccurate peak area determination. Specialised fitting models for fitting these peaks can be used, such as those developed by He and van Espen (1991) and Van Gysel et al. (2003) and have shown to improve the BFP technique. These models were not implemented since they were not incorporated in the AXIL software employed for spectral fitting of XRS spectra. A better estimation of the average incidence and exit angles, from Figure 5.3 and Equation (5-24), requires more data points to better establish the gradient and intercept of the best fit line. This can be achieved by performing measurements of elements with a range of mass attenuation coefficients, which will influence the x values in Equation (5-24).

Alvarez et al. (2004) has examined the application of the BFP technique and questioned the use of Compton scatter peaks in the case of annular source excitation (equivalent to disc sources) to provide information about the dark matrix and correct for matrix effects. The FP method relies on the assumption that the incident beam and exit beam are well collimated and represented by average incidence and exit angles. However, in the case of excitation using radioisotope sources, the assumption of an average angle of incidence and exit is questionable. In addition, Alvarez et al. (2004) confirmed experimentally that G_{Inc} and G_{Coh} are not constant but are a function of the average atomic number of the sample. Also, these factors are a function of the Compton

scattering angle. For the experimental setup employed for Alvarez et al. (2004), the range of scattering angles for the Ag K radiation was between 100° and 150° as compared to an average angle of 124° for the XRS. The observed scattering intensities, used in the matrix correction procedure, can also be altered by scattering that occurs in the instrument rather than the sample. However, Alvarez et al. (2004) found that the BFP technique when applied to the analysis of soil and sediment samples gave a satisfactory performance. This was because the geometric factor does not significantly vary for the average atomic numbers of reference materials derived from soils and silicate rocks.

5.8 Summary

This chapter has described the calibration process for the XRS. It outlined the basis for spectral fitting of spectra using least squares fitting of peaks and background. The spectra of several reference materials were fitted and for each element, the net intensities of the peaks were linearly correlated with the concentration. This chapter described the theoretical basis for the Backscatter Fundamental Parameter method that was employed for the quantitative calibration. The parameters necessary for the BFP technique to be implemented, namely the average angles of incidence and exit and the geometric ratio were established experimentally for the XRS. Finally, the results from the implementation of the technique to estimate the concentration of a suite of reference materials were presented. Chapter 6 will use the quantitative analysis of the reference materials to compare the analytical performance of the XRS with other X-ray spectrometers.

Chapter 6

The Comparative Analytical Performance of the X-ray Spectrometer

This chapter evaluates the analytical performance of the XRS using three criteria: accuracy, detection limit and fitting precision. The analytical performance of the XRS was compared with (i) a terrestrial portable X-ray fluorescence (PXRF) instrument and (ii) a conventional laboratory wavelength-dispersive X-ray fluorescence instrument (WD XRF). The results of this study indicate several possible improvements to the analytical performance of future versions of the XRS (Talboys et al., 2005).

6.1 Introduction

The analytical performance of the XRS characterises the quality of the geochemical data from its analyses. A full characterisation of the Beagle 2 XRS analytical performance in comparison to other terrestrial X-ray spectrometers enables identification of key design features that impact upon its accuracy, detection limit and fitting precision. The comparative analytical performance of the spectrometers was experimentally determined from the geochemical analysis of reference materials and evaluated using these criteria. Two XRF spectrometers were chosen for a comparison with the FS XRS because each one had a unique capability that is desirable for the FS XRS. The first instrument was a field portable energy-dispersive spectrometer that has been fully characterised for terrestrial *in situ* fieldwork (Potts et al., 1995). The second instrument was a wavelength-dispersive spectrometer (Ramsey et al., 1995), typical of similar spectrometers that are widely used in geochemical research laboratories so that an evaluation can be made against “research grade” geochemical data. Both instruments are based at the Department of Earth Sciences, Open University. Two aspects of the XRS make it unique compared to these commercially available spectrometers. Firstly, it was designed to be robust enough to survive launch, transit to Mars, landing and operations on the Martian surface (Sykes and Whitehead, 2000, 2003; Sykes 2003b). Secondly, it was highly miniaturised in order to be accommodated on the Beagle 2 lander.

6.2 Experimental

Each spectrometer analysed a subset of an overall suite of reference materials but with some common materials shared between all the spectrometers. The composition and supplier of the reference materials are given in Chapter 5, Section 5.2.

The suite of reference materials were analysed by the FS XRS in the experimental arrangement described in Chapter 3, Section 3.4. The integration time for each reference material was 3 hours in order to achieve an adequate number of counts for the elemental lines of interest.

Table 6.1 summarises the characteristics of the X-ray Spectrometers used in the comparison. The first instrument against which the XRS analytical performance was compared was a portable X-ray spectrometer designed for terrestrial fieldwork. It was a Spectrace TN 9000* (Figure 6.1), that consisted of two parts: a probe and an analyser. The probe consisted of a sealed aluminium enclosure containing the X-ray detector and three radioisotope sources. The probe aperture was sealed with a plastic film on which the sample was placed. The analyser provided data acquisition, data processing and display capabilities. The dimensions of the probe were 127 × 76 × 216 mm with a mass of 1.9 kg while the analyser had dimensions of 320 × 300 × 100 mm and a mass of 6.7 kg. The instrument utilised ⁵⁵Fe (1800 MBq), ¹⁰⁹Cd (180 MBq) and ²⁴¹Am (180 MBq) radioisotope sources for primary excitation which excited the sample sequentially. The fluoresced X-rays from the sample passed through the probe aperture and were detected by a solid state mercury (II) iodide X-ray detector with a resolution of 260 eV FWHM at Mn K_α (Potts et al., 1995). Spectra were obtained by exciting the sample with each source in turn for 100 s live time and recorded via a 2000 channel MCA built into the analyser component of the PXRF. The quantitative analysis was derived from the elemental intensities using the Fundamental Parameter method implemented in the analyser's software which assumes the 'dark matrix' is composed of SiO₂.

The second instrument was an ARL 8420+ dual goniometer wavelength-dispersive XRF spectrometer, with a Rhodium anode 3 kW end-window X-ray tube operated at 60 kV and 40 mA. The fluorescent X-rays from elemental lines Rb K_{α1}, Sr K_{α1} and Zr K_{α1} were detected using a scintillation counter with a fine collimator using a LiF(200) crystal (2d = 1.652 Å) for a live time of 70 s. The ARL 8420 had dimensions of 135 × 87 × 104 cm and a mass of 1200 kg. Trace elements were matrix corrected by normalising elemental intensities to the intensity of Compton scattered tube lines.

Each spectrometer analysed a different range of elements. As described in Chapter 5, the FS XRS analysed major elements Si, K, Ca, Ti and Fe and trace elements Rb, Sr and Zr. The PXRF is not capable of analyzing elements with atomic number, Z, less than 19 (Potassium) because of its

* Formerly manufactured by TN Technologies Inc. (Round Rock, Texas, USA)

low detection efficiency at energies less than ~ 3 keV (Potts et al., 1995) due to X-ray absorption by the detector encapsulation to protect it against the effects of moisture (Bradley et al., 1989; Iwanczyk et al., 1990). The WD XRF was optimised for the quantitative analysis of trace elements only.

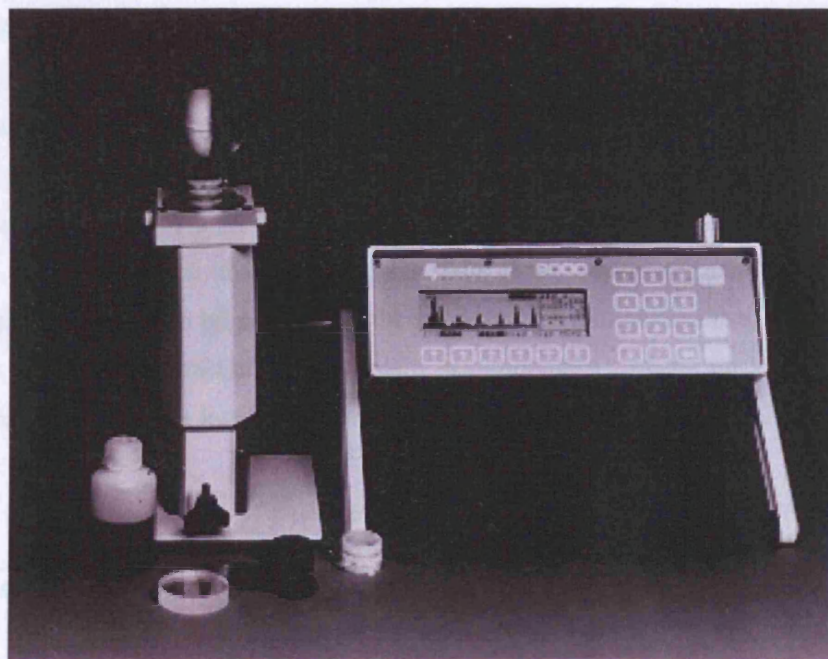


Figure 6.1: The Spectrace TN9000 PXRF with probe (left) and analyser (right).

X-ray Spectrometer	Detector type	Excitation Source	Count time (s)	Resolution at FWHM Mn K _α (eV)	Mass
FS XRS	Si-PIN	2 x ⁵⁵ Fe (56.5, 49.1 MBq) 2 x ¹⁰⁹ Cd (4.32, 4.45 MBq) Simultaneous excitation	10800	391	58+98g
PXRF	Mercuric (II) Iodide	⁵⁵ Fe (1800 MBq) ¹⁰⁹ Cd (180 MBq) ²⁴¹ Am (180 MBq) Sequential excitation	100	260	6.7+1.9 Kg
WD XRF	Scintillation counter + LiF crystal	Rh X-ray tube 3 kW (max)	70	~50	1200 Kg

Table 6.1 A comparison of the characteristics of the X-ray Spectrometers. The source strengths are reported to the date of measurement. The integration times for each instrument were set to those used for a typical measurement of reference materials.

6.3 Results

6.3.1 Fitting Precision

The precision is a measure of the repeatability of a measurement. For XRS analyses, the precision of an analysed elemental concentration is limited by the uncertainty on its corresponding peak area (set by Poisson statistics) calculated at the spectral fitting stage.

The spectral fitting performed for both the PXRF and the XRS finds the least squares fit of a function, representing both the background and the peaks, to the spectrum (see Equation 5-1). The uncertainty in the peak areas is derived from both Poisson statistics and the uncertainty in the parameters of the function that best fit the data (Van Espen and Janssens, 2002). The uncertainties result from the propagation of the statistical fluctuations in the spectral data into the parameters of the fitting function. The standard deviation, $\sigma(A)$, of the peak area, A , for large interference-free peaks on a low background is close to that expected from Poisson statistics and is given by:

$$\sigma(A) \approx \sqrt{A} . \quad (6-1)$$

In contrast, a peak on a high background and that has significant overlap interference with neighbouring peaks, has an uncertainty on its peak area larger than that expected from Poisson statistics, given by:

$$\sigma(A) > \sqrt{A} . \quad (6-2)$$

The uncertainty in the concentration derived from the fitting can be compared to the Horwitz function (Thompson, 2004; Thompson and Lowthian, 1997), which relates the concentration of an element to its standard deviation. The Horwitz function is an empirical function that relates the analysed concentration of an element to its associated relative standard deviation. This function states that as the concentration of the element decreases by two orders of magnitude, the relative standard deviation (RSD) increases by a factor of two. For example, at an element concentration of 100% the RSD is 2%, whereas at a concentration of 1% the RSD increases to 4%. This relationship has been found to hold regardless of the analytical methods and the test material employed. It was originally derived from an inter-laboratory performance study of the

compositional analysis of foods (Horwitz et al., 1980) but has wider applications. In particular, the Horwitz function holds for the geochemical analysis of silicate rocks using a variety of techniques. For example, the standard deviation of the compositional analysis of volcanic glasses by two methods, laser-ablation inductively-coupled-plasma mass spectrometry and electron microprobe (Potts et al. 2002), followed the Horwitz function over a large concentration range from 10^{-1} to 10^{-6} g/g. The empirical Horwitz function has not been explained from first principles but explanations for its existence are based around it representing a fitness for purpose benchmark for appropriate areas of analytical chemistry including silicate rock analysis (Thompson, 1999). Suppose an instrument was used for elemental analysis but its RSD on analysed concentrations was excessively high. Hence this instrument would not be used for these analyses in future since its performance is not fit for its purpose. Therefore, this instrument does not contribute to defining the Horwitz function. The instrument analyses that do define the function are those whose analytical performance is of sufficiently high quality to be useful for the purpose of elemental analysis, and hence it can be used as an appropriate benchmark.

The Horwitz function can be used as an appropriate benchmark (for fitness-for-purpose) against which to compare the standard deviation of the element concentrations in reference materials as analysed by the X-ray spectrometers under study. It has already been used as a benchmark for inter-laboratory proficiency tests for silicate rock analysis using a variety of techniques including X-ray fluorescence (Thompson et al., 1997). The Horwitz function relates the standard deviation, σ_H (g/g), to the concentration of element i , C_i (g/g) and is given by (Horwitz et al., 1980):

$$\sigma_H = 0.02C_i^{0.8495} \quad (6-3)$$

In logarithmic form Equation 6-3 can be expressed as:

$$\log_{10} \sigma_H = 0.8495 \log_{10} C_i - 1.6990 \quad (6-4)$$

The Horwitz function expressed as the RSD is given by:

$$RSD(\%) = \frac{\sigma_H}{C_i} \times 100 = 2.C_i^{-0.1505} \quad (6-5)$$

The analysed concentrations of elements in all the reference materials were plotted against their respective standard deviations and compared to the Horwitz function for the FS XRS and PXRF (Figure 6.2). The FS XRS and PXRF were compared to evaluate the effect of resolution on the performance of the least squares spectral fitting algorithm implemented for energy-dispersive spectrometers. The data points at high concentration ($\log\{\text{concentration}\} \sim -0.1$ to -0.9) correspond to Si whereas those at low concentrations ($\log\{\text{concentration}\} \sim -4.1$ to -5.2) correspond to the trace elements Sr and Zr. The data points with concentrations in between these concentrations correspond to the major elements K, Ca, Ti and Fe.

For both spectrometers, the RSD generally conforms to the Horwitz function over several orders of magnitude of concentration from 10s of percent to 10s of parts per million. For the XRS data, the standard deviation has an even scatter around the Horwitz function. For the PXRF, the standard deviation for the major elements Ca, K and Fe outperforms that predicted by the Horwitz function. In particular, there is a strong linear correlation between the $\log\{\text{standard deviation}\}$ and $\log\{\text{concentration}\}$ for each of these elements. For the trace elements the standard deviation is above the benchmark set by the Horwitz function because the concentration is less than or close to the detection limits for those elements.

The scatter of the points about the Horwitz function is larger for the FS XRS than the PXRF due to the larger uncertainty in the peak areas derived from spectral fitting as a direct result of the better resolution of the PXRF. The consequences of a poorer resolution for spectral peaks is that it introduces greater overlap with neighbouring lines and lower signal to noise ratios (Potts, 1987). This contributes to a larger uncertainty in peak areas and ultimately a larger uncertainty on the concentrations. A difference in resolution of 130 eV between the FS XRS and PXRF can produce significant differences in the fitting uncertainty. For example, the degree of overlap between Ca K_{α} and K K_{β} peaks increases from 33 to 44 % in spectra of resolution 138 and 165 eV at Mn K_{α} respectively. In addition, for a spectrometer with a resolution of 138 eV at Mn K_{α} , the background area under the Ca K_{α} line increases by 12 % and 25 % for detector resolutions 151 eV and 165 eV respectively.

Generally, in the spectra of the reference materials from the FS XRS, the elements Si, K and Ca suffer from overlap from neighbouring lines (most particularly Si) but Ti is interference free. This is most clearly seen for Ca, the K_{α} line of which overlaps with K K_{β} . For the FS XRS, the simultaneous excitation by ^{55}Fe and ^{109}Cd means that Fe K_{α} overlaps with Mn K_{β} in spectra and

so the peak area must be inferred from Fe K_{β} . In the case of the PXRF, the Fe K_{α} peak does not have this overlap since its area is derived from the spectra using solely ^{109}Cd excitation. For the trace elements, Sr K_{β} overlaps with Zr K_{α} .

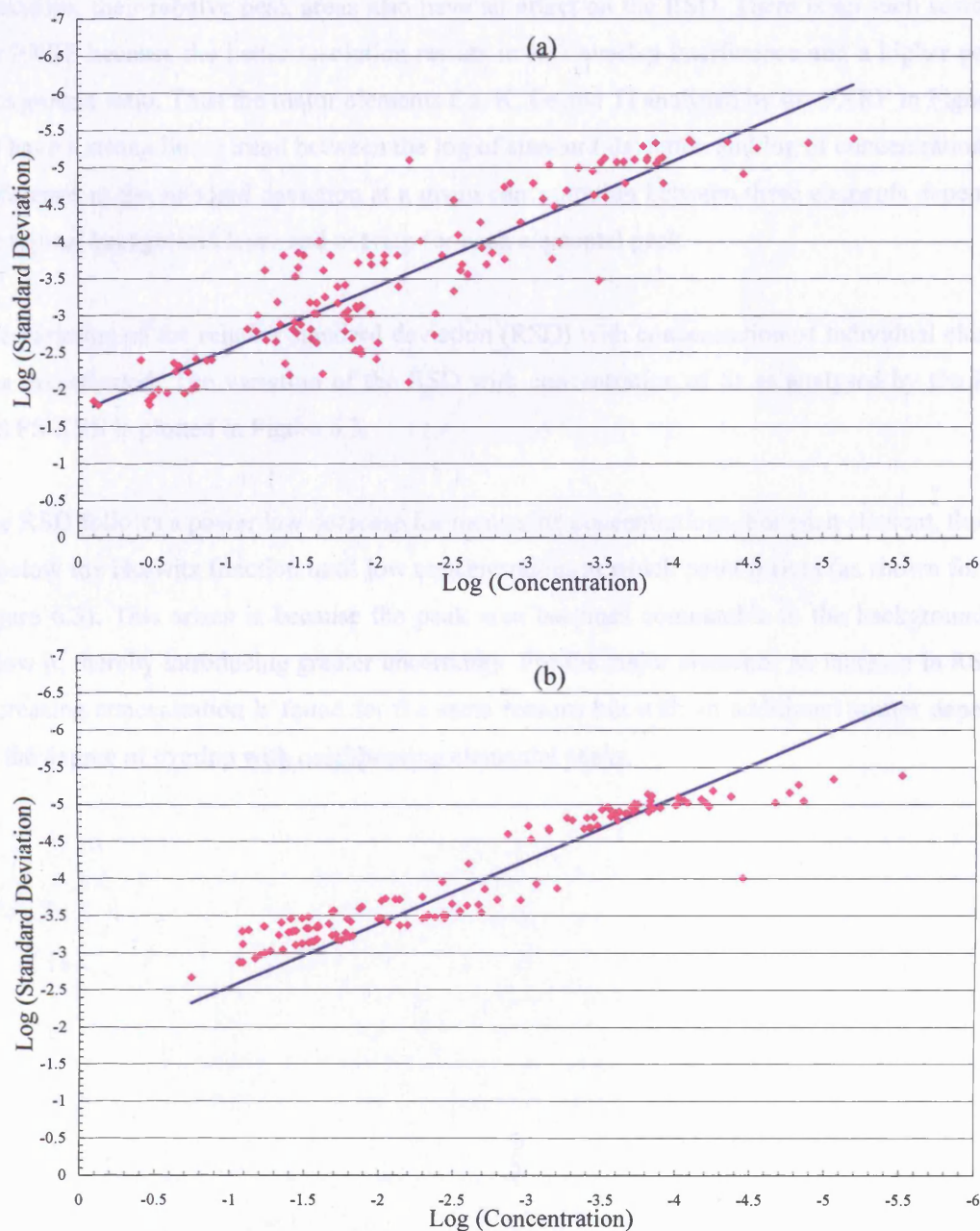


Figure 6.2 The log of standard deviation versus the log of concentration of elements in reference materials as estimated by the (a) FS XRS and (b) PXRF (purple diamonds). The Horwitz function (blue line) is plotted for comparison.

In addition to the general increase in RSD as the concentration decreases, there is also a scatter that is introduced that depends on the relative areas of overlapping peaks. In the FS XRS spectra of reference materials, the K line is generally less intense than the Ca line and the two overlap. Therefore, their relative peak areas also have an effect on the RSD. There is no such scatter for the PXRF because the better resolution results in less overlap interference and a higher peak to background ratio. Thus the major elements Ca, K, Fe and Ti analysed by the PXRF in Figure 6.2 (b) have a strong linear trend between the log of standard deviation and log of concentration. The difference in the standard deviation at a given concentration between these elements depends on the typical background level and overlap for each elemental peak.

The variation of the relative standard deviation (RSD) with concentration of individual elements was investigated. The variation of the RSD with concentration of Sr as analysed by the PXRF and FS XRS is plotted in Figure 6.3.

The RSD follows a power law decrease for increasing concentrations. For each element, the RSD is below the Horwitz function until low concentrations at which point it rises (as shown for Sr in Figure 6.3). This arises because the peak area becomes comparable to the background area below it, thereby introducing greater uncertainty. For the major elements, an increase in RSD for decreasing concentration is found for the same reasons but with an additional scatter depending on the degree of overlap with neighbouring elemental peaks.

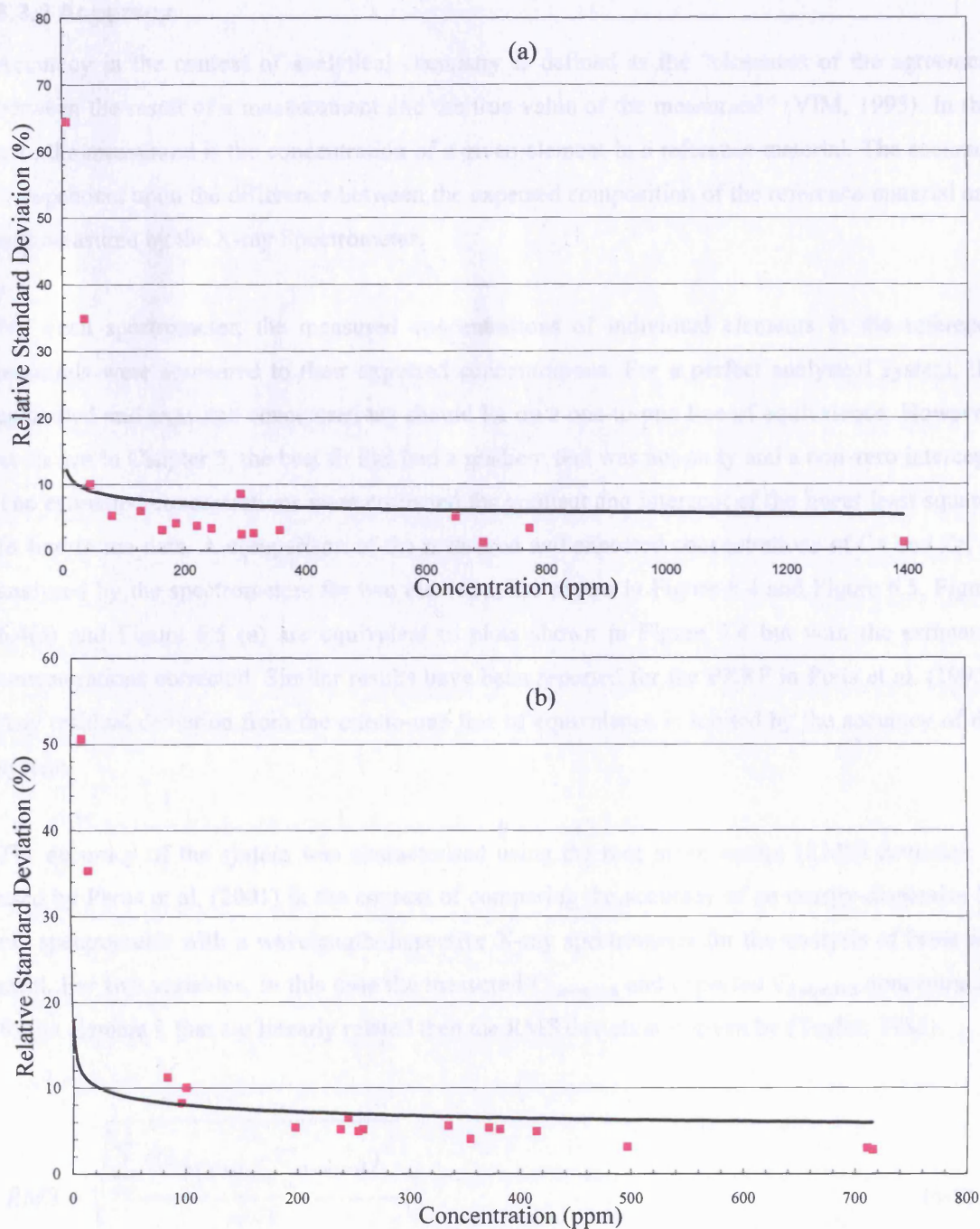


Figure 6.3 Variation of the relative standard deviation with concentration of Sr for (a) the XRS and (b) PXRf. The Horwitz function (black line) is plotted for comparison.

6.3.2 Accuracy

Accuracy in the context of analytical chemistry is defined as the “closeness of the agreement between the result of a measurement and the true value of the measurand” (VIM, 1995). In this case the measurand is the concentration of a given element in a reference material. The accuracy is dependent upon the difference between the expected composition of the reference material and that measured by the X-ray Spectrometer.

For each spectrometer, the measured concentrations of individual elements in the reference materials were compared to their expected concentrations. For a perfect analytical system, the estimated and expected concentrations should lie on a one-to-one line of equivalence. However, as shown in Chapter 5, the best fit line had a gradient that was not unity and a non-zero intercept. The estimated concentrations were corrected for gradient and intercept of the linear least squares fit line to the data. A comparison of the measured and expected concentrations of Ca and Zr, as analysed by the spectrometers for two elements, are shown in Figure 6.4 and Figure 6.5. Figure 6.4(a) and Figure 6.5 (a) are equivalent to plots shown in Figure 5.4 but with the estimated concentrations corrected. Similar results have been reported for the PXRf in Potts et al. (1995). Any residual deviation from the one-to-one line of equivalence is limited by the accuracy of the system.

The accuracy of the system was characterised using the root mean square (RMS) deviation as used by Parus et al. (2001) in the context of comparing the accuracy of an energy-dispersive X-ray spectrometer with a wavelength-dispersive X-ray spectrometer for the analysis of brass and steel. For two variables, in this case the measured $C_{i \text{ measured}}$ and expected $C_{i \text{ expected}}$ concentration for an element i , that are linearly related then the RMS deviation is given by (Taylor, 1982):

$$RMS = \sqrt{\frac{\sum_{m=1}^n (C_{i \text{ expected}} - C_{i \text{ measured}})^2}{n - 1}}, \quad (6-6)$$

where n is the total number of reference materials.

The analytical performance was also characterised using the global analytical uncertainty (E). This is the average relative difference between the measured and expected concentration of reference materials expressed as a fraction of the expected concentration. The global analytical

uncertainty, $E_{fractional}$, over a given concentration range for an analyte is given by (Rousseau, 2001):

$$(E)_{fractional} = \frac{\sum_{m=1}^n \left\{ \frac{\sqrt{(C_{i\ expected} - C_{i\ measured})^2}}{C_{i\ expected}} \right\}_m}{n}, \quad (6-7)$$

where m is a suffix for identifying each reference material. A perfect analytical system has zero deviation between the estimated and certified concentration and hence the value of E is zero.

Both measures of accuracy have advantages and disadvantages. For the RMS, the expression $(C_{i\ expected} - C_{i\ measured})^2$ in the numerator is more significant for larger concentrations compared to smaller concentrations. Therefore the RMS is not a representative measure of the accuracy over a large range of concentrations. The global analytical uncertainty is a measure of the average deviation relative to the expected concentration. The disadvantage is that for smaller sample sizes, a single large deviation (at any concentration) can skew the overall average value of E .

The RMS deviation and the global analytical uncertainty are presented in Table 6.2 and Table 6.3 for the XRS, PXRF and WD-XRF. The analytical performance of the MER APXS has been characterised in terms of its accuracy (Gellert et al., 2004) expressed as the relative standard deviation and is presented in Table 6.3 for information.

The accuracies for the major and trace elements generally improve from the FS XRS to the PXRF and WD XRF. As explained in Chapter 5, the limiting factor in the accuracy of the FS XRS is the application of the BFP algorithm for quantitative analysis. For some reference materials, the BFP algorithm can mis-estimate the concentration of a given element. This produces outliers from the general linear trend between the estimated and certified concentration. This effect is greater for elements present in larger concentrations (particularly Si). Both measures of accuracy are sensitive to the presence of these outliers. The PXRF uses a simpler fundamental parameter algorithm that benefits from (i) improved resolution for accurate peak fitting of elemental peaks, (ii) sequential excitation of the sample by the ^{55}Fe and ^{109}Cd as opposed to simultaneously with the FS XRS making the FP calculations simpler and (iii) a dark matrix correction based on the assumption that the majority of the dark matrix is composed of oxygen and silicon (both major

components of any silicate rock) rather than estimating it from the area of the Compton scattered Ag K_{α} peak. The matrix correction for the trace elements Rb, Sr, and Zr analysed by the WD XRF consists of the robust method of normalisation of elemental intensities to the Rh K_{α} Compton scattered X-ray lines (de Vries and Vrebos, 2002).

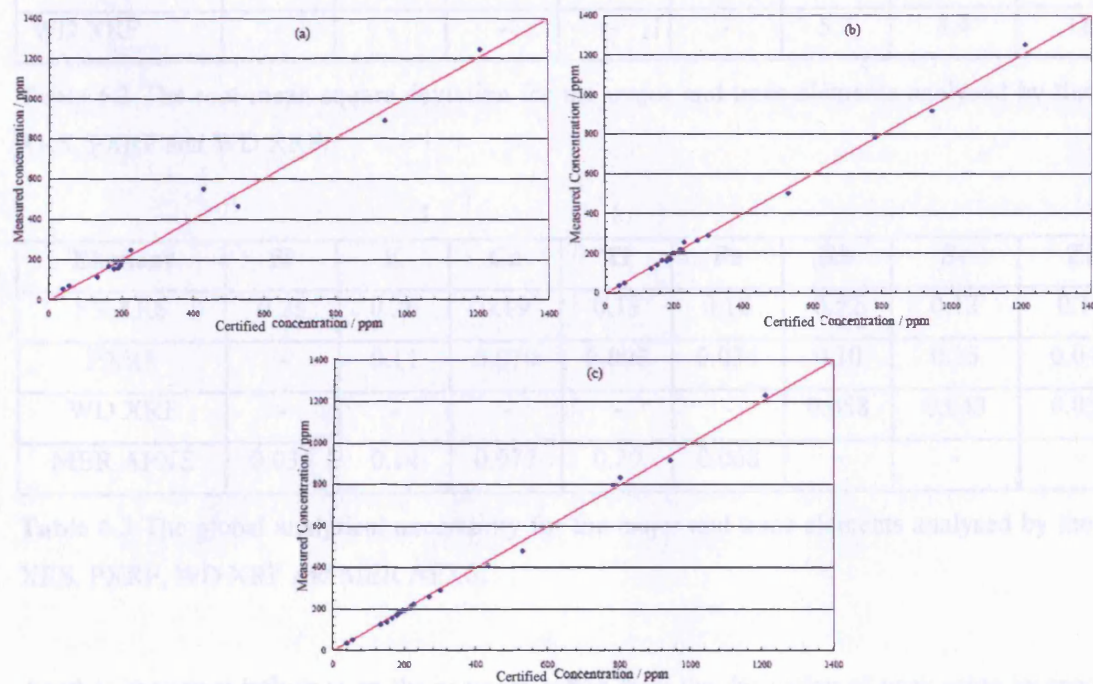


Figure 6.4 Plots of measured concentration of Zr in reference materials versus expected concentration as analysed by the (a) FS XRS, (b) PXRF and (c) WD XRF respectively. The pink line is a one-to-one line of equivalence.

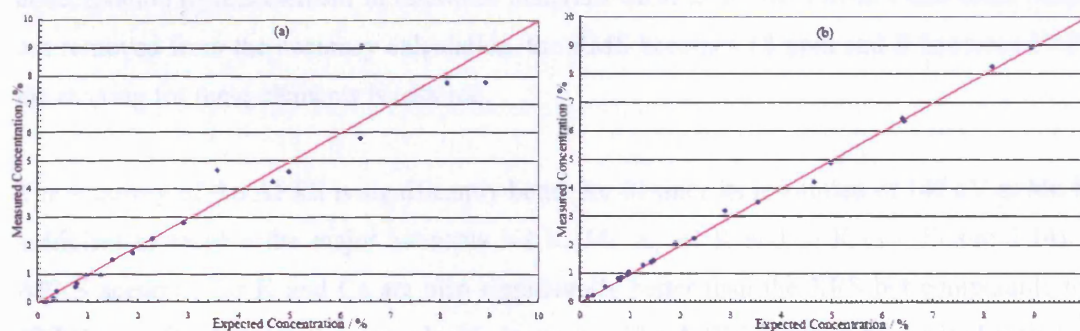


Figure 6.5 Plots of measured concentration of Ca in reference materials versus expected concentration as analysed by the (a) FS XRS and (b) PXRF respectively. The pink line is a one-to-one line of equivalence.

Element	Si (%)	K (%)	Ca (%)	Ti (%)	Fe (%)	Rb (ppm)	Sr (ppm)	Zr (ppm)
FS XRS	8.5	0.68	0.81	0.16	1.1	65	40	47
PXRF	-	0.13	0.14	0.045	0.15	13	34	21
WD XRF	-	-	-	-	-	5.7	8.4	18

Table 6.2 The root mean square deviation for the major and trace elements analysed by the FS XRS, PXRF and WD XRF.

Element	Si	K	Ca	Ti	Fe	Rb	Sr	Zr
FS XRS	0.25	0.26	0.19	0.13	0.18	0.52	0.13	0.14
PXRF	-	0.11	0.070	0.098	0.034	0.10	0.15	0.047
WD XRF	-	-	-	-	-	0.058	0.043	0.033
MER APXS	0.035	0.14	0.077	0.20	0.068	-	-	-

Table 6.3 The global analytical uncertainty for the major and trace elements analysed by the FS XRS, PXRF, WD XRF and MER APXS.

Another important influence on the accuracy arises from the derivation of peak areas by spectral fitting which is sensitive to the spectrometer resolution. The accuracy for the major and trace elements (with the exception of Sr) improves with improving resolution of the FS XRS, PXRF and WD XRF which are 391 eV, 260 eV and 50 eV at FWHM Mn K α respectively. The relatively large values of RMS and E for Sr for the PXRF is due to a large mis-estimation of the concentration of this element in reference materials SRM 2710 and PM-S. Once these materials are removed from the accuracy calculation, the RMS becomes 18 ppm and E becomes 0.12 and the ranking for these elements is restored.

The accuracy of the APXS is significantly better for Si since its resolution of 147 eV at Mn K α is sufficient to resolve the major elements Na K, Mg K, Al K and Si K (see Figure 2.14). The APXS accuracy for K and Ca are also significantly better than the XRS but comparable to the PXRF since Ca K and K K are resolvable in spectra. The APXS accuracy for Fe is slightly higher than the PXRF accuracy but comparable. The accuracy for Ti is higher than either the PXRF or the XRS. This arises because in the case of the APXS, X-ray fluorescence emission arises from bombardment of the sample by both alpha particles and Pu L X-rays (predominantly at 14.3 and

18.3 keV). The minimum of the X-ray production cross sections for both modes occurs at Ti K and so this element has the lowest sensitivity (counts per second per unit concentration) for all the elements analysable with the APXS (Brückner et al., 2003). In the case of the PXRF and XRS, primary excitation of Ti is from Mn K X-rays at ~6 keV (from the ⁵⁵Fe sources) and this is an efficient process because the energy of the X-rays are close to the Ti absorption edge.

6.3.3 Detection Limit

The limit of detection (LOD) is defined as the “smallest nett signal (or the derived concentration) that can be distinguished from the background signal at a specified confidence level” (IUPAC, 1978). The derivation of the detection limit is given in Potts (1987). For a given elemental peak superimposed on a background, the nett peak counts, N_p , is given by the following expression:

$$N_p = N_g - N_b, \quad (6-8)$$

where N_g is the gross (background plus peak) counts in the elemental peak region of interest for the analyte line and N_b are the corresponding background counts below the line.

The standard deviation of the counts in the peak, s_p , from Poisson statistics is:

$$s_p = \sqrt{s_g^2 + s_b^2} = \sqrt{N_g + N_b}, \quad (6-9)$$

where s_g is the standard deviation of the total gross counts and s_b is the standard deviation of the background counts.

At the detection limit the following condition applies:

$$N_g \approx N_b. \quad (6-10)$$

Therefore s_p becomes:

$$s_p = \sqrt{2N_b} . \quad (6-11)$$

An elemental peak in terms of area can be defined as significant if N_p is three standard deviations above N_b . Thus:

$$3s_p = 3\sqrt{2N_b} . \quad (6-12)$$

The background count rate, I_b (counts s^{-1}), is given by:

$$I_b = \frac{N_b}{t} , \quad (6-13)$$

where t is the integration time.

Equation 6-13 can be used to substitute for N_b in Equation 6-12 to obtain:

$$3s_p = 3\sqrt{2I_b t} . \quad (6-14)$$

In order to convert the detection limit from peak counts into concentration, Equation 6-14 is divided by the sensitivity S (counts per second per unit element %) and total measurement time t .

The sensitivity S is given by:

$$S = \frac{I_i}{C_i} . \quad (6-15)$$

The limit of detection in units of concentration is therefore:

$$LOD = \frac{3\sqrt{2}}{S} \sqrt{\frac{I_b}{t}} . \quad (6-16)$$

By substituting for t in Equation 6-16 using Equation 6-13 the following expression is obtained (Kump, 1997):

$$LOD = 3\sqrt{2} \frac{I_b}{S} \cdot \frac{\sqrt{N_b}}{N_b}. \quad (6-17)$$

Equation 6-17 was used by Kump et al. (2004) for the comparison of the capabilities of two energy-dispersive X-ray spectrometers using Si-PiN and Si(Li) detectors. This expression clearly demonstrates the parameters that influence the detection limit. These are:

- The ratio of the background and the signal count rates (I_b/S) or the signal to noise ratio (SNR), which is integration time independent.
- The factor 3 that defines the confidence level for the minimum intensity line above the background.
- The relative standard deviation of the background signal (RSDB) under the elemental line $\sqrt{N_B/N_B}$, which is integration time dependent. An elemental line superimposed on a background is more difficult to discern if the background is noisy, ie. if $\sqrt{N_B/N_B}$ is large. The RSDB depends on the total number of counts in the background. This relates to Equation 6-16 which implies that a longer integration time can result in improved detection limits since, as specified in Equation 6-17, the RSDB also reduces.

The limit of detection for the FS XRS was determined from the measurement of reference material GSP-1 for an integration time of three hours and calculated using Equation 6-16. The detection limits were determined in a similar way for the WD XRF (Ramsey et al., 1995) and the PXRF (Potts et al., 1995). The limit of detection for the X-ray spectrometers is given in Table 6.4.

For the major elements the detection limits of the XRS are generally better than that for the PXRF with the exception of Fe. For the trace elements, the detection limits rank WD XRF, PXRF and XRS. For the energy-dispersive systems, there is the well characterised general improvement in the detection limit for the major elements with increasing atomic number and then a sudden increase at Fe (Potts, 1987). This sudden increase arises because the energy of the absorption edges for Si, K, Ca and Ti are increasingly closer to the energy of the primary radiation from the ^{55}Fe sources and so are more efficiently excited. The sudden increase in the detection limit of Fe arises from the fact that primary excitation of this element is provided by the Ag K X-rays

emitted from the ^{109}Cd sources. The detection limits for Rb, Sr and Zr are significantly better than Fe since their absorption edges are closer to ^{109}Cd primary energy.

Element	Si ($\mu\text{g/g}$)	K ($\mu\text{g/g}$)	Ca ($\mu\text{g/g}$)	Ti ($\mu\text{g/g}$)	Fe ($\mu\text{g/g}$)	Rb ($\mu\text{g/g}$)	Sr ($\mu\text{g/g}$)	Zr ($\mu\text{g/g}$)
FS XRS	2600	110	75	33	590	22	27	26
PXRF	-	360	230	120	420	13	14	9
WD-XRF	-	-	-	-	-	1.3	1.4	1.2

Table 6.4 The limit of detection for the FS XRS, PXRF and WD XRF.

The source strength and measurement time influences the LOD since these variables determine the total number of counts in the spectra. The LOD is dependent upon the factor $\sqrt{N_b/N_s}$ (RSDB) from Equation 6-17 which is smaller for spectra with a higher number of counts in the background. The typical integration times for the X-ray spectrometers are set to obtain reasonable statistics in the spectra and depend upon their respective source strengths. The integration times were 70 s for the WD XRF, 100 s for the PXRF and 10800 s (3 hr) for the XRS. The source strength for the FS XRS was low because it was designed to acquire a spectrum over a Martian night (~12 hours). In contrast, the PXRF source strength is ~20 times stronger because it is designed for rapid acquisition of data in the field. The WD-XRF employs an X-ray tube with a small integration time for each element because its function is to rapidly analyse large numbers of samples in a geochemical research laboratory. Equation 6-17 shows that the detection limits can be contrived by careful choice of source strength and / or integration time to achieve a total number of counts in the spectrum and hence a certain RSDB. This is also implied by the conventional expression for LOD, Equation 6-16, which states that detection limits can be improved by arbitrarily increasing the integration time. However, the calculated detection limit remains a true reflection of the working detection limits of these X-ray spectrometers at the time of measurement.

The other factor that influences the LOD in Equation 6-17 is the peak to background ratio for fluorescent peaks of elements. As discussed in section 6.3.1, the resolution of a spectrometer influences the peak to background ratio. An increasing resolution between the spectrometers means that for a given elemental line there is a correspondingly higher background below the FWHM peak.

The difference in resolution and source strength explains the ranking WD XRF, PXRF and XRS for the LODs of the trace elements. The better LOD for the XRS than the PXRF for the major region is because of the lower detection efficiency (and hence sensitivity S) the PXRF has in that region that offsets its higher source strength. The PXRF is not capable of determining the concentration of elements with atomic number lower than ~ 19 (Potassium) owing to its low detection efficiency for fluorescent X-rays less than $\sim 3\text{keV}$. In contrast, the XRS is can detect X-rays down to $\sim 1\text{ keV}$ corresponding to Na K. For the trace elements, the improving resolution (and hence signal to noise ratio) of the XRS, PXRF and WD XRF explains the improving detection limits.

6.4 Conclusion

The analytical performance of the XRS, PXRF and WD XRF was based on the analysis of geochemical reference materials and the results were evaluated using three criteria: accuracy, detection limit and fitting precision. In order of improving accuracy, the X-ray spectrometers generally ranked XRS, PXRF and WD XRF based on results for various major and trace elements. The limiting factor in the performance of the XRS was the application of the BFP algorithm to correct for matrix effects and convert elemental intensities into concentrations. A secondary factor was a result of the improving resolution between these spectrometers, which allowed the peak areas to be fitted with increasing accuracy. The detection limits for the trace elements ranked in the same order. This was a result of increasing signal to noise ratio and decreasing relative standard deviation of the background. The fitting precision of the XRS and PXRF plotted as log relative standard deviation versus log concentration was complied with the Horwitz function over 4 orders of magnitude of concentration range from 10^{-1} to 10^{-5} g/g . The scatter about the Horwitz function for the PXRF was less than the XRS as a result of the better resolution and signal to noise for elemental peaks, meaning less uncertainty was introduced into the fitting parameters, and ultimately the peak areas, at the spectral fitting stage. The resolution of the spectrometers was a common factor that impacted upon their accuracy, detection limit and fitting precision and ultimately their analytical performance. A better resolution improves the peak to background ratio and the degree of overlap of neighboring peaks.

For the XRS, a significant contribution to the noise was from the pre-amplifier electronics as a result of the miniaturisation of the instrument. The limiting factor in the accuracy of the FS XRS was the application of the BFP method for its calibration. For some reference materials, this produced outliers in the bias plots which had an impact upon the RMS deviation. Methods to improve the performance of the BFP method are discussed in Chapter 5.

To improve the XRS LOD, the signal to noise ratio must be improved. A collimator can be employed in the detector to reduce or eliminate events occurring near the edge of the depleted region and thereby reduce shelving of the elemental peaks in spectra (discussed in Chapter 3). In addition, employing stronger sources that have a greater intensity can decrease the relative standard deviation of the background for a given integration time thereby improving the elemental detection limits.

The Beagle 2 FS XRS had several unique qualities compared to the two X-ray spectrometers against which its analytical performance was compared. It was robust enough to perform *in situ* field work on Mars. It was engineered to withstand the vibration encountered during launch and impulse during landing on Mars. It also underwent various tests to qualify its robustness including vibration and thermal vacuum tests (Sykes and Whitehead, 2000, 2003; Sykes 2003b). In order to be accommodated on the Beagle 2 lander, it successfully met many design constraints; the size and mass for the instrument was driven down because of the same constraints for the entire Beagle 2 lander. For comparison the mass of the FS XRS is 156 g compared to 6700 g for the PXRF. The FS XRS met its design constraints as a planetary instrument and provided a satisfactory analytical performance compared to other X-ray spectrometers optimised for other applications.

6.5 Summary

This chapter has described the analytical performance of the XRS and compared it to two other commercially available X-ray spectrometers. The analytical performance was found to be satisfactory in comparison and several ways in which the performance can be improved were identified. Chapter 7 will describe the use of the XRS for the analysis of field representative rocks, as opposed to reference materials. This chapter will investigate the operational performance of the XRS to achieve its two science objectives of (i) a geochemical analysis of rocks and soils and (ii) perform a K radiometric of the rocks by using the K content (as measured by the XRS) in conjunction with the ^{40}Ar content (as measured by a mass spectrometer).

Chapter 7

The Operational Performance of the X-ray Spectrometer

This chapter describes the operational performance of the Beagle 2 XRS in terms of its capability to achieve its scientific goals which are to perform (i) geochemical analyses and (ii) *in situ* radiometric date measurements of geological materials.

7.1 Introduction

The operational performance of the XRS was investigated by using the instrument to perform geochemical analyses and radiometric dating of several basalt samples. The geochemical analyses of the basalts were performed using the FS XRS and compared to complementary analyses made using other X-ray spectrometers, namely the PXRF and WD XRF, that were used in the assessment of analytical performance (Chapter 6). To perform $^{40}\text{K} \rightarrow ^{40}\text{Ar}$ radiometric dating for a given basalt, the Ar isotope content was measured using a laboratory version of the Beagle 2 Gas Analysis Package (Verchovsky, 2005).

7.2 Experimental Arrangement

A total of six fine-grained basalt samples in the form of rock slabs were used in the study (Figure 7.1, left). Measurement of the basalts using the FS XRS was performed with the DHA inside the calibration facility (described in Chapter 3, Section 3.4) at a pressure of 2.10^{-7} mbar (Figure 7.1, right) and connected to the BEE on the laboratory bench via a feedthrough. The DHA was mounted to the 'L' plate such that it was pointing vertically downwards and was cooled to ~ 250 K. Each basalt was mounted on a platform below the XRS and raised using four screws at each corner of the platform until the surface of the basalt was flush against the Al ring on the CFRP structure. The integration time for each measurement was 3 hours.

For the measurement by the PXRF, the basalt slabs were placed on top of the Spectrace 9000 probe aperture and primary excitation was performed by sequential illumination using ^{109}Cd for a 100 s live time and ^{55}Fe for a 60 s live time. The elements of interest for this study were the major elements (K, Ca, Ti) derived from primary excitation from ^{55}Fe and the trace elements (Fe, Sr, Zr) from ^{109}Cd . For measurement using the WD XRF, ~ 10 g of each slab was used to make a powder pellet (in an identical format as the geochemical reference materials). Primary excitation was performed using a Rhodium anode 3 kW end-window X-ray tube operated at 60 kV and 40 mA. The fluorescence K_{α} X-rays from the major elements were detected using a gas flow

proportional counter with a LiF(200) crystal monochromator (with the exception of Si K_{α} where a pentaerythritol crystal (PET) was used) with integration times of 15 - 30 s depending on the element. The spacing for each crystal sets the maximum X-ray wavelength it can diffract (according to Bragg's law) and so different crystals are used for different elemental X-ray lines. The fluorescent X-rays from elemental lines Rb $K_{\alpha 1}$, Sr $K_{\alpha 1}$ and Zr $K_{\alpha 1}$ were detected using a scintillation counter with a fine collimator using a LiF(200) crystal for an integration time of 70 s.



Figure 7.1 (Left) Basalt rock slab (Z1853.6) of age 179 million years as determined by $^{39}\text{Ar} \rightarrow ^{40}\text{Ar}$ radiometric dating. (Right) Experimental setup for measurement of a basalt slab in the calibration facility by the FS XRS.

7.3 Geochemical Composition of the Basalts

The calibration of the FS XRS and PXRF was based on the analysis of reference materials (Chapter 5). These reference materials consist of rocks that have been ground into a fine powder and compressed into powder pellets. The reference materials are ideal for analysis by the XRS because (as described in Chapter 5, Section 5.2) they are homogeneous, flat, of a thickness greater than the critical penetration depth of the radioisotope sources and of a diameter greater than the diameter of the XRS footprint (25 mm). Although the basalts are more representative of rocks in their natural state, their format is similar to reference materials since they are in the form of flat rock slabs, homogenous (since they are fine-grained) and of sufficient dimensions to satisfy the criteria for critical penetration depth and sampling footprint.

The concentration of the analysed elements in the basalts was estimated by the FS XRS and

PXRF and plotted against the corresponding WD XRF concentration. Figure 7.2 is a plot of the concentration of Ti as estimated by the FS XRS in reference materials (blue points) versus the certified concentration. There is a strong linear trend between the expected and certified concentration established for the reference materials. Also plotted are the estimated concentrations of Ti in the basalts by the FS XRS (purple points) versus the analysed concentration for the WD XRF. The Ti data for the basalts coincide with the best fit line established by the reference materials. For each analysed element in the set of basalts, the concentrations estimated by the FS XRS or PXRF versus the WD XRF concentration were approximately on the best fit line as defined by analysed concentrations of the same element in the reference materials.

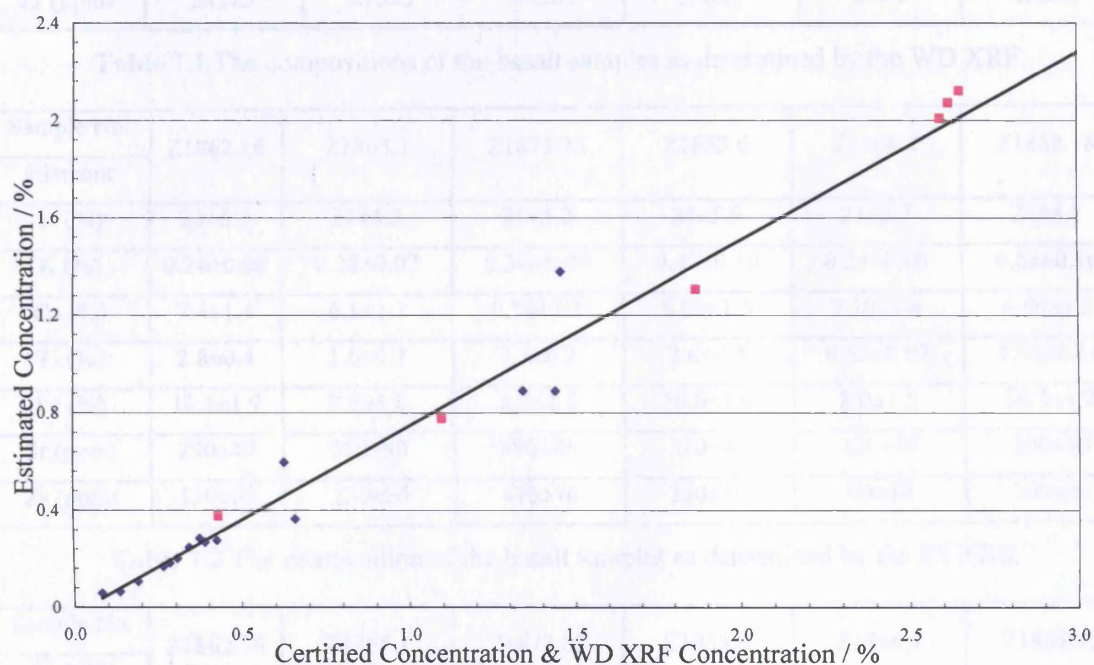


Figure 7.2 The estimated versus the certified concentration for Ti in reference materials (blue points) as analysed by the FS XRS. The black line is the least squares fit to the reference material data. For comparison, the estimated concentration of Ti in the basalts (purple points) versus the concentration analysed by the WD XRF is also plotted.

The estimated concentration of each element in the basalts were corrected using factors based on the gradient and intercept of the best fit line in the same way as the estimated concentration of each element in the reference materials. The final results for the geochemical analyses of the basalts analysed by the WD XRF, FS XRS and PXRF are shown in Table 7.1, Table 7.2, and

Table 7.3 respectively. The uncertainties are derived from the global analytical uncertainty calculated for the elements analysed by each spectrometer (Chapter 6).

Sample No.	Z1862.16	Z1865.1	Z1873.25	Z1853.6	Z1866.1	Z1868.18
Element						
Si (%)	22.6±0.1	21.5±0.1	22.5±0.1	22.6±0.1	23.5±0.1	24.8±0.1
K (%)	0.200±0.003	0.241±0.004	0.41±0.01	0.41±0.01	0.48±0.01	0.58±0.01
Ca (%)	7.6±0.2	6.3±0.1	6.5±0.1	7.9±0.2	6.9±0.2	6.4±0.1
Ti (%)	2.65±0.02	1.86±0.01	2.61±0.02	2.59±0.02	0.430±0.003	1.10±0.01
Fe (%)	10.27±0.05	9.90±0.05	9.02±0.05	9.98±0.05	7.95±0.04	9.45±0.05
Sr (ppm)	285±4	287±4	585±9	332±5	115±2	265±4
Zr (ppm)	351±5	215±3	445±7	336±5	83±1	158±2

Table 7.1 The compositions of the basalt samples as determined by the WD XRF.

Sample No.	Z1862.16	Z1865.1	Z1873.25	Z1853.6	Z1866.1	Z1868.18
Element						
Si (%)	23±5.7	21±5.2	21±5.2	24±5.9	23±5.7	24±6.1
K (%)	0.24±0.06	0.28±0.07	0.36±0.09	0.41±0.10	0.24±0.06	0.63±0.16
Ca (%)	7.4±1.4	6.1±1.2	6.10±1.1	8.00±1.5	7.20±1.4	6.80±1.3
Ti (%)	2.8±0.4	1.6±0.2	2.7±0.3	2.6±0.3	0.52±0.07	1.10±0.14
Fe (%)	10.1±1.9	9.7±1.8	8.5±1.6	10.0±1.9	8.0±1.5	10.3±1.9
Sr (ppm)	290±40	260±40	590±80	320±40	120±20	290±40
Zr (ppm)	330±50	220±30	470±70	320±50	90±10	160±20

Table 7.2 The composition of the basalt samples as determined by the FS XRS.

Sample No.	Z1862.16	Z1865.1	Z1873.25	Z1853.6	Z1866.1	Z1868.18
Element						
K (%)	0.19±0.02	0.26±0.03	0.44±0.05	0.45±0.05	0.33±0.04	0.57±0.06
Ca (%)	7.0±0.5	6.3±0.4	6.4±0.5	8.1±0.6	7.1±0.5	6.1±0.4
Ti (%)	2.7±0.3	1.7±0.2	2.8±0.3	2.6±0.3	0.47±0.05	0.97±0.1
Fe (%)	10.1±0.3	9.6±0.3	9.5±0.3	10.4±0.4	7.95±0.3	8.6±0.3
Sr (ppm)	280±40	290±40	597±90	320±50	120±20	270±40
Zr (ppm)	350±20	230±10	470±20	320±10	85±34	152±7

Table 7.3 The composition of the basalt samples as determined by the PXRF.

The elemental composition of the basalts as determined by the FS XRS and PXRF generally

agrees with that analysed by the WD XRF to within one standard deviation. The improved uncertainty on the concentrations for the PXRF as compared to the FS XRS was a result the better accuracy of the instrument. The estimated Si concentrations for the FS XRS are within 1.5 % of the concentration analysed by the WD XRF but the calculated uncertainty is higher (at ~6%). The calculated global analytical uncertainty for Si was weighted by several reference materials where the estimated concentration (via the Backscatter Fundamental Parameter method) differed greatly from the certified concentration. This arose because Si, out of all the analysed elements, is most sensitive to an inaccurate estimation of the dark matrix and so produces the largest systematic errors in its estimated concentration.

The measured K content by the WD XRF for Z1866.1 was higher than that measured using the FS XRS and PXRF whereas for the remaining basalts, the K content measured by these spectrometers agreed with the WD XRF results. The value of K as determined by the WD XRF was confirmed by repeat measurement. To investigate the K content of Z1866.1 further, four measurements across the surface of the slab using the PXRF were performed and the results are shown in Figure 7.3.

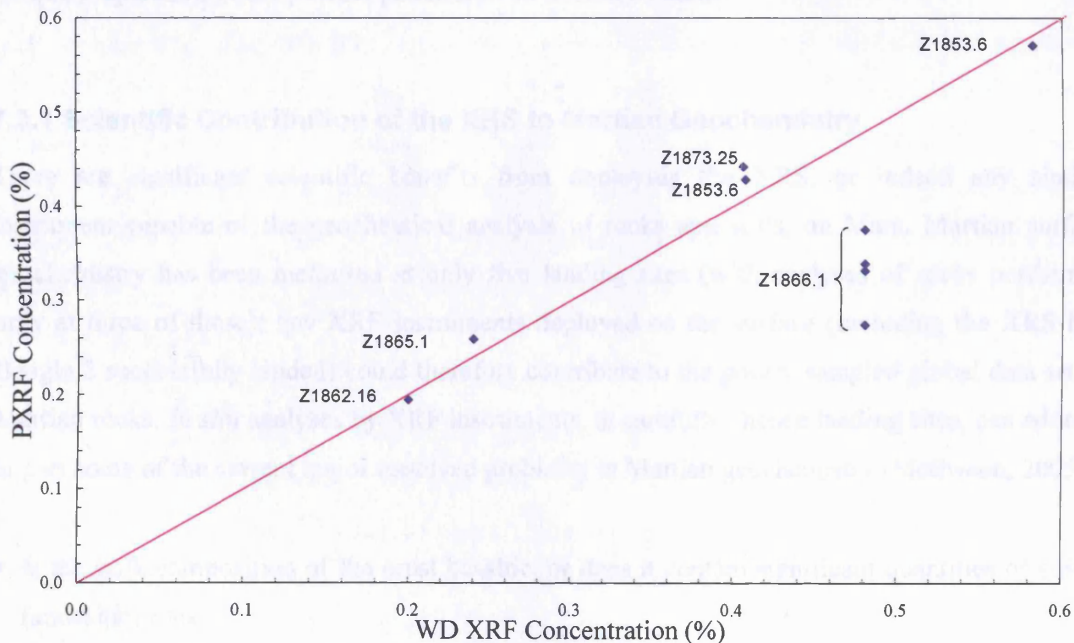


Figure 7.3 Estimated K content of basalt samples analysed by the PXRF versus the concentration estimated by the WD XRF. Four measurements were performed for Z1866.1, two on each surface of the basalt slab.

The PXRF K content agreed with the WD XRF measurement for all the basalts except Z1866.1 where there is a clear difference. There was a variation of 0.1 % K between the measurements made on the surface of the basalt slab (two on each side) with an average K content of 0.33 ± 0.04 %. This variation is larger than the PXRF relative precision for K at ~4% (Potts et al., 1995) meaning the variation is actually present in the sample rather than arising from the level of repeatability with the instrument. This disagreement in the K content between the spectrometers can be explained by the fact that the slab has an inhomogeneous distribution of K. The measurement of K with the PXRF and FS XRS was made on each basalt slab in its natural state and is an indication of the K content in the upper ~30 μm of the rock (Potts et al., 1997a) equivalent to the penetration depth of K K_{α} X-rays in silicate rocks. In contrast, the WD XRF does not perform a measurement on the rock slab but instead a portion of the rock was sampled to make a homogeneous pellet. Therefore, the WD XRF measurement was more representative of the bulk composition of the rock. Therefore, if the overall bulk K composition of the rock slab is higher than that analysed in the 30 μm thick slices measured by the energy-dispersive spectrometers, then the WD XRF measurement of K will be higher compared to the PXRF and XRS. Alternatively, the systematic error in the WD XRF concentration could result from the sample preparation of the powder pellet derived from the basalt.

7.3.1 Scientific Contribution of the XRS to Martian Geochemistry

There are significant scientific benefits from deploying the XRS, or indeed any similar instrument capable of the geochemical analysis of rocks and soils, on Mars. Martian surface geochemistry has been measured at only five landing sites (with analyses of rocks performed only at three of those); any XRF instruments deployed on the surface (including the XRS had Beagle 2 successfully landed) could therefore contribute to the poorly sampled global data set of Martian rocks. *In situ* analyses by XRF instruments, at carefully chosen landing sites, can address in part some of the current major unsolved problems in Martian geochemistry (McSween, 2005):

- Is the bulk composition of the crust basaltic, or does it contain significant quantities of silicic (andesitic) rocks?
- Have surface sediments experienced chemical weathering and, if so, what chemical changes resulted?
- What is the significance of differences in the compositions of relatively young Martian meteorites and the ancient crust?

- How well do Martian meteorites constrain the chemical and mineralogical composition and evolution of their mantle source regions?

Geochemical data from the XRS would have been used in conjunction with data from other instruments in the payload of Beagle 2 to establish the type of minerals and rocks at the landing area. Measurements of the geochemical composition of Martian rocks, from in situ measurements, and Martian meteorites have been used to establish a tentative geochemical classification of Martian volcanic rocks (McSween, 2002) using the $\text{Na}_2\text{O} + \text{K}_2\text{O}$ versus SiO_2 concentrations, although more data is required. XRF data can also contribute to an understanding of the history of the landing site. The APXS for the MER rovers found geochemical signatures, such as Br and Cl, which suggested that liquid water played a role in shaping the evolution of the landing site at some time in its history (Rieder et al., 2004; Gellert et al., 2004). The Beagle 2 landing site, Isidis Planitia, is a sedimentary basin (Bridges et al., 2003) and so the XRS could have made geochemical measurements of sedimentary rocks deposited by water.

Direct analyses of rocks at the surface can provide valuable ground truth to data from orbiter instruments that measure mineralogy, such as the Thermal Emission Spectrometer (TES) on Mars Global Surveyor and the Thermal Emission Spectrometer Imaging System (THEMIS). The inferred rock type using data from these instruments may be ambiguous. For example, Wyatt and McSween (2002) showed that TES was not able to discriminate between andesite and partially weathered basalt since their spectra are too similar. It was originally thought that the Martian surface was dominated by basaltic rocks (Mustard et al., 1997), especially the Southern highlands, but the Pathfinder APXS analyses showed that andesitic rocks existed at the landing site (Rieder et al., 1997b) leading to reconsideration of results from TES (Bandfield et al., 2000; Hamilton et al., 2001).

The value of geochemical measurements made by the XRS in particular (as opposed to the APXS) is that it could have made the first measurement of geochemically important trace elements Rb, Sr, Zr and Y in rocks, although these elements have been measured by the Viking XRFs in soils. However, unlike the APXS it could not have made measurements of carbon in rocks. With advances in the calibration of the XRS, using the recommendations outlined in Chapter 5, the range of elements that could be reliably determined by the instrument can be extended particularly with the major elements Na, Mg and Al.

The analytical performance of the instrument, assessed in Chapter 6, needs to be improved. An appropriate benchmark for the accuracy of the major and trace elements for the XRS is that set by the PXRf that is used for terrestrial geological fieldwork. It is important to improve the accuracy of all elements, particularly Si since it is a major component of silicate rocks. The accuracy of the XRS may pose difficulties in discriminating between different rock types from the interpretation of the geochemical data alone. The LOD for the XRS needs to be improved to the level of approximately 10 ppm for the trace elements for reliable geochemical interpretation. Most reference materials contained Rb, Sr and Zr at levels above the detection limit of the XRS. The Viking XRFS (Clark et al., 1976a) found that the Martian regolith contained Sr in concentrations 60 ± 30 ppm at Chryse Planitia and 100 ± 40 ppm at Utopia Planitia whereas Rb and Zr were present at levels at or near the detection limit of 30 ppm. These results illustrate the importance of a lower detection limit for the XRS to less than 10 ppm since if it had analysed the same regolith, the results would have been at or near the detection limit.

7.4 Radiometric ages of the Basalts

7.4.1 *In situ* $^{40}\text{K} \rightarrow ^{40}\text{Ar}$ Radiometric Dating on Mars Using Beagle 2

An important science aim of Beagle 2 was to perform the first *in situ* radiometric date measurement of Martian rocks (Wright et al. 2003). This was to have been performed using the $^{40}\text{K} \rightarrow ^{40}\text{Ar}$ technique with the XRS measuring the K concentration and the GAP measuring the Ar isotope content. In addition, a measurement of the Cosmic Ray Exposure (CRE) age was to have been attempted solely by GAP by measuring the neon isotopic composition (^{20}Ne , ^{21}Ne and ^{22}Ne). The CRE age is based on the analysis of isotopes that are produced by cosmic ray nuclear interactions with nuclei in rocks and accumulate over time (Doran et al., 2004; Eugster, 2003).

Radiometric dating is based on the decay of ^{40}K into ^{40}Ar , with a half life of $1.277 \cdot 10^9$ years, and uses the quantities of these isotopes in the rock to derive the age. The decay of ^{40}K is a branching decay, with either ^{40}Ar or ^{40}Ca possible (Figure 7.4). The major branch for decay into ^{40}Ar is through capture of an electron usually from the K shell to combine with a proton to form a neutron. This leaves the argon atom in an excited state and subsequent emission of a gamma-ray returns it to the ground state. The only branch of decay into ^{40}Ca is the emission of a beta particle from its nucleus and the conversion of a neutron into a proton.

The natural radioactive ^{40}K in a rock decays to ^{40}Ar which becomes trapped in the mineral lattice. This ^{40}Ar is only liberated if the mineral is melted, recrystallised or heated to a temperature that

will allow the ^{40}Ar to diffuse through the mineral lattice. When the rock is formed, the rock will not retain ^{40}Ar until it cools to a sufficient temperature and at this time the potassium-argon clock is 'set' (Dalrymple and Lanphere, 1969).

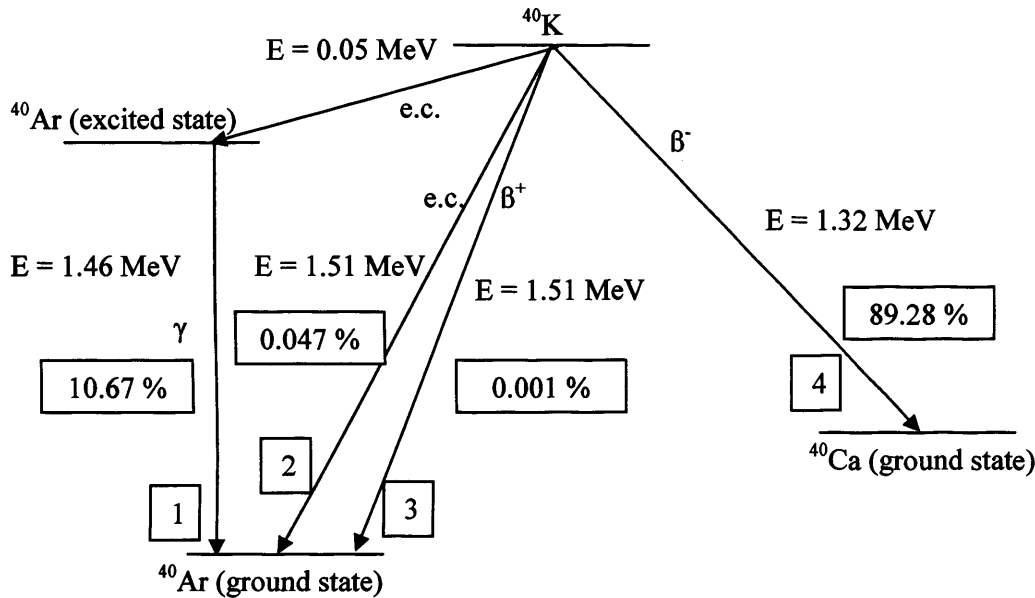


Figure 7.4 Decay scheme for ^{40}K . Four branches are shown which are (i) electron capture with emission of a gamma-ray, (ii) electron capture without gamma-ray emission, (iii) positron emission, (iv) beta emission. Also shown are the energy released and probability for each mode of decay (adapted from Dalrymple and Lanphere, 1969).

There are significant scientific returns to establishing an age for Martian geological materials for either *in situ* or returned samples. The importance of *in situ* dating on Mars has been emphasized by the Committee on Planetary and Lunar Exploration (COMPLEX, 2003): “COMPLEX recommends that studies of the feasibility of *in situ* determination of rock ages, by robotic spacecraft, be pursued”. To fully understand the geological history and origin of Mars it is crucial to establish the absolute ages of key stratigraphic geological units. Crater statistical techniques, together with stratigraphy, are the major tools by which relative chronologies of most planetary surfaces are derived (Tanaka et al., 1992). For Mars, crater density is used as a means of estimating relative chronology. For the Moon, the crater density is calibrated in absolute terms using dating of returned samples from the Apollo missions (Stöffler and Ryder, 2001). An absolute calibration of the cratering rate on Mars has been extrapolated from the Moon but this involves some uncertainty because of difficulties transferring the lunar crater production function

to Mars (Neukum et al., 2001). As a consequence, there are large uncertainties associated with the boundary age of Martian epochs. For example, the beginning of the Middle Amazonian has the largest uncertainty and is determined to have an absolute age between 1.4 – 2.1 Gyr (Hartmann and Neukum, 2001).

Several important geological targets on Mars for *in situ* radiometric dating have been described by Doran et al. (2004). The primary target is to perform a calibration of the Martian cratering rate. Since the relative stratigraphy and chronology is already established then the determination of the ages of certain samples at key sites means that the absolute chronology of Martian history could be constrained. An ideal target to achieve this would be igneous rocks at a site whose relative stratigraphy and geological context is well-known. Other suitable targets for $^{40}\text{K} \rightarrow ^{40}\text{Ar}$ dating include young volcanic lava flows or widespread ash deposits for example in the polar layered deposits. Also, hydrologic events could be dated if K-rich salts in sediments were present that precipitated from the waters in the associated fluvial and lacustrine events. The Beagle 2 landing site was Isidis Planitia which had extensive volcanism during the Hesperian epochs into the late Amazonian epochs and so any *in situ* dating would have further constrained the absolute chronology of these epochs (Bridges et al., 2003).

Several instruments have been proposed to perform an *in situ* radiometric date measurement on Mars. Swindle et al. (2003) are developing a system that consists of two instruments. K abundance is measured using the Laser-Induced Breakdown Spectroscopy (LIBS) technique, using an instrument developed at Los Alamos National Laboratory. The Ar isotope content is measured using a miniature Quadrupole Mass Spectrometry Array (QMSA), developed at the Jet Propulsion Laboratory.

The two instruments in the payload of Beagle 2 to perform radiometric dating, the XRS and the GAP, were situated on the PAW package on the end of the robotic arm and in the body of the lander respectively (Chapter 3). $^{40}\text{K} \rightarrow ^{40}\text{Ar}$ radiometric dating of rocks would have been a consequence of the general operational strategy called the rock analysis cycle (Pullan et al., 2004). After an initial survey using the Stereo Camera System (SCS), a target rock would be chosen. This rock would be intensively imaged by the SCS from various angles utilising the geological and stereoscopic filters. The Microscope and Spectrometers would then perform measurements on the weathered surface of the rock.

For radiometric dating to be effective, the Ar derived from the decay of ^{40}K must be retained in the rock. Weathering processes on the surface of the rock can alter the Ar content (Faure, 1977) and so a fresh interior portion of the rock is sampled instead. The Rock Corer-Grinder (RCG) on the PAW would have been used to grind away the exterior of a target rock to reveal a fresh surface. The teeth of the RCG would then acquire chippings from the rock and deliver them to the GAP via an inlet port for the Ar measurement. The prepared surface would then be analysed using the XRS to determine the K content. In addition, further measurements on the prepared surface using the Microscope and Mössbauer Spectrometer would also be made in order to compare the weathered surface of the rock to its interior.

To investigate the radiometric date measurement using versions of the XRS and GAP, the $^{40}\text{K} \rightarrow ^{40}\text{Ar}$ ages of the youngest and oldest basalts were measured. These $^{40}\text{K} \rightarrow ^{40}\text{Ar}$ ages were compared to complementary radiometric ages known via the ^{39}Ar - ^{40}Ar technique (Kelley, 2005).

7.4.2 Argon isotope content

The Ar isotope content was measured using a laboratory equivalent of the GAP, called Finesse, developed in-house at the Planetary and Space Sciences Research Institute, Open University (Verchovsky, 2005). It contains an extraction system and mass spectrometer similar to those utilised in the GAP for Beagle 2. A sample of mass approximately 4 mg (similar to sample mass acquired by the RCG) was extracted from the rock slabs and heated in the extraction furnace. The Ar was liberated from the sample by stepped heating from 300 to 1400 °C in 100 °C steps. Figure 7.5 is a histogram of the ^{40}Ar release for Z1853.6 at different temperatures.

For accurate radiometric dating, the ^{40}Ar used in the age calculations must be of solely radiogenic origin (ie derived from ^{40}K) and not from other sources. The only major additional component of ^{40}Ar is from the atmosphere which must be subtracted from the analysed total ^{40}Ar . The contamination arises from atmospheric gas adsorbed onto the surfaces of samples and equipment. To perform the correction for atmospheric ^{40}Ar , ^{36}Ar is used as a tracer since it is not produced through the decay of ^{40}K . The Earth value of $\{^{40}\text{Ar}/^{36}\text{Ar}\}_{\oplus} = 296$ (Faure, 1977) compared to 1700-1900 for Mars (Bogard and Garrison, 1999).

A correction for atmospheric ^{40}Ar was performed to derive the amount of radiogenic ^{40}Ar in the sample using the following equation:

$${}^{40}\text{Ar}^* = {}^{40}\text{Ar} \left(1 - \frac{\left\{ \frac{{}^{40}\text{Ar}}{{}^{36}\text{Ar}} \right\}_{\oplus}}{\frac{{}^{40}\text{Ar}}{{}^{36}\text{Ar}}} \right), \quad (7-1)$$

where ${}^{40}\text{Ar}^*$ is the radiogenic ${}^{40}\text{Ar}$ content, ${}^{40}\text{Ar}$ is the total measured ${}^{40}\text{Ar}$, $\left\{ \frac{{}^{40}\text{Ar}}{{}^{36}\text{Ar}} \right\}_{\oplus}$ is the ratio of natural Ar isotopes 40 and 36 in the Earth's atmosphere and $\left\{ \frac{{}^{40}\text{Ar}}{{}^{36}\text{Ar}} \right\}$ is the measured Ar isotope ratio.

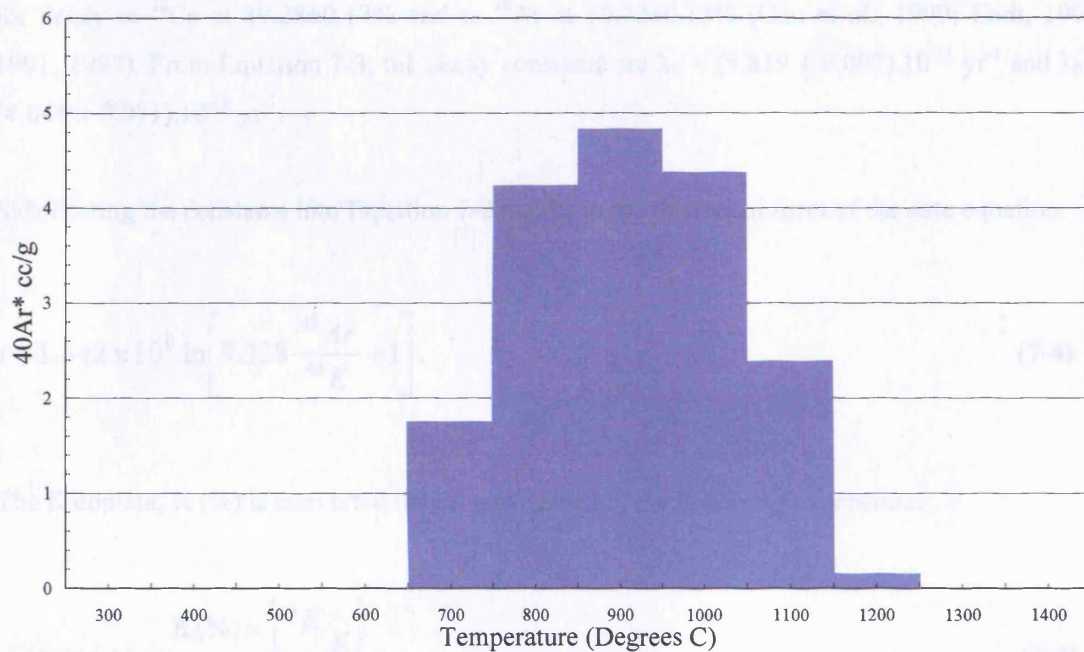


Figure 7.5 Radiogenic ${}^{40}\text{Ar}$ (symbolised by ${}^{40}\text{Ar}^*$) release by stepped heating from Z1853.6 (Verchovsky, 2005).

7.4.3 Radiometric ages

The ${}^{40}\text{K} \rightarrow {}^{40}\text{Ar}$ radiometric age t (years) is given by (Dalrymple and Lanphere, 1969):

$$t = \frac{1}{\lambda_K + \lambda_\beta} \ln \left[\frac{\lambda_K + \lambda_\beta}{\lambda_K} \frac{{}^{40}\text{Ar}^*}{{}^{40}\text{K}} + 1 \right], \quad (7-2)$$

where λ_K is the probability that an atom of ${}^{40}\text{K}$ will decay into ${}^{40}\text{Ar}$ per unit time (year^{-1}), λ_β is the

probability that an atom of ^{40}K will decay into ^{40}Ca per unit time (year^{-1}), $^{40}\text{Ar}^*$ is the number of atoms of radiogenic ^{40}Ar and ^{40}K is the number of atoms of ^{40}K .

The values of the decay constants for decay to ^{40}K and ^{40}Ca are derived from the equation:

$$\lambda_{K,\beta} = p_{K,\beta} \cdot \lambda, \quad (7-3)$$

where the total decay constant is $\lambda = (5.428) \cdot 10^{-10} \text{ yr}^{-1}$, p_β and p_K are the branching probabilities for decay to ^{40}Ca at $89.28 \pm 0.13\%$ and to ^{40}Ar at $10.72 \pm 0.13\%$ (Chu et al., 1999; Endt, 1990, 1991, 1993). From Equation 7-3, the decay constants are $\lambda_K = (5.819 \pm 0.007) \cdot 10^{-11} \text{ yr}^{-1}$ and $\lambda_\beta = (4.846 \pm 0.071) \cdot 10^{-10} \text{ yr}^{-1}$.

Substituting the constants into Equation 7-2 results in the numerical form of the date equation:

$$t = 1.842 \times 10^9 \ln \left[9.328 \frac{^{40}\text{Ar}}{^{40}\text{K}} + 1 \right]. \quad (7-4)$$

The K content, K (%) is converted into K (mol/g) using the following expression:

$$K(\text{mol/g}) = \frac{K(\%) \times \left\{ \frac{^{40}\text{K}}{\text{K}} \right\}}{100 \times A}, \quad (7-5)$$

where A is the atomic weight of K (39.1 g/mol) and $\{^{40}\text{K}/\text{K}\}$ is the natural isotopic abundance of ^{40}K which is 0.0117 (Faure, 1977).

^{40}Ar in units of cc/g is converted into units of mol/g by multiplying the by the constant $4.462 \times 10^{-5} \text{ mol/cc STP}$ (Lide, 1992) derived from the ideal gas equation.

The uncertainty on the age can be derived by first expressing Equation 7-4 in the following way:

$$t = A \ln[x], \quad (7-6)$$

where:

$$x = B \frac{{}^{40}\text{Ar}}{{}^{40}\text{K}} + 1, \quad (7-7)$$

where $A = 1.842 \cdot 10^9$ yr and $B = 9.328$ are constants derived from the decay constants and are in the numerical form of the radiometric age Equation 7-4. The uncertainties on the values of the decay constants have a negligible effect on the uncertainty on the age, $\sigma(t)$ (Dalrymple and Lanphere, 1969) and in practice, the $\sigma(t)$ is limited by the uncertainty on the measured quantities of ${}^{40}\text{Ar}$ and ${}^{40}\text{K}$.

The uncertainty in x , $\sigma(x)$, is given by:

$$\sigma(x) = B \frac{{}^{40}\text{Ar}}{{}^{40}\text{K}} \sqrt{\left(\frac{\sigma({}^{40}\text{Ar})}{{}^{40}\text{Ar}}\right)^2 + \left(\frac{\sigma({}^{40}\text{K})}{{}^{40}\text{K}}\right)^2}. \quad (7-8)$$

This can then be used to derive the error in t , $\sigma(t)$:

$$\sigma(t) = t \cdot \frac{\sigma\{\ln(x)\}}{\ln(x)}, \quad (7-9)$$

where:

$$\sigma\{\ln(x)\} = \frac{\sigma(x)}{x}. \quad (7-10)$$

Table 7.4 contains the results used to derive the radiometric ages for the basalt samples and consist of the K content as measured by the FS XRS, PXRF and WD XRF, the ${}^{40}\text{Ar}$ isotope content as measured by the Finesse mass spectrometer and the radiometric ages as determined by the ${}^{39}\text{Ar}$ - ${}^{40}\text{Ar}$ and ${}^{40}\text{K} \rightarrow {}^{40}\text{Ar}$ techniques. The radiometric age of the youngest and oldest basalts

were used.

Sample Identity	K Content (%)			Radiogenic ^{40}Ar Isotope Content (cc/g)	Radiometric Ages	
	FS XRS	PXRF	WD XRF		^{39}Ar - ^{40}Ar (Ma)	^{40}K → ^{40}Ar (Ma)
Z1853.6	0.41±0.10	0.45±0.05	0.41±0.01	$(1.79\pm0.18)\cdot 10^{-6}$	179±3	FS XRS: 110±30 PXRF: 99±14 WD XRF: 109±11
Z1866.1	0.24±0.06	0.33±0.04*	0.48±0.01	$(2.47\pm0.25)\cdot 10^{-5}$	1141±23	FS XRS: 1600±300 PXRF: 1300±150 WD XRF: 1000±80

Table 7.4 Collated results for the radiometric date measurement of Z1853.6 and Z1866.1. It contains K content as measured by an FS XRS, PXRF and WD XRF, ^{40}Ar content corrected for atmospheric contamination as measured by a flight-like version of the GAP and radiometric ages derived using the Ar-Ar and ^{40}K → ^{40}Ar techniques. A ^{40}K → ^{40}Ar ages is reported corresponding to the K measurement made by each spectrometer.

7.4.4 Discussion

The ^{40}K → ^{40}Ar age for Z1866.1 as derived from the K measurement by the FS XRS is older than its Ar-Ar age. In contrast, the ^{40}K → ^{40}Ar age derived from the K measurements by the WD XRF and PXRF approximately agrees with the Ar-Ar age. As discussed in Section 7.3, the K determination by the WD XRF was more representative of the bulk K content of the rock since it uses a homogeneous pellet derived from the basalt slab. In contrast, the K analysis determined by the FS XRS and PXRF is representative of the K at the surface to a depth of 10s of micrometres whereas the rock has elevated levels of K in its interior. However, the measurement of K by the PXRF is the average of four repeat measurements across the surface of the basalt, which makes it more representative of the bulk K composition of the rock as compared to the single XRS measurement (Potts, 1997a).

A younger ^{40}K → ^{40}Ar age for Z1853.6 can be attributed to argon loss. Faure (1977) lists several reasons for argon loss. Geological processes that elevate the temperature of the rock sufficiently high can cause some of the radiogenic Ar to be released. In addition, chemical weathering and alteration by aqueous fluids can lead to argon loss. Finally, argon loss can occur during the grinding of the rock into a powder for analysis with the mass spectrometer.

The $^{40}\text{K}\rightarrow^{40}\text{Ar}$ ages of the Martian meteorites all generally agree with the Ar-Ar age with the exception of ALH84001 where an impact resetting event probably occurred at ~4 Ga ago (Doran et al., 2004). Swindle (2001) found that the $^{40}\text{K}\rightarrow^{40}\text{Ar}$ technique can be used to determine the age of Martian meteorites in the laboratory to an accuracy of ~20%. The level of uncertainty with the age determination of the basalts was ~25% for Z1853.6 and ~13% for Z1866.1. The limiting error on the age depends on the errors on the measurements of Ar and K by the XRS and GAP respectively and improvements in the analytical performance of these instruments can produce a higher precision age determination.

In the context of performing the radiometric date measurement *in situ* on Mars there are several considerations for the K and Ar measurement. The K measurement by the XRS is subject to several field effects. Firstly, surface roughness may alter the relative X-ray fluorescence intensities from various elements. A correction for the effect of surface roughness for the *in situ* analysis of rocks by a field portable X-ray spectrometer has been developed by Potts et al. (1997b). However, ideally a sample preparation tool could be utilised to make the surface flat. While Beagle 2 was equipped with the RCG, a similar tool was installed on the NASA Mars Exploration Rovers Spirit and Opportunity called the Rock Abrasion Tool which was capable of making a 'crater' of dimensions 45 mm in diameter and depth of 5 mm on the rock (Gorevan et al., 2003). Another effect is sample inhomogeneity from the natural mineralogy which may produce a variation of the K content (Potts et al., 1997a). This can be solved using multiple measurements on the sample to determine an average composition. Finally, rocks may have a weathered coating such that the geochemical composition of the exterior differs from the interior (Potts et al., 2006). This can again be addressed by use of a sample preparation tool to remove the weathered surface.

To perform an accurate measurement of the radiogenic Ar *in situ* on Mars, the sources of non-radiogenic Ar and methods of argon loss must be taken into account (as considered by Swindle, 2001). Argon loss occurs by heating in the rocks' history to a temperature high enough to liberate the Ar and this is a common mechanism for Earth rocks (Faure, 1977). When a rock is heated to such a high temperature it undergoes metamorphism where its physical and/or chemical properties change. Swindle (2001) maintains that few rocks on Mars will have experienced metamorphism and so argon loss by this method is unlikely. The conditions for metamorphism arise from (i) plate tectonics and (ii) the intrusion of magma into a body of solid rock. However, given the occurrence of volcanism on Mars up to two million years ago (Neukum et al., 2004)

and possibly plate tectonics in early Mars history (Van Thienen et al, 2004) it is apparent that metamorphic rocks do occur on Mars. Impact heating is another mechanism for argon loss but the process only heats a small fraction of rocks to a sufficient temperature. For Mars the main sources of non-radiogenic ^{40}Ar are mainly from the atmosphere and in magma. For terrestrial rocks, any ^{36}Ar present is assumed to originate from the Earth's atmosphere and accompany ^{40}Ar in the ratio 296. On Mars, this ratio is not well characterised and is in the range 1700 – 1900 (Bogard and Garrison, 1999). There is an additional component of ^{40}Ar in the magma with an $^{40}\text{Ar} / ^{36}\text{Ar}$ ratio of 200 – 400 (Bogard and Garrison, 1999). A further complication is that where all ^{36}Ar in Earth rocks can be assumed to come from the atmosphere, in the case of Mars it can also be produced by high-energy cosmic ray interaction with the regolith. However, another Ar isotope ^{38}Ar is produced by cosmic rays and the ratio $^{38}\text{Ar} / ^{36}\text{Ar}$ is expected to be present in a fixed ratio and so the cosmogenic ^{36}Ar can be derived.

7.5 Conclusion

The scientific importance of performing *in situ* measurements of the geochemistry of Martian rocks and soils has been discussed. The Beagle 2 XRS, in its current state of calibration, was capable of achieving its scientific aims in that it could perform a geochemical analysis of a range of elements, in particular potassium to contribute to the radiometric date measurement. The instrument performance would have been improved by following the recommendations in Chapter 5 to improve spectral fitting and the quantitative analysis methods, similar to as occurred after recalibration of the Pathfinder APXS (Brückner et al., 2003; Foley et al., 2003a). Furthermore, the analytical performance of the XRS has been fully characterised, yielding important parameters such as instrument accuracy and detection limits, which are required to reliably interpret raw data from the instrument.

The geochemical composition of the set of basalts as determined by the FS XRS was found to generally agree to within one standard deviation with complementary analyses performed with the PXRf and WD XRF. In terms of the operational performance of the XRS, the instrument was able to perform a geochemical analysis for several major and trace elements in basalts. However, improvements in the design of the XRS and the implementation of its calibration (discussed in Chapters 5 and 6) can improve its analytical performance. The $^{40}\text{K} \rightarrow ^{40}\text{Ar}$ radiometric dating is more challenging because (i) the analysed K content may not be representative of the whole rock and (ii) the rock may have experienced radiogenic ^{40}Ar loss and also acquired non-radiogenic ^{40}Ar from various sources.

The use of *in situ* $^{40}\text{K}\rightarrow^{40}\text{Ar}$ dating in the context of Mars exploration has the potential to establish the absolute chronology of Mars. If radiometric dating were performed using several lander or rover missions at sites where the cratering stratigraphy was well established then the relative age of geological units on Mars can be tied into an absolute chronology and major events could be timed (COMPLEX, 2003). An *in situ* radiometric date determination could potentially complement the rock ages from returned samples derived with a greater precision. The terrestrial radiometric dating technique is best applied using multiple techniques and on multiple samples for which the geological context is well characterised and this philosophy applies equally to Mars (Doran et al., 2004; Meyer et al., 1996).

7.6 Summary

This chapter has investigated the operational performance of the FS XRS. The FS XRS analysed the geochemical composition of a suite of basalts and the results were generally in agreement to within one standard deviation with analyses using the PXRF and WD XRF. This chapter also demonstrated radiometric dating of two basalt samples using versions of the Beagle 2 XRS and GAP. The radiometric dating was performed using the $^{40}\text{K}\rightarrow^{40}\text{Ar}$ technique where the K was measured by the XRS and the Ar isotope content measured by a laboratory equivalent of the GAP. The ages of the samples were already dated using the Ar-Ar technique with the oldest (Z1866.1) and youngest (Z1853.6) samples dated at 1141 ± 23 Ma and 179 ± 3 Ma respectively. The $^{40}\text{K}\rightarrow^{40}\text{Ar}$ ages for the sample Z1866.1 at 1600 ± 300 Ma was older than the Ar-Ar age because the K measurement was not representative of the whole rock. The $^{40}\text{K}\rightarrow^{40}\text{Ar}$ age for Z1853.6 at 110 ± 30 Ma was less than the corresponding Ar-Ar age due to argon loss by some mechanism.

Chapter 8

Conclusions

This chapter briefly summarises the main conclusions of the thesis and outlines some future research aims. These conclusions come from an assessment of the Beagle 2 X-ray Spectrometer in four areas: characterisation (Chapter 4), calibration (Chapter 5), analytical performance (Chapter 6) and operational performance (Chapter 7).

The characterisation (Chapter 4) of the XRS was investigated prior to its calibration. The XRS was found to have an energy resolution of ~ 390 eV at Mn K_{α} and a gain of ~ 6.4 eV/Ch. Spectral artefacts were identified, some of which arose from fluorescence of the instrument and backscatter of X-rays from the sources, in order to distinguish them from the characteristic elemental lines arising from X-ray fluorescence of the sample. The main components of the instrument detection efficiency were modelled and compared to measurements. The detection efficiency at low energies (< 3 keV) was found to be dependent upon the X-ray transmission of the Be window but the transmission of the gold contacts, parylene and nitrogen were also major contributors. At higher energies (> 5 keV) the detection efficiency was dominated by the absorption in the Si-PiN diode depleted region. The system deadtime was investigated and a major contributor to it (the Multi Channel Analyser) was eliminated for the calibration work. The gain of the XRS was found to be weakly dependent upon the temperature of the Detector Head Assembly but was more sensitive to the temperature of the Back End Electronics. The gain was found to change by 20 % when the BEE temperature was increased from -10°C to $+50^{\circ}\text{C}$. Although important for operations on Mars, the gain variation with temperature did not impact upon the calibration of the XRS since the temperature of the BEE could be maintained at a stable temperature in the laboratory.

The XRS underwent a quantitative calibration (Chapter 5) to enable conversion of raw X-ray pulse height data from the measurement of a geological sample into geochemical concentrations. The calibration was split into (i) energy calibration followed by a qualitative evaluation of the spectrum to identify characteristic X-ray lines from elements in the sample, (ii) fitting of spectral peaks and background to extract X-ray fluorescence intensities and (iii) conversion of these intensities into elemental concentrations using the Backscatter Fundamental Parameter (BFP) method. Spectral fitting of several major and trace elements in the spectra of reference materials was performed. The spectral fitting was challenging for some elements owing to the spectral

resolution of the XRS which caused significant peak overlap at all energies. To improve the accurate derivation of elemental intensities, more specialised peak fitting functions or experimentally derived peak shapes can be employed (Ellis, 2002; Campbell and Wang, 1991; Campbell et al., 1997; Lepy et al., 1997). The BFP method was implemented after experimentally determining several instrument parameters such as the average incidence angle of the primary radiation and average exit angle of the fluorescent radiation. The estimated versus certified concentration of reference materials for the calibrated elements showed a general linear relationship. The performance of the BFP method is sensitive to accurate fitting of the Compton scattered Ag K_{α} peak.

The analytical performance of the XRS was assessed (Chapter 6) and compared to two spectrometers (i) a terrestrial portable X-ray fluorescence (PXRF) instrument and (ii) a conventional laboratory wavelength-dispersive X-ray fluorescence instrument (WD XRF) of the type widely used in geochemical research laboratories. In order of improving accuracy, the spectrometers generally ranked XRS, PXRF and WD XRF. The detection limits ranked in the same order for the trace elements. The fitting precision of the XRS and PXRF were plotted as log relative standard deviation versus log concentration was benchmarked against the Horwitz function over 4 orders of magnitude of concentration.

Several areas where the performance of the XRS could be improved were identified following the study of operational performance. The resolution of the XRS was an important characteristic of the spectrometers that impacted upon their accuracy, detection limit and fitting precision. An improving resolution between the XRS, PXRF and WD XRF (~390 eV, ~260 eV and ~50 eV at 5.9 keV respectively) meant there was less overlap between neighbouring lines and a lower background relative to the peak area (Potts, 1987). The accuracy of the XRS was limited by incorrectly estimated concentrations of some elements by the BFP algorithm in a few reference materials arising from inaccurate fitting of the Compton scattered Ag K_{α} peak. The XRS limit of detection can be improved by increasing the peak area to background ratio.

The operational performance of the XRS was investigated (Chapter 7) when the XRS was used to analyse a set of basalt rock slabs. The concentration of each element as analysed by the XRS was found to generally agree with complementary analyses by the PXRF and WD XRF to within one standard deviation. The K concentration of the oldest and youngest basalts was used in conjunction with their ^{40}Ar content, measured by a laboratory version of the Gas Analysis

Package (Wright et al., 2003), to perform a $^{40}\text{K}\rightarrow^{40}\text{Ar}$ radiometric date measurement. The uncertainty on the age determination was dependent upon the uncertainty associated with the K measurement (by the XRS) and the ^{40}Ar measurement (by the GAP). The $^{40}\text{K}\rightarrow^{40}\text{Ar}$ age for Z1866.1 at 1600 ± 300 Ma, as derived from the K measurement by the XRS, was older than its Ar-Ar age at 1141 ± 23 . This was due to the analysed K being not representative of the higher bulk K content of the rock. The younger $^{40}\text{K}\rightarrow^{40}\text{Ar}$ age for Z1853.6, at 110 ± 30 Ma, than the Ar-Ar age at 179 ± 3 Ma can be attributed to argon loss. An accurate measurement of the age of a rock using the $^{40}\text{K}\rightarrow^{40}\text{Ar}$ method of radiometric dating is challenging because (i) the analysed K content may not be representative of the whole rock and (ii) the rock may have lost radiogenic ^{40}Ar and / or acquired non-radiogenic ^{40}Ar from various sources, particularly the atmosphere. This study emphasised the importance of performing the radiometric date measurement using multiple techniques and on multiple samples for which the geological context is well characterised.

The Beagle 2 XRS has undergone four studies (characterisation, calibration, analytical performance, operational performance) to characterise the instrument for the geochemical analysis of rocks and soils on the surface of Mars. Any future work with the instrument will aim to improve its analytical and operational performance. The resolution can be improved by use of lower noise pre-amplifier electronics and / or use of a lower noise detector. For example, in the case of the APXS, the resolution was improved from ~ 260 eV at Fe K_{α} (Rieder et al., 1997a) with the Pathfinder APXS to ~ 160 eV at Mn K_{α} (Rieder et al., 2003) with the MER APXS because of a redesign of the electronics and switching from use of an Amptek Si-PiN diode to a Ketek silicon drift detector (Lechner et al., 2004). In addition, the new generation Amptek Si-PiN diodes (Redus et al., 2001) are now reported to have a resolution of ~ 149 eV at Mn K_{α} .

The effect of a collimator fitted in front of the detector on the peak to background ratio and hence detection limits can be investigated. A collimator on the detector can reduce or eliminate events that occur near the edge of the depleted region of the detector (Potts, 1987) thereby reducing shelving on the low energy side of spectral peaks that contribute to the background (Karydas et al., 2003). In addition, employing stronger sources can decrease the relative standard deviation of the background for a given integration time and improve detection limits.

Improved fitting models of both elemental lines (Ellis, 2002 and references therein) and the Compton scattered Ag K lines (Van Gysel et al., 2003) can be implemented to improve the quantitative calibration of the XRS. To complement the quantitative calibration work, a Monte

Carlo model of the instrument, similar to that used by Omand et al. (2005) for the MER APXS, can be developed to compare the predicted and measured X-ray yields of elements in reference materials. Further characterisation of $^{40}\text{K} \rightarrow ^{40}\text{Ar}$ radiometric dating using robotic landers can be performed (COMPLEX, 2003). In addition, the effect of surface roughness of rocks (on the mm scale) on elemental X-ray fluorescence intensities can be investigated. In particular, the correction for surface roughness, as developed by Potts et al., 1997b, that consists of normalisation of the elemental X-ray intensity to the ^{55}Fe scatter peak is limited by the scatter of the ^{55}Fe X-rays from the air gaps between the sample and detector. The effectiveness of this correction could be investigated under vacuum since this will have applicability to *in situ* analysis of rocks on Mars with an atmospheric pressure that is effectively a vacuum.

There is a significant scientific value in making *in situ* geochemical measurements of Martian rocks and soils and instruments that can deliver this kind of data should be included in the payloads of all future missions. X-ray fluorescence spectrometers are ideal instruments with which to perform these measurements and they can be engineered to meet the stringent requirements for planetary missions. A new version of the APXS is under development for the Mars Science Laboratory (MSL) due for launch in 2009 (Vasavada, 2006). As for future contributions of these instruments, the basic principles of their operation mean that the range of analysable elements, although large, cannot change significantly. The analytical performance of X-ray fluorescence spectrometers is limited in part by their resolution. The current resolution of the MER APXS (~ 160 eV at Mn K_{α}) is sufficient to separate the fluorescence lines of interest (see for example Figure 2.14). Any further increases in resolution, to approach the intrinsic detector resolution of ~ 140 eV at Mn K_{α} , will not significantly impact upon its performance and will be limited instead by the quantitative analysis method employed. The next generation of robotic rovers (such as ExoMars and MSL) have other instruments that can also perform measurements of geochemistry and offer several complementary features compared to X-ray fluorescence spectrometers. The remote Laser Induced Breakdown Spectrometer (baselined for ExoMars and MSL) can acquire data on much shorter timescales compared to the APXS and at standoff distances of ~ 1 m (Salle et al., 2005). A combined XRD/XRF (Blake et al., 2003; Marinangeli et al., 2005) instrument can provide mineralogical data in conjunction with the geochemistry of rocks. These instruments are extremely promising although they have not yet been deployed on Mars. Future opportunities for the XRS include the Chinese Chang'e II lunar rover (Talboys et al., 2005) and potentially for other terrestrial bodies such as Venus (Talboys et al., 2006). The studies described in this thesis can contribute to the development of the XRS to optimise the performance of the instrument for future planetary applications.

Bibliography

Allen, C. C., R. V. Morris, K. M. Jager, D. C. Golden, D. J. Lindstrom, M. M. Lindstrom, J. P. Lockwood, "Martian regolith simulant JSC MARS-1", *Lunar and Planetary Science XXXIX*, no. 1690, (1998).

Alvarez, R. P., P. J. Van Espen, A. A. Quintana, "Assessing scattering effects in annular radioisotope excited XRF", *X-Ray Spectrometry*, vol. 33, no. 1, (2004), pp. 74-82.

Baird, A. K., A. J. Castro, B. C. Clark, P. Toulmin, H. Rose, K. Keil, J. L. Gooding, "The Viking X-ray fluorescence experiment: Sampling strategies and laboratory simulations", *Journal of Geophysical Research*, vol. 82, (1977), pp. 4595-4624.

Bandfield, J. L., V. E. Hamilton, P. R. Christensen, "A global view of martian surface compositions from MGS-TES", *Science*, vol. 287, (2000), pp.1626-1630.

Berger, M. J., J. H. Hubbell, S. M. Seltzer, J. Chang, J. S. Coursey, R. Sukumar, D. S. Zucker, XCOM: Photon Cross Sections Database, National Institute of Standards and Technology Database 8 (XGAM), <http://physics.nist.gov/PhysRefData/Xcom/Text/XCOM.html> (5th January 2006).

Bertolini, G., A. Coche, "*Semiconductor Devices*", Elsevier-North Pub. Co., Amsterdam, 1968.

Blake, D. F., P. Sarrazin, S. J. Chipera, D. L. Bish, D. T. Vaniman, Y. Bar-Cohen, S. Sherrit, S. Collins, B. Boyer, C. Bryson, J. King, "Definitive mineralogical analysis of martian rocks and soils using the Chemin XRD/XRF instrument and the USDC sampler", *Sixth International Mars Conference*, no. 3022, (2003).

Bogard, D. D., D. H. Garrison, "Argon-39-argon-40 'ages' and trapped argon in Martian shergottites Chassigny and Allan Hills 84001", *Meteoritics and Planetary Science*, vol. 34, (1999), pp. 451-473.

Bradley, J. G., J. M. Conley, A. L. Albee, J. S. Iwanczyk, A. J. Dabrowski, W. K. Warburton, "Practical application of HgI₂ detectors to a space-flight scanning electron microscope", *Nuclear Instruments and Methods*, vol. A283, (1989), pp. 348-351.

Bridges, J. C., A. M. Seabrook, D. A. Rothery, J. R. Kim, C. T. Pillinger, M. R. Sims, M. P. Golombek, T. Duxbury, J. W. Head, A. F. C. Haldemann, K. L. Mitchell, J.-P. Muller, S. R. Lewis, C. Moncrieff, I. P. Wright, M. M. Grady, J. G. Morley, "Selection of the landing site in Isidis Planitia of Mars probe Beagle 2", *Journal of Geophysical Research*, vol. 108, issue E1, no. 5001, (2003).

Brückner, J., G. Dreibus, R. Rieder, H. Wänke, "Refined data of Alpha Proton X-ray Spectrometer analyses of soils and rocks at the Mars Pathfinder site: Implications for surface chemistry", *Journal of Geophysical Research*, vol. 108, issue. E12, no. 8094, (2003).

Butcher, G., "FM XRS Pre-Flight Science Test Results", Beagle 2 Project Report, BGL2-LUX-TN-0225, 16th January 2003.

Campbell, J. L., J. X. Wang, "Improved model for the intensity of low-energy tailing in Si(Li) X-ray Spectra", *X-ray Spectrometry*, vol. 20, (1991), pp. 191-197.

Campbell, J. L., J. A. Maxwell, T. Papp, G. White, "Si(Li) detector lineshapes: Contributions from atomic physics and detector properties", *X-ray Spectrometry*, vol. 26, (1997), pp. 223-231.

Carr, M. H., "*Water on Mars*", Oxford University Press, 1995.

Chu, S. Y. F., L. P Ekstrom, R. B. Firestone, "The Lund/LBNL Nuclear Data Search", Version 2.0, February 1999, <http://nucleardata.nuclear.lu.se/NuclearData/toi/>.

Clark, B. C., A. K. Baird, "Ultraminiature X-ray Fluorescence Spectrometer for in-situ geochemical analysis on Mars", *Earth and Planetary Science Letters*, vol. 19, (1973), pp. 359-368.

Clark, B. C., Baird, A. K., H. J. Rose, K. Keil, A. J. Castro, W. C. Kelliher, C. D. Rowe, P. H. Evans, "Inorganic analyses of Martian surface samples at the Viking lander sites", *Science*, vol. 194, (1976a), pp. 1283-1288.

Clark, B. C., P. Toulmin, A. K. Baird, K. Keil, H. J. Rose, "Argon content of Martian atmosphere at Viking-1 landing site – Analysis by X-ray fluorescence spectroscopy", *Science*, vol. 193,

(1976b), pp 804-805.

Clark, B. C., A. K. Baird, H. J. Rose, P. Toulmin, R. P. Christian, W. C. Kelliher, A. J. Castro, C. D. Rowe, K. Keil, G. R. Huss, "The Viking X-ray fluorescence experiment: analytical methods and early results", *Journal of Geophysical Research*, vol. 82, (1977), pp. 4577-4594.

Clark, B. C., A. K. Baird, R. J. Weldon, D. M. Tsusaki, L. Schnabel, M. P. Candelaria, "Chemical composition of Martian fines", *Journal of Geophysical Research*, vol. 87, (1982), pp. 10059-10067.

Committee on Planetary and Lunar Exploration (COMPLEX), "Assessment of Mars Science and Mission Priorities", Space Studies Board, Division on Engineering and Physical Sciences, National Research Council of the National Academies, National Academies Press, Washington, D. C., 2003.

Dalrymple, G. B., M. A. Lanphere, "Potassium-Argon Dating: Principles, Techniques and Applications to Geochronology", W. H. Freeman and Company, 1969.

de Vries, J. L., B. A. R. Vrebos, "Quantification of infinitely thick specimens by XRF analysis", Chapter 5 in Van Grieken, R. E. and Markowicz, A. A., "Handbook of X-ray Spectrometry", Marcel Dekker Inc., 2nd Ed. 2002.

Doran, P. T., S. M. Clifford, S. L. Forman, L. Nyquist, D. A. Papanastassiou, B. W. Stewart, N. C. Sturchio, T. D. Swindle, T. Cerling, J. Kargel, G. McDonald, K. Nishiizumi, R. Poreda, J. W. Rice, K. Tanaka, "Mars chronology: assessing techniques for quantifying surficial processes", *Earth Science Reviews*, vol. 67, (2004), pp. 313-337.

Ebel, M., M. Mantler, S. Saxinger, R. Svagera, B. Wernsperger, P. Wobrauschek and A. C. Huber, "On the energy dependence of the detector efficiency of a Si-PIN diode", *Advances in X-ray Analysis*, vol. 42, (1998), pp. 36-43.

Ellis, A. T., Chapter 3 in, Van Grieken, R. E. and A. A. Markowicz, "Handbook of X-ray Spectrometry", Marcel Dekker Inc., 2nd Ed., 2002.

Endt, P. M., "Energy levels of A = 21-44 nuclei (VII)", *Nuclear Physics*, vol. A521, (1990), pp. 1-830; *Errata and Addenda Nuclear Physics*, vol. A529, (1991), pp. 763-764; *Errata and Addenda Nuclear Physics*, vol. A564, (1993), pp. 609-614.

Eugster, O., "Comic-ray exposure ages of meteorites and lunar rocks and their significance", *Chemis der Erde Geochemistry*, (2003), vol. 63, pp. 3-30.

Fano, U., "Ionization yield of Radiations II: The fluctuations of the number of ions, *Physical Review*, vol. 72, (1947), pp. 26-29.

Faure, G., "*Principles of Isotope Geology*", John Wiley and Sons, 2nd Ed., 1977.

Fletcher-Holmes, D. W., "Avalanche photodiodes for the CATSAT gamma-ray burst mission", Ph. D. Thesis, University of Leicester, 2000.

Foley, C. N., T. E. Economou, R. N. Clayton, W. Dietrich, "Calibration of the Mars Pathfinder alpha proton X-ray Spectrometer", *Journal of Geophysical Research*, vol. 108, issue E12, no. 8095, (2003a).

Foley, C. N., T. Economou, R. N. Clayton, "Final Chemical Results from the Mars Pathfinder alpha proton X-ray Spectrometer", *Journal of Geophysical Research*, vol. 108, issue. E12, no. 8096, (2003b).

Fraser, G. W., A. F. Abbey, A. Holland, K. McCarthy, A. Owens, A. Wells, "The X-ray energy response of silicon: Part A. Theory", *Nuclear Instruments and Methods*, vol. A350, (1994), pp. 368-378.

Gellert, R., R. Rieder, R. C. Anderson, J. Brückner, B. C. Clark, G. Dreibus, T. Economou, G. Klingelhöfer, G. W. Lugmair, D. W. Ming, S. W. Squyres, C. d'Uston, H. Wänke, A. Yen, J. Zipfel, "Chemistry of rocks and soils in Gusev Crater from the Alpha Particle X-ray Spectrometer", *Science*, vol. 305, (2004), pp. 829-832.

Gellert, R., R. Rieder, J. Brückner, B. Clark, G. Dreibus, G. Klingelhofer; G. Lugmair, D. Ming, D. H. Wänke, A. Yen, J. Zipfel, S. Squyres, "The Alpha Particle X-Ray Spectrometer

(APXS): Results from Gusev Crater and calibration report”, *Journal of Geophysical Research*, vol. 111, issue. E2, no. 2555, (2006).

Gladney, E. S., I. Roelandts, “1987 compilation of elemental concentration data for USGS BHVO-1, MAG-1, QLO-1, RGM-1, SCo-1, SDC-1, SGR-1 and STM-1”, *Geostandards Newsletter*, vol. 12, (1988), pp. 253-362.

Gladney, E. S., E. A. Jones, E. J. Nickell, I. Roelandts, “1988 compilation of elemental concentration data for USGS Basalt BCR-1”, *Geostandards Newsletter*, vol. 14, (1990), pp. 209-359.

Gladney, E. S., I. Roelandts, “1988 compilation of elemental concentration data for USGS geochemical exploration reference materials GXR-1 to GXR-6”, *Geostandards Newsletter*, vol. 14, (1990), pp. 21-118.

Gladney, E. S., E. A. Jones, E. J. Nickell, I. Roelandts, “1988 compilation of elemental concentration data for USGS DTS-1, G-1, PCC-1, and W-1”, *Geostandards Newsletter*, vol. 15, (1991), pp.199-396.

Gladney, E. S., E. A. Jones, E. J. Nickell, I. Roelandts, “1988 compilation of elemental concentration data for USGS AGV-1, GSP-1 and G-2”, *Geostandards Newsletter*, vol. 16, (1992), pp. 111-300.

Golombek, M. P., R. A. Cook, T. Economou, W. M. Folkner, A. F. C. Haldemann, P. H. Kallemeyn, J. M. Knudsen, R. M. Manning, H. J. Moore, T. J. Parker, R. Rieder, J. T. Schofield, P. H. Smith, R. M. Vaughan, “Overview of the Mars Pathfinder mission and assessment of landing site predictions”, *Science*, vol. 278, (1997), pp. 1743-1748.

Gorevan, S. P., T. Myrick, K. Davis, J. J. Chau, P. Bartlett, S. Mukherjee, R. Anderson, S. W. Squyres, R. E. Arvidson, M. B. Madsen, P. Bertelsen, W. Goetz, C. S. Binou, L. Richter, “Rock abrasion tool: Mars exploration rover mission”, *Journal of Geophysical Research*, vol. 108, issue E12, no. 8068, (2003).

Govindaraju, K., “1994 compilation of working values and descriptions for 383 geostandards”,

Geostandards Newsletter, vol. 18, (1994), pp. 1-158.

Govindaraju, K., P. J. Potts, P. C. Webb, J. S. Watson, "1994 report on Whin Sill Dolerite from England and Pitscurrie Microgabbro PM-S from Scotland – Assessment by 104 international laboratories" *Geostandards Newsletters*, vol. 18, (1994), pp. 211-300.

Govindaraju, K., "Working Values with confidence limits for twenty-six CRPG, ANRT and IWG-GIT geostandards", *Geostandards Newsletter*, vol. 19, (1995), pp. 1-32.

Griffiths, A. D., A. J. Coates, J.-L. Josset, G. Paar, B. Hofmann, D. Pullan, P. Rüffer, M. R. Sims, C. T. Pillinger, "The Beagle 2 stereo camera system", *Planetary and Space Science*, vol. 53, (2005), pp. 1466-1482.

Hamilton, V. E., M. B. Wyatt, H. Y. McSween, P. R. Christensen, "Analysis of terrestrial and martian volcanic compositions using thermal emission spectroscopy: 2. Application to martian surface spectra from the Mars global surveyor thermal emission spectrometer", *Journal of Geophysical Research*, vol. 106, (2001), pp.14733-14746.

Harland, D. M., "*The Earth in Context: a Guide to the Solar System*", Springer-Verlag, 2001.

Harland, D. M., "*Water and the Search for Life on Mars*", Springer-Verlag, 2005.

Hartmann, W. K., G. Neukum, "Cratering chronology and the evolution of Mars", *Space Science Reviews*, vol. 96, (2001), pp. 165-194.

He, F., P. J. Van Espen, "General approach for quantitative energy-dispersive X-ray fluorescence analysis based on fundamental parameters", *Analytical Chemistry*, vol. 63, (1991), pp. 2237-2244.

Horwitz, W., L. R. Kamps, K. W. Boyer, "Quality assurance in the analysis of foods for trace constituents", *Journal of the Association of Official Analytical Chemists*, vol. 63, (1980), pp. 1344-1354.

Hubbell, J. H., W. J. Veigele, E. A. Briggs, R. T. Brown, D. T. Cromer, R. J. Howerton, "Atomic

form factors, incoherent scattering functions, and photon scattering cross sections”, *Journal of Physical and Chemical Reference Data*, vol. 4, (1975), pp. 471-538.

IAEA, IAEA Manual, “*QXAS Quantitative X-ray Analysis System*”, Vienna, 1996.

IAEA, Fundamental Parameter Calculator Software, Copyright 2003-2004, International Atomic Energy Agency, P.O. Box 100, Wagramer Strasse 5, A-1400 Vienna, Austria, <http://www.iaea.org/OurWork/ST/NA/NAAL/pci/ins/xrf/pciXRFdown.php> (28th September 2005).

International Organisation for Standardisation (Geneva), “*Terms and Definitions Used in Connection with Reference Materials*”, ISO Guide 30, International Organisation for Standardisation (Geneva), 2nd Ed., 1992.

IUPAC, “Nomenclature, symbols, units and their usage in spectrochemical analysis – II – data interpretation”, *Spectrochimica Acta*, vol. B33, (1978), pp. 242-245.

Iwanczyk, J. S., Y. J. Wang, J. G. Bradley, J. M. Conley, A. L. Albee, W. F. Schneppe, “Advances in the development of encapsulants for mercuric iodide detectors”, *IEEE Transactions on Nuclear Science*, vol. 37, no. 6, (1990), pp. 2214-2218.

Jenkins, R., R. W. Gould, D. Gedcke, “*Quantitative X-ray spectrometry*”, Marcel Dekker Inc., 2nd Ed., 1995.

Johnson, J. B., “Thermal agitation of electricity by conductors”, *Physical Review*, vol. 32, (1928), pp. 97-109.

Jordanov, V. T., J. A. Pantazis, A. C. Huber, “Compact circuit for pulse rise-time discrimination”, *Nuclear Instruments and Methods*, vol. A380, (1996), pp. 353-357.

Kaldarar, H., C. Strelj, “Comparison of response function fitting with QXAS-AXIL non linear least square fitting: Spectral evaluation of low Z elements”, *Advances in X-ray Analysis*, vol. 48, (2004).

Kalinka, G., T. Papp, G. Hegyesi, "Spectral artefacts with a Si-pin photodiode X-ray detector: II. The high energy case", Annual Report Institute of Nuclear Research of the Hungarian Academy of Science (ATOMKI), (2001), p. 63.

Kane, J. S., B. F. Arbogast, J. S. Leventhal, "Characterization of Devonian Ohio Shale SDO-1 as a USGS geochemical reference sample" *Geostandards Newsletter*, vol. 14, (1990), pp. 169-196.

Kargel, J. S., "*Mars: A Warmer, Wetter Planet – Climate Change on the Red Planet*", Springer-Verlag, 2004.

Karydas, A. G., Ch. Zarkadas, A. Kyriakis, J. Pantazis, A. Huber, R. Redus, C. Potiriadis, T. Paradellis, "Improvement of peak-to background ratio in PXE and XRF methods using thin Si-PIN detectors", *X-ray Spectrometry*, vol. 32, (2003), pp. 93-105.

Kelley, S., private communication, 2005.

Klingelhöfer, G., R.V. Morris, B. Bernhardt, D. Rodionov, P. A. de Souza Jr., S. W. Squyres, J. Foh, E. Kankeleit, U. Bonnes, R. Gellert, Ch. Schröder, S. Linkin, E. Evlanov, B. Zubkov, O. Prilutski, "Athena MIMOS II Mossbauer spectrometer investigation", *Journal of Geophysical Research*, vol. 108, issue E12, no. 8067, (2003).

Knoll, G. F., "*Radiation detection and Measurement*", John Wiley & Sons, 3rd Ed., 2000

Krause, M. O., "Atomic radiative and radiationless yields for the K and L shells", *Journal of Physical and Chemical Reference Data*, vol. 8, (1979), pp. 307-327.

Krause, M. O., J. H. Oliver, "Natural widths of atomic K and L levels, $K\alpha$ X-ray lines and several KLL Auger lines", *Journal of Physical and Chemical Reference Data*, vol. 8, (1979), pp. 329-338.

Kump, P., "Some considerations on the definition of the limit of detection in X-ray fluorescence spectrometry", *Spectrochimica Acta Part B*, vol. 52, (1997), pp. 405-408.

Kump, P., M. Nečemer and J. Drinovec, "The capabilities of an electrically cooled energy-

dispersive X-ray detector for quantitative X-ray fluorescence analysis”, *X-Ray Spectrom.*, vol. 33, (2004), pp. 107-111.

Lechner, P., A. Pahlke, H. Soltau, “Novel High-Resolution Silicon Drift Detectors”, *X-Ray Spectrometry*, vol. 33, (2004), pp. 256-261.

Lederer, C. M., J. M. Holland, I. Pearlman, “*Table of Isotopes*”, John Wiley, New York, 6th Ed., 1967.

Lepy, M. C., J. Plagnard, P. Stemmler, G. Ban, L. Beck, P. Dhez, “Si(Li) detector efficiency and peak shape calibration in the low-energy range using synchrotron radiation”, *X-ray Spectrometry*, vol. 26, (1997), pp. 195-202.

Lide, D. R., “*Handbook of Chemistry and Physics*”, CRC Press Inc., 73rd Ed., 1992.

Longhi, J., E. Knittle, J. R. Holloway, H. Wänke, “*The Bulk Composition, Mineralogy and Internal Structure of Mars*” in H.H. Kieffer, B. M. Jakosky, C. W. Snyder, M. S. Matthews (Eds.) “*Mars*”, The University of Arizona Press, 1992.

Marinangeli, L., A. Baliva, R. Delhez, A. Wielders, A. Holland, I. Hutchison, C. Ponzoni, A. Stevoli, “A European X-ray Diffractometer for the ExoMars Mission”, *Geophysical Research Abstracts*, vol. 7, no. 10791, (2005).

McKay, C. P., “Exobiology and future Mars missions: The search for Mars’ earliest biosphere”, *Advances in Space Research*, vol. 6, (1986), pp. 269-285.

McMaster, W. H., N. K. Delgrand, J. H. Mallet, J. H. Hubbell, “*Compilation of X-ray cross sections*”, UCRL Report 50174, Lawrence Livermore Lab, University of California, USA, 1968.

McSween Jr., H. Y., “The rocks of Mars, from far and near”, *Meteoritics and Planetary Science*, vol. 37, (2002), pp. 7-25.

McSween Jr., H. Y., “*Mars*”, Chapter 1.22 in Davis, A. M. (Ed.), “*Meteorites, Comets and Planets*”, Treatise on Geochemistry Vol. 1, Elsevier Press, 2005.

Meyer, C. et al. (Eds.), "Planetary Surfaces Instruments Workshop", LPI Technical Report, Houston, TX, Lunar and Planetary Institute, no. 95-05, 1996.

Moseley, H. G. J., "The high frequency spectra of the elements", *Philosophical Magazine*, vol. 26, (1913), pp. 1024-1034.

Moseley, H. G. J., "The high frequency spectra of the elements. Part II", *Philosophical Magazine*, vol. 27, (1914), pp. 703-713.

Mustard, J. F., S. Murchie, S. Erard, J. M. Sunshine, "In situ compositions of martian volcanics: implications for the mantle", *Journal of Geophysical Research*, vol. 102, (1997), pp. 25605-25615.

National Institute of Standards and Technology (NIST), Certificate of Analysis, Standard Reference Material 2709, San Joaquin Soil, 18th July 2003.

National Institute of Standards and Technology (NIST), Certificate of Analysis, Standard Reference Material 2710, Montana Soil, 18th July 2003.

National Institute of Standards and Technology (NIST), Certificate of Analysis, Standard Reference Material 2711, Montana Soil, 18th July 2003.

Neukum, G., B.A. Ivanov, W.K. Hartmann, "Cratering records in the inner Solar System in relation to the Lunar reference system", *Space Science Reviews*, vol. 96, (2001), pp. 55-86.

Neukum, G., R. Jaumann, H. Hoffmann, E. Hauber, J. W. Head, A. T. Basilevsky, B. A. Ivanov, S. C. Werner, S. van Gasselt, J. B. Murray, T. McCord and The HRSC Co-Investigator Team, "Recent and episodic volcanic and glacial activity on Mars revealed by the High Resolution Stereo Camera", *Nature*, vol. 432, (2004), pp. 971-979

Nicholson, P. W., "*Nuclear Electronics*", Wiley, London, 1974

Nielson, K., "Matrix corrections for energy dispersive X-ray fluorescence analysis of environmental samples with coherent/incoherent scattered X-rays", *X-Ray Spectrometry*, vol. 49, (1977), pp. 641-648.

Omand, M., J. L. Campbell, J. A. Maxwell, "Simulation of the relationship between element concentrations and X-ray yields in the Mars Exploration Rovers X-ray Spectrometer", *Nuclear Instruments and Methods*, vol. A229, (2005), pp. 123-136.

Owens, A., G. W. Fraser, K. J. McCarthy, "On the experimental determination of the Fano factor in Si at soft X-ray wavelengths", *Nuclear Instruments and Methods*, vol. A491, (2002), pp. 437-443.

Pantazis, J., private communication to G. Fraser, 2000.

Parus, J., W. Raab, D. L. Donohue, "Comparison of a compact energy-dispersive spectrometer with a wavelength-dispersive spectrometer for brass and stainless steel", *X-Ray Spectrometry*, vol. 30, (2001), pp. 296-300.

Patterson, J. H., A. L. Turkevich, E. Franzgrote, "Chemical analyses of surfaces using alpha particles", *Journal of Geophysical Research*, vol. 70, (1965), pp. 1311-1327.

Pearson, J. F., "Advances in soft X-ray performance of microchannel plate detectors", Ph.D. Thesis, University of Leicester, 1984.

Potts, P. J., "*A handbook of Silicate Rock Analysis*", Blackie & Son Limited, London, 1987.

Potts, P. J., P. C. Webb, O. Williams Thorpe, "Analysis of silicate rocks using field-portable X-ray fluorescence instrumentation incorporating a mercury(II) iodide detector: a preliminary assessment of analytical performance", *Analyst*, vol. 120, (1995), pp. 1273-1278.

Potts, P. J., O. Williams-Thorpe, P. C. Webb, "The bulk analysis of silicate rocks by portable x-ray fluorescence: Effect of sample mineralogy in relation to the size of the excited volume", *Geostandards Newsletter*, vol. 21, no. 1, (1997a), pp. 29-41.

Potts, P. J., P. C. Webb, O. Williams-Thorpe, "Investigation of a correction procedure for surface irregularity effects based on scatter peak intensities in the field analysis of geological and archaeological rock samples by portable X-ray fluorescence spectrometry", *Journal of Analytical Atomic Spectroscopy*, vol. 12, (1997b), pp. 769-776.

Potts, P. J., M. Thompson, J. S. Kane, P. C. Webb, J. Carignan, "GEOPT6 - an international proficiency test for analytical geochemistry laboratories - report on round 6 (OU-3: Nanhoron microgranite) and 6A (CAL-S: CRPG limestone)", *International Association of Geoanalysts*, (2000), unpublished report.

Potts, P. J., M. Thompson, S. Wilson, "G-Probe-1 – An international proficiency test for microprobe laboratories – Report on round 1 February 2002 (TB-1 basaltic glass)", *Geostandards Newsletter*, vol. 26, no. 2, (2002), pp. 197-235.

Potts, P. J., F. Bernardini, M. C. Jones, O. Williams-Thorpe, P. C. Webb, "Effects of weathering on *in situ* portable X-ray fluorescence analysis of geological outcrops: Dolerite and rhyolite outcrops from the Preseli Mountains, South Wales", *X-ray Spectrometry*, vol. 35, (2006), pp. 8-18.

Pullan, D., M. R. Sims, I. P. Wright, C. T. Pillinger, R. Traunter, "Beagle 2: the Exobiological Lander of Mars Express", ESA Special Publication SP-1240, 2004.

Ramsey, M. H., P. J. Potts, P. C. Webb, P. Watkins, J. S. Watson, B. J. Coles, "An objective assessment of analytical method precision: comparison of ICP-AES and XRF for the analysis of silicate rocks", *Chemical Geology*, vol. 124, (1995), pp. 1-19.

Redus, R. H., A. C. Huber, J. A. Pantazis, "Improved thermoelectrically cooled X/ γ -ray detectors and electronics", *Nuclear Instruments and Methods*, vol. A458, (2001), p214-219.

Richter, L., P. Coste, V.V. Gromov, H. Kochan, R. Nadalini, T.C. Ng, S. Pinna, H.-E. Richter, K.L. Yung, "Development and testing of subsurface sampling devices for the Beagle 2 lander", *Planetary and Space Science*, vol. 50, (2002), pp. 903-913.

Rieder, R., H. Wänke, T. Economou, A. Turkevich, "Determination of the chemical composition of Martian soils and rocks: The alpha proton X-ray spectrometer", *Journal of Geophysical Research*, vol. 102, issue E2, (1997a), pp. 4027-4044,

Rieder, R., T. Economou, H. Wänke, A. Turkevich, J. Crisp, J. Brückner, G. Dreibus, H. Y. McSween Jr., “The chemical composition of martian soil and rocks returned by the mobile Alpha Proton X-ray Spectrometer: Preliminary results from the X-ray mode”, *Science*, vol. 278, no. 5344, (1997b), pp. 1771-1774.

Rieder, R., R. Gellert, J. Brückner, G. Klingelhöfer, G. Dreibus, A. Yen, S. W. Squyres, “The new Athena alpha particle X-ray spectrometer for the Mars Exploration Rovers”, *Journal of Geophysical Research*, vol. 108, no. E12, (2003).

Rieder, R., R. Gellert, R. C. Anderson, J. Brückner, B. C. Clark, G. Dreibus, T. Economou, G. Klingelhöfer, G. W. Lugmair, D. W. Ming, S. W. Squyres, C. d'Uston, H. Wänke, A. Yen, J. Zipfel, “Chemistry of rocks and soils at Meridiani Planum from the Alpha Particle X-ray Spectrometer”, *Science*, vol. 306, no. 5702, (2004), pp. 1746-1749.

Rousseau, R.M., “Detection limit and estimate of uncertainty of analytical XRF results”, *The Rigaku Journal*, vol. 18, (2001), pp. 33-47.

Rutherford, E., J. Chadwick, C. D. Ellis, “*Radiations from radioactive substances*”, Cambridge University Press, New York, 1930.

Salle, B., P. Mauchien, J.-L. Lacour, S. Maurice, R. C. Wiens, “Laser-induced breakdown spectroscopy: a new method for stand-off quantitative analysis of samples”, *Lunar and Planetary Science XXXVI*, no. 1693, (2005).

Schmidt, R., “Mars Express – Esa’s first mission to planet Mars”, *Acta Astronautica*, vol. 52, (2003), pp. 197-202.

Schröder, C., G. Klingelhöfer, W. Tremel, “Weathering of Fe-bearing minerals under Martian conditions investigated by Mössbauer spectroscopy”, *Planetary and Space Science*, vol. 52, (2004), pp. 997-1010.

Scofield, J. A., “Exchange corrections of K X-ray emission rates”, *Physical Review*, vol. A10, (1974a), pp. 1041-1049.

Scofield, J. A., “Hartree-Fock values of L X-ray emission rates”, *Physical Review*, vol. A10,

(1974b), pp. 1507-1510.

Sherman, J., "The theoretical derivation of fluorescent X-ray intensities from mixtures", *Spectrochimica Acta*, vol. 7, (1955), pp. 283-306.

Sims, M. R., C. T. Pillinger, I. P. Wright, J. Dowson, S. Whitehead, A. Wells, J. E. Spragg, G. Fraser, L. Richter, H. Hamacher, A. Johnstone, N. P. Meredith, C. de la Nougerede, B. Hancock, R. Turner, S. Peskett, A. Brack, J. Hobbs, M. Newns, A. Senior, M. Humphries, H. U. Keller, N. Thomas, J. S. Lingard, J. C. Underwood, N. M. Sale, M. F. Neal, G. Klingelhofer, T. C. Ng, "Beagle 2: a proposed exobiology lander for ESA's 2003 Mars express mission", *IAU SYMPOSIA*, vol. 23, issue 11, (1999), pp. 1925-1928.

Sims, M. R. (Ed.), "*Beagle 2 Mission Report*", University of Leicester, 2004.

Soffen, G. A., A. T. Young, "The Viking Missions to Mars", *Icarus*, vol. 16, issue 1, (1972), pp. 1-16.

Squyres S. W., R. E. Arvidson, E. T. Baumgartner, J. F. Bell, P. R. Christensen, S. Gorevan, K. E. Herkenhoff, G. Klingelhöfer, M. B. Madsen, R. V. Morris, R. Rieder, R. A. Romero, "Athena Mars Rover science investigation", *Journal of Geophysical Research*, vol. 108, issue E12, no. 8062, (2003).

Stöffler, D., G. Ryder, "Stratigraphy and isotope ages of Lunar geologic units: Chronological standard for the inner Solar System", *Space Science Reviews*, vol. 96, (2001), pp. 9-54.

Surkov, Y., "*Exploration of Terrestrial Planets from Spacecraft*", Wiley-Praxis Series in Astronomy and Astrophysics, John Wiley and Sons Ltd, 1996.

Swindle, T. D., "Could in situ dating work on Mars?", *Lunar and Planetary Science XXXII*, no. 1492, (2001).

Swindle, T. D., R. Bode, W. V. Boynton, D. A. Kring, M. Williams, A. Chutjian, M. R. Darrach, D. A. Cremers, R. C. Wiens, S. L. Baldwin, "AGE (Argon Geochronology Experiment): An instrument for in situ geochronology on the surface of Mars, *LPSC XXXIV*, no. 1488, (2003).

Sykes, J., S. Whitehead, "XRS shock and vibration test plan and report", BGL-LUX-PL-124, Issue 01, September 2000.

Sykes, J., private communication, 2003a.

Sykes, J., "Beagle2 PAW FM Vibration Test Report", BGL-LUX-TR-222, Issue 01, March 2003b.

Sykes, J., S. Whitehead, "Beagle 2 FM PAW/BEE Thermal Cycling Test Report", BGL-LUX-TR-2026, Issue 01, March 2003.

Szaloki, I., S. Szegedi, K. Varga, M. Braun, J. Osan, R. Van Grieken, "Efficiency calibration of energy-dispersive detectors for application in quantitative X- and γ -ray spectroscopy", *X-Ray Spectrometry*, vol. 30, (2001), pp. 49-55.

Talboys, D. L., G. W. Fraser, M. R. Sims, D. Pullan, H.-F. Chen, J.-S. Wang, Z.-Y. Pu, W.-X. Jiao, "A Sino-European collaboration to develop a potential payload element for the Chinese Lunar exploration programme", *Geophysical Research Abstracts*, vol. 7, no. 01158, (2005).

Talboys, D. L., N. Nelms, R. Ambrosi, G. W. Fraser, A. Ball, M. Bentley "X-ray and Gamma-ray Spectroscopy for the elemental composition and density of the Venusian surface", *Proceedings of the Venus Entry Probe Workshop, January 19-20 2006, ESA/ESTEC, Noordwijk, the Netherlands*, in press.

Tanaka, K. L., D.H. Scott, R. Greeley, "Global Stratigraphy," pp. 354–382 in H.H. Kieffer, B.M. Jakosky, C.W. Snyder, M.S. Matthews (Eds.), "*Mars*", The University of Arizona Press, 1992.

Taylor, J. R., "*An introduction to error analysis: The study of uncertainties in physical measurements*", University Science Books, Oxford University Press, California, 1982.

Thomas, N., B.S. Luthi, S.F. Hviid, H.U. Keller, W.J. Markiewicz, T. Blumchen, A.T. Basilevsky, P.H. Smith, R. Tanner, C. Oquest, R. Reynolds, J.-L. Josset, S. Beauvivre, B. Hofmann, P. Ruffer, C.T. Pillinger, "The microscope for Beagle 2", *Planetary and Space Science*, vol. 52, (2004), pp. 853-866.

Thompson, M., P. J. Potts, P. C. Webb, “GeoPT1. International proficiency test for analytical geochemistry laboratories – Report on round 1”, *Geostandards newsletter*, vol. 20, (1996). pp. 277-287.

Thompson, M., P. J. Lowthian, “The Horwitz function revisited”, *Journal of AOAC International*, vol. 80, no. 3, (1997), pp. 676-679.

Thompson, M., P. J. Potts, P. C. Webb, J. S. Kane, “GeoPT – A proficiency test for geoanalysis”, *Analyst*, vol. 122, no. 11, (1997), pp. 1249-1254.

Thompson, M., P. J. Potts, J. S. Kane, P. C. Webb, J. S. Watson, “GeoPT2. International proficiency test for analytical geochemistry laboratories - Report on round 2”, *Geostandards Newsletter*, vol. 22, (1998), pp. 127-156.

Thompson, M., “A natural history of analytical methods”, *Analyst*, vol. 124, no. 7, (1999), pp. 991-991.

Thompson, M., P. J. Potts, J. S. Kane, P. C. Webb, J. S. Watson, “GeoPT4. An international proficiency test for analytical geochemistry laboratories - Report on round 4”, *Geostandards Newsletter*, vol. 24, (2000), pp. E1-E37.

Thompson, A. C., D. T. Attwood, E. M. Gullikson, M. R. Howells, J. B. Kortright, A. L. Robinson, J. H. Underwood, K. Kim, J. Kirz, I. Lindau, P. Pianetta, H. Winick, G. P. Williams, J. H. Scofield, “X-ray Data Booklet”, Center for X-ray Optics and Advanced Light Source, 2nd Ed., January 2001, Lawrence Berkeley National Laboratory, University of California, Berkeley, California 94720.

Thompson, M., “The amazing Horwitz function”, *AMC Technical Brief*, Royal Society of Chemistry, no. 17, (2004).

Toulmin, P. A. K. Baird, B. C. Clark, K. Keil, H. J. Rose, “Inorganic chemical investigation by X-ray fluorescence analysis: The Viking Mars Lander”, *Icarus*, vol. 20, (1973), pp. 153-178.

Towner, M. C., M.R. Patel, T.J. Ringrose, J.C. Zarnecki, D. Pullan, M.R. Sims, S. Haapanala, A.-

M. Harri, J. Polkko, C.F. Wilson, A.P. Zent, R.C. Quinn, F.J. Grunthaner, M.H. Hecht, J.R.C. Garry, "The Beagle 2 environmental sensors: science goals and instrument description", *Planetary and Space Science*, vol. 51, (2004), pp. 1141-1156.

Turkevich, A. L., E. F. Franzgrote, J. H. Paterson, "Chemical Composition of lunar surface in Mare Tranquillitatis", *Science*, vol. 165, (1969), pp. 277-279.

Turkevich, A., "Chemical analysis of surfaces by use of large-angle scattering of heavy charged particles", *Science*, vol. 134, pp. 672 -674, (1961).

Van Espen, P., K. Janssens, J. Nobels, "AXIL-PC software for the analysis of complex X-ray spectra", *Chemom. Intell. Lab. Sys.*, vol. 1, (1987), pp. 109-114.

Van Espen, P., K. Janssens, "Spectrum Evaluation", Chapter 4 in Van Greiken, R. E. and Markowicz, A. A., "Handbook of X-ray Spectrometry", Marcel Dekker Inc., 2nd Ed., 2002.

Van Greiken, R. E. and Markowicz, A. A., "Handbook of X-ray Spectrometry", Marcel Dekker Inc., 2nd Ed., 2002.

Van Gysel, M., P. Lemberge, P. Van Espen, "Description of Compton peaks in energy-dispersive X-ray fluorescence spectra", *X-ray Spectrometry*, vol. 32, (2003), pp. 139-147.

Van Thienen, P., N. J. Vlaar, A. P. van den Berg, "Plate tectonics on the terrestrial planets", *Physics of the Earth and Planetary Interiors* vol. 142, (2004), pp.61-74.

Vasavada, A. R., "NASA's 2009 Mars Science Laboratory: an update", *Lunar and Planetary Science XXXVII*, no. 1940, (2006)

Verchovsky A., private communication, 2005.

VIM:1995, "Vocabulary of metrology. Part 1. Basic and general terms (international)". International Organisation for Standardisation (Geneva), British Standards Institution (London), PD 6461: Part 1, 1995.

Wänke, H., J. Brückner, G. Dreibus, R. Rieder, I. Ryabchikov, "Chemical composition of rocks and soils at the Pathfinder site", *Space Science Reviews*, vol. 96, (2001), pp. 317-330.

Wegrzynek, D., A. Markowicz, E. Chinea-Cano, "Application of the backscatter fundamental parameter method for *in situ* element determination using a portable energy-dispersive X-ray fluorescence spectrometer", *X-Ray Spectrometry*, vol. 32, (2003a), pp. 119-128.

Wegrzynek, D., A. Markowicz, E. Chinea-Cano, P. J. Potts, "Application of the backscatter fundamental parameter method with simultaneous excitation by ^{55}Fe and ^{109}Cd radioisotope sources", *Advances in X-ray Analysis*, vol. 46, (2003b), pp. 388-393.

Wright, I. P., M. R. Sims, C. T. Pillinger, "Scientific objectives of the Beagle 2 lander", *Acta Astronautica*, vol. 52, (2003), pp. 219-225.